

MICROFLUIDICS FOR TRANSLATING MULTIFUNCTIONAL NANOMATERIALS

A Dissertation
Presented to
The Academic Faculty

by

Yoshitaka J. Sei

In Partial Fulfillment
of the Requirements for the Degree
Doctor of Philosophy in the
George W. Woodruff School of Mechanical Engineering

Georgia Institute of Technology
December 2018

COPYRIGHT © 2018 BY YOSHITAKA J. SEI

MICROFLUIDICS FOR TRANSLATING MULTIFUNCTIONAL NANOMATERIALS

Approved by:

Dr. YongTae Kim, Advisor
George W. Woodruff School of Mechanical
Engineering
Georgia Institute of Technology

Dr. Andrés García
George W. Woodruff School of
Mechanical Engineering
Georgia Institute of Technology

Dr. Julie Champion
School of Chemical & Biomolecular
Engineering
Georgia Institute of Technology

Dr. Hanjoong Jo
Wallace H. Coulter Department of
Biomedical Engineering
Georgia Institute of Technology

Dr. J. Brandon Dixon
George W. Woodruff School of Mechanical
Engineering
Georgia Institute of Technology

Date Approved: August 1, 2018

ACKNOWLEDGEMENTS

Thank you to my parents, Shizuko and Yoshitatsu Sei. You are both my inspiration, and your unwavering faith in me has always helped me to look forward.

Thank you to my significant other, Alexis Lopez. You have always supported me, and I feel incredibly lucky to go through this journey with you.

Thank you to my advisor, Tony Kim. I appreciate the time and effort you took to provide many kinds of opportunities. I gained tremendous insight from my experiences with those opportunities, and I learned so much from my time at the Kim Lab.

Thank you to my Thesis Committee, Julie Champion, Brandon Dixon, Andrés García, and Hanjoong Jo. Your support and insights helped me to develop my perspective, and I appreciate the time you all took to guide me to the finish line.

Thank you to the past and present members of the Kim Lab. Learning with you all has been a privilege. I could not have asked for better lab mates and friends.

Thank you to Janet Levy, Krieks McDermott, Catherine McLellan, and Luke Whitesell. I am very fortunate to grow up with your support. Thank you for looking out for me.

Thank you to all my friends and family. I could not have done this without you.

The work presented in this thesis was supported by the startup resources of Georgia Institute of Technology, the American Heart Association Scientist Development Grant 15SDG25080314, the National Institutes of Health Director's New Innovator Award 1DP2HL142050, the National Science Foundation under CAREER CMMI 1653006, the Center for Pediatric Nanomedicine (CPN) of Children's Healthcare of Atlanta Seed Grant, the Basic Science Research Program through the National Research Foundation of Korea funded by the Ministry of Science, ICT & Future Planning NRF-2015R1A2A1A09005662, 2016R1A4A1010796, the National Institutes of Health/National Institute of General Medical Sciences-sponsored Cell and Tissue Engineering (CTEng) Biotechnology Training Program (T32GM008433), and the National Science Foundation Graduate Research Fellowship (DGE-1148903). This work was in part performed at the core facilities at the Parker H. Petit Institute for Bioengineering and Bioscience at the Georgia Institute of Technology and the Institute for Electronics and Nanotechnology at the Georgia Institute of Technology, a member of the National Nanotechnology Coordinated Infrastructure, which is supported by the National Science Foundation (Grant ECCS-1542174).

TABLE OF CONTENTS

ACKNOWLEDGEMENTS	III
LIST OF TABLES	VII
LIST OF FIGURES	VIII
SUMMARY	XI
CHAPTER 1. INTRODUCTION	1
1.1 Background	1
1.2 Research Objectives	13
CHAPTER 2. DETECTING THE FUNCTIONAL DIFFERENCES BETWEEN HIGH-DENSITY LIPOPROTEIN MIMETICS	14
2.1 Abstract	14
2.2 Introduction	15
2.3 Results and Discussion	18
2.4 Conclusions	30
2.5 Methods	31
2.6 Supplementary Information	39
CHAPTER 3. A MICROPHYSIOLOGICAL SYSTEM FOR DETECTING AND MONITORING THE INFLAMED ENDOTHELIUM	49
3.1 Abstract	49
3.2 Introduction	49
3.3 Results and Discussion	53
3.4 Conclusion	58
3.5 Methods	60
3.6 Supplementary Information	63
CHAPTER 4. PROBING THE IMPACT OF OSCILLATORY SHEAR STRESS ON HDL-MIMETIC NANOPARTICLE INTERACTIONS WITH THE ENDOTHELIUM	67
4.1 Abstract	67
4.2 Introduction	67
4.3 Results and Discussion	71
4.4 Conclusions	76
4.5 Methods	77
4.6 Supplementary Information	81
CHAPTER 5. CONCLUSIONS	84
5.1 Concluding Remarks	84
5.2 Current Challenges and Future Work	85

APPENDIX A. MICROFLUIDIC CELL CULTURE AND ELECTRODE FABRICATION	89
A.1. Overview	89
A.2. Electrode Fabrication	89
A.3. μ TM Assembly	93
A.4. Cell Culture	100
APPENDIX B. NANOPARTICLE SYNTHESIS WITH MICROFLUIDICS	105
B.1 Overview	105
B.2 Synthesis Protocol	105
APPENDIX C. RIGHTS AND PERMISSIONS	113
REFERENCES	114

LIST OF TABLES

TABLE S2.1. MOLECULAR DYNAMICS SIMULATIONS FOR EHNP-R4F.	48
---	----

LIST OF FIGURES

FIGURE 1.1. PREVALENCE OF LOCALIZED ATHEROSCLEROSIS IN VASCULATURE.....	1
FIGURE 1.2. PARTIAL LIGATION MOUSE MODEL FOR DISTURBED FLOW-INDUCED ATHEROSCLEROSIS.	2
FIGURE 1.3. HDL BASIC STRUCTURES AND COMPONENTS.....	4
FIGURE 1.4. THE SCALE OF TRANSLATIONAL TOOLS AND TECHNOLOGIES.	7
FIGURE 1.5 MICROFLUIDIC METHODS FOR NANOPARTICLE SYNTHESIS.	9
FIGURE 1.6. ENGINEERING LIVING SYSTEMS ON CHIPS.....	11
FIGURE 2.1. COMPARISON OF ENGINEERED HDL-MIMETIC NANOPARTICLES MADE FROM APOA1 OR R4F.	20
FIGURE 2.2. COMPARISON OF EHNP BIOACTIVITY.	22
FIGURE 2.3. ENDOTHELIAL RESPONSE TO EHNPs IN MICROENGINEERED VASCULAR SYSTEM.	24
FIGURE 2.4. INCORPORATING DOX INTO EHNPs FOR IN VITRO DELIVERY.	26
FIGURE 2.5. EHNP-FACILITATED DOX DELIVERY TO XENOGRAFT TUMOR IN A MURINE MODEL.	29
FIGURE S2.1. SCHIFFER-EDMUNSON DIAGRAM FOR R4F AND THE 10 ALPHA HELICES OF APOA1.....	40
FIGURE S2.2. ENGINEERING THE MICROVORTEX PROPAGATION MIXER (μ VPM).	42
FIGURE S2.3. SIZE DISTRIBUTIONS OF EHNP-A1	42
FIGURE S2.4. SIZE DISTRIBUTIONS OF EHNP-R4F.....	43
FIGURE S2.5. MICROENGINEERED VASCULAR SYSTEM COMPONENTS.	44

FIGURE S2.6. MICROENGINEERED VASCULAR SYSTEM TIMELINE.	45
FIGURE S2.7. DOX LOADING MEASUREMENTS.	46
FIGURE S2.8. PREPARATION FOR IN VIVO EXPERIMENT.	46
FIGURE S2.9. IN VIVO BIODISTRIBUTION MEASUREMENTS AND SETUP.	47
FIGURE S2.10. IVIS ANALYSIS FOR NUDE BALB/C MICE BEARING HL-60 TUMORS.....	48
FIGURE 3.1. MONITORING OF THE ENDOTHELIUM FOR FLOW-BASED STUDIES.	53
FIGURE 3.2. MICROFLUIDIC TRANSCELLULAR MONITOR DESIGN.	56
FIGURE 3.3. COMPARING LSS CASES FOR +1 AND +10 DYNE/CM ²	57
FIGURE 3.4. MONITORING OF ENDOTHELIAL FREQUENCY RESPONSE.....	58
FIGURE S3.1. MICROFLUIDIC TRANSCELLULAR MONITOR SETUP.	64
FIGURE S3.2. THE EFFECT OF THE MICROCHANNEL WALL.	65
FIGURE S3.3. OSS CULTURE TIMELINE FOR HAECs.	65
FIGURE S3.4. OSS FREQUENCY RESPONSE IN IMAECs.	66
FIGURE 4.1. DETECTING FLOW-DEPENDENT INTERACTIONS OF HDL WITH THE ENDOTHELIUM.	70
FIGURE 4.2. EHNP CONCENTRATION DEPENDENT ANALYSIS WITH LSS.....	72
FIGURE 4.3. EHNP CONCENTRATION DEPENDENT ANALYSIS WITH OSS.....	73
FIGURE 4.4. ENDOTHELIAL RESPONSE TO EHNPs WHEN SR-B1 IS BLOCKED.	76
FIGURE S4.1. HAEC CULTURE USING COLLAGEN 1.	81

FIGURE S4.2. ORIENTATION OF HAECs UNDER LSS OR OSS.	83
FIGURE A.1. CUTTING DIAGRAM FOR GLASS SLIDE.....	91
FIGURE A.2. LOCATION OF DRILLED HOLES FOR WIRES OF μ TM.....	98
FIGURE A.3. LOCATION OF SEALANT FOR μ TM.	99
FIGURE A.4. FINAL DEVICE READY FOR CELL CULTURE.....	100
FIGURE A.5. LOCATION OF HOLES IN LID FOR TUBING.....	102
FIGURE B.1. MATERIALS USED IN THE SYNTHESIS OF EHNPs.....	106
FIGURE B.2. MEASUREMENT OF TUBING.	107
FIGURE B.3. PE TUBING INSERTED INTO CP TUBING.....	107
FIGURE B.4. ASSEMBLED TUBING WITH NEEDLES AND ADAPTERS.	108
FIGURE B.5. ASSEMBLED μ VPM WITH TUBING.....	108
FIGURE B.6. μ VPM READY FOR SYNTHESIS.....	110
FIGURE B.7. COLLECTION OF NANOPARTICLES FROM EHNPs.....	111

SUMMARY

Conflicting results between benchtop experiments, animal models, and clinical trials have posed a significant challenge in translational medical research, motivating the development of technologies with which to assess and screen experimental therapeutics. Among these new technologies are microfluidic platforms that allow for the synthesis of nanoparticles and the tuning of microenvironments to replicate the ideal physiological conditions to study living responses *in vitro*. The advantages of using microfluidic technologies in order to accomplish these feats are attributed to volumetrically minimal usage of expensive reagents while also having the capacity to be run continuously for high-throughput and large-scale applications. Some of the challenges still associated to the general adoption of microfluidic technologies are those typically found in the early stages of new technological advancements: (1) a lack of standardization in work flow and platform design, and (2) a limited accessibility to specialized equipment. This thesis focuses on contributing to the standardization of the microfluidic workflow through exploring both platform designs for the synthesis and screening of nanoparticles, and exploring key translational questions with experiments that are uniquely enabled with microfluidics. The microfluidic platforms that are presented in this work are a mixer for nanoparticle synthesis and a monitor for the permeability of a cellular monolayer. These platforms were implemented in experiments studying the functionality of high-density lipoprotein mimetic nanoparticles and their interactions with endothelial cells within the context of cardiovascular disease. We report how the functionality of the high-density lipoprotein mimetic nanoparticles is affected by its protein composition, and how its interactions with the endothelial monolayer are modulated depending on the oscillatory flow stimulated inflammatory condition of the endothelial cells.

CHAPTER 1. INTRODUCTION

1.1 BACKGROUND

Cardiovascular disease (CVD) impacts one of the largest groups of individuals throughout the world [1]. One of the most common manifestations of CVD is through the formation of atherosclerotic plaques that lead to vascular occlusion and stiffening [2]. Initiation of atherosclerosis is preceded by chronic inflammation of the endothelium that largely occurs in areas with disturbed flow and high cholesterol levels in the blood [3, 4]. These areas with disturbed, or oscillatory, flow are largely localized to specific regions of vasculature: (1) carotid arteries, (2) coronary arteries, (3) abdominal aorta, and (4) ilio-femoral arteries (Fig. 1.1) [5]. Of these regions, the carotid arteries and ilio-femoral arteries have the highest prevalence of atherosclerotic plaques due to their unique geometries that enable the generation of disturbed flow profiles.

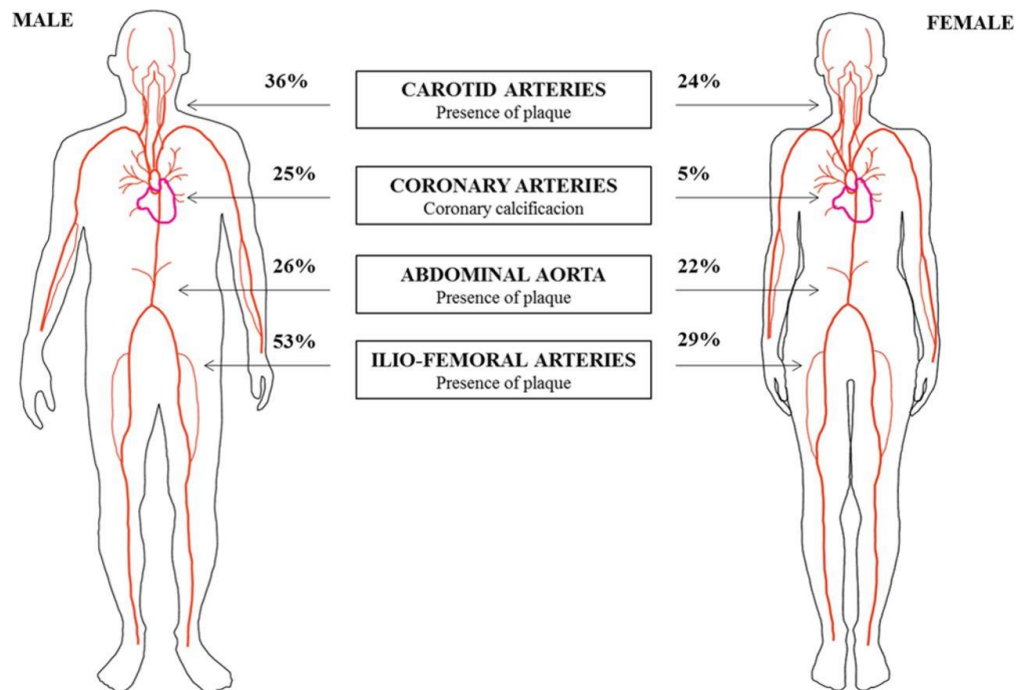


Figure 1.1. Prevalence of localized atherosclerosis in vasculature.

Atherosclerosis localization is most dominant in the regions with the most disturbed flow profiles: the carotid arteries and the ilio-femoral arteries. This figure was reproduced with permission [5].

The effects of localized disturbed flow have been studied in murine partial ligation models, which have become a gold-standard in studying atherosclerotic plaque initiation and progression [6, 7]. The model involves ligating the downstream portions of the left carotid artery (LCA) (Fig. 1.2A) to allow for the growth of an atherosclerotic plaque in an apolipoprotein E knockout mouse (Fig. 1.2B). The partial ligation of the LCA generates a disturbed flow profile that initiates the growth of the atherosclerotic plaque, which can be analyzed with histology and ultrasound equipment to compare the bidirectional flow velocities of the LCA to the unidirectional flow velocities of the right carotid artery (RCA) (Fig. 1.2C-F). The development of this mouse model allowed for the screening of therapeutic and diagnostic, or theranostic, materials, such as nanoparticles, statins, and nucleic acids [8-10]. However, how translatable an animal response to a therapy is when compared to a human response is a question that is still brought up due to the discrepancies in the results between animal studies and clinical trials [11].

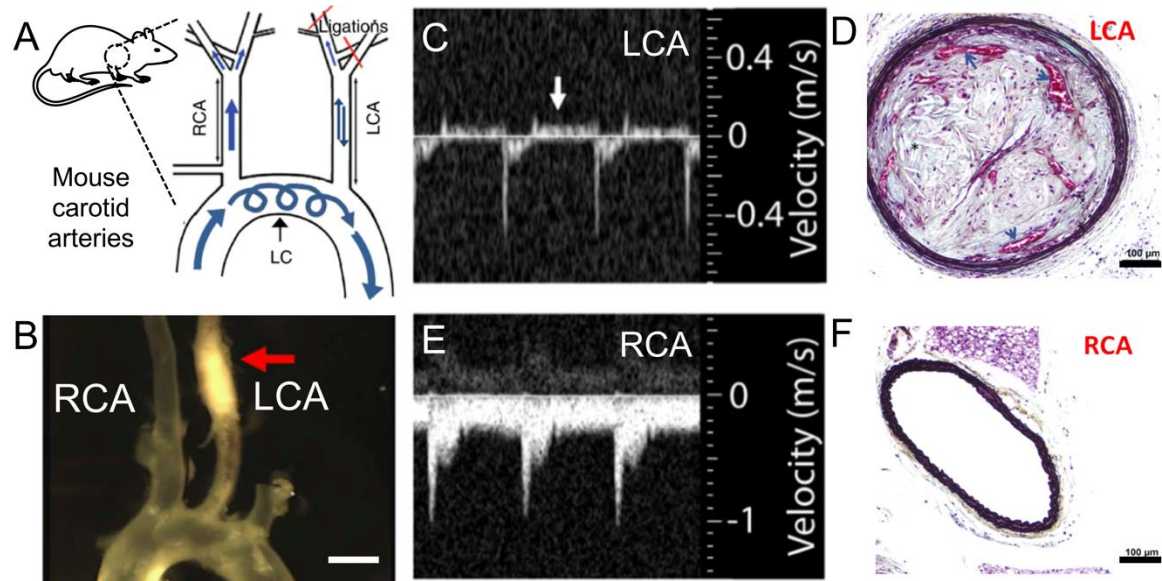


Figure 1.2. Partial ligation mouse model for disturbed flow-induced atherosclerosis. (A) The left carotid artery (LCA) of a mouse is ligated to allow for (B) the growth of an atherosclerotic plaque (red arrow). Scale bar is 1 mm. (C, D) Ultrasound and pentachrome staining can be used on the LCA and (E, F) right carotid artery (RCA) to compare the effects of disturbed flow on atherosclerotic plaque growth. Scale bar is 100 μm. This figure was adapted with permission [6, 8].

Current therapies for CVD patients primarily include dieting, exercise, and the use of statins, which are orally administered drugs that competitively inhibit cholesterol synthesis in the liver [12, 13]. However, patients who undergo these therapies still risk the occurrence of hepatic and/or cardiac related issues, forcing the need to develop additional therapies against inflammatory mechanisms that trigger atheroprotection [14, 15]. Of the potential therapies currently being studied, high-density lipoproteins (HDLs) have been studied for their key contributions to cardiovascular health, which include the regulation of lipid homeostasis in the body and their anti-inflammatory effects on the vascular endothelium [16, 17]. HDL is one of 5 lipoproteins with a size range of 7-17 nm across 5 subclasses: (1) very large, (2) large, (3) medium, (4) small, and (5) very small [18-20]. As a highly heterogeneous nanoparticle, HDL not only spans a range of sizes and densities throughout its subclasses, but it also has a diverse proteome and lipidome [19]. The primary structural and functional component of HDL is apolipoprotein-A1 (apoA1), which is the most abundant protein in the HDL proteome [21-23]. Making up over 70% of the HDL proteome, apoA1 stabilizes HDL as it matures and transitions from a discoidal structure to a spherical structure upon encapsulation of hydrophobic materials [19]. When HDL is in its discoidal configuration, a dimerized apoA1 “double-belt” stabilizes the particle; when in its spherical configuration, HDL is stabilized with 3 apoA1 proteins in a “trefoil” configuration (Fig. 1.3). This maturation cycle starts in the liver and gut with the association of lipid-free apoA1 with phospholipids to form the discoidal nanoparticles, often called nascent HDLs [23, 24]. As the nascent HDL internalizes cholesteryls and lipids from tissue during circulation, the discoidal structure matures into a spherical particle, a characteristic structural change indicating that the core of the particle has been filled with hydrophobic materials. The idea of using HDL to combat the effects of CVD was first introduced in the Framingham Studies that discovered an inverse correlation between the

serum HDL-levels and the incidence of CVD, which paved the way for the “HDL Hypothesis” [25-27].

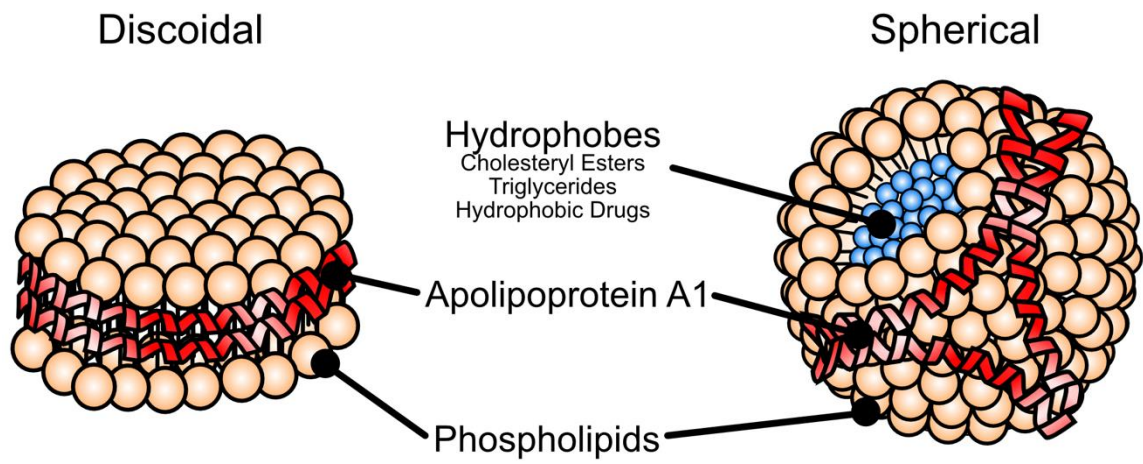


Figure 1.3. HDL basic structures and components.

Through a process called HDL maturation, HDL transitions from its discoidal “double-belt” configuration to its spherical “trefoil” configuration through the encapsulation of hydrophobic materials. The average diameter of the HDL nanoparticle is 10 nm.

The “HDL Hypothesis” poses the idea of raising serum HDL levels to decrease the incidence of CVD-related events [27]. In the context of nanomedicine, HDL has emerged as a promising option for an endogenous therapeutic delivery vehicle that is stable in circulation while intrinsically offering anti-inflammatory and atheroprotective effects [28-31]. Such effects include promoting of cholesterol efflux known as reverse cholesterol transport (RCT), inhibiting of endothelial adhesion molecules such as intercellular adhesion molecule-1 (ICAM-1) and vascular adhesion molecule-1 (VCAM-1), and functioning as an antioxidant that reduces the atherogenicity of lipoproteins like low-density lipoproteins (LDL) [32]. It should be noted that the diversity of the HDL proteome and lipidome, with over 200 detected types of associated proteins and lipids, has a distinct impact on the functionality of HDL [33, 34]. Several HDL-associated components and their functions include: (1) cholesterylester transfer protein (CETP) is needed for the exchange of triglycerides and cholesteryls between LDLs and HDLs; (2) paraoxonase-1 (PON1) provides HDL the enzymatic activity to combat the oxidative modification of HDL; and (3)

apolipoprotein-M (apoM) and sphingosine-1-phosphate (S1P) together enable HDL's interaction with S1P-1 and S1P-3 receptors to improve the barrier integrity of endothelial cells [33, 35, 36]. With varied levels of functionality that depend on composition, HDLs are likely to have heterogeneous characteristics that vary between patients [37]. Issues in transitioning HDL therapies from benchtop results to clinical practice continue to persist; simply raising the HDL serum levels have not conclusively resulted in reducing patient CVD outcomes [33, 38-40]. These therapies that focused on raising apoA1 concentrations in serum through infusion or oral administration, such as the recombinant apoA1 based CER-001 or CETP-inhibiting based Evacetrapib, failed to show regression of atherosclerotic plaques in clinical studies [40-42]. It is unclear whether or not the negative outcomes from HDL-therapy trials are due to the diversity of the HDL functionality between patients, which is a motivation to better understand the contributions of HDL's functional components. In order to achieve this level of understanding, it becomes necessary to engineer HDLs with a controlled composition and measure their interactions with living systems for translational research.

The transition of products from benchtop results to their practical usage in society, otherwise known as translational research, has come with many challenges since its implementation. Among these challenges include the development of medicines for use in clinical practice, which typically requires a massive investment of limited resources for a relatively low yield in practical results [11, 40, 43]. HDL therapies belong to a class of materials known as nanoparticles, therapeutic materials on the scale of 1-100 nm that can be engineered for specific applications with the capacity for multiple therapeutic and imaging agents [44-47]. Reported applications of HDL-nanoparticles include its use as an imaging agent through the incorporation of a gold crystal into the lipid core of an apoA1-stabilized nanoparticle [48, 49], its applications in gene-therapies through the delivery of small interfering ribonucleic acids (siRNA) [50], and through the use of apoA1-mimetic

peptides in an attempt to mimic or improve the anti-inflammatory properties of HDL [38]. These mimetic peptides, while having no sequence homology with apoA1, are capable of forming a class A amphipathic helix similar to those of the lipid binding domain for apoA1. The first mimetic peptides for apoA1 were based on an 18 amino acid sequence with varying physical and chemical properties; the most commonly known early peptides are 18A, 2F, 3F, and 4F [38]. Early tests of these peptides showed that it was difficult to detect peptide biofunctionality through the evaluation of just the physical and chemical properties; the 4F peptide garnered attention for its potential anti-inflammatory applications after demonstrations of its ability to induce reverse cholesterol transport from macrophages [51]. The positive outlook of the 4F peptide inspired the examination of its reverse sequence analog, r4F. The r4F peptide was also found to be able to replicate natural HDL functionality through cholesterol efflux assays, and was even used for diagnostic and therapeutic application studies in cancer and Alzheimer's disease [52, 53]. Although the r4F peptide's structure and functionality closely resembled that of natural HDL, a direct one-to-one comparison between r4F and apoA1 functionality had not been made. Aside from endogenous and synthetic lipoproteins, common forms of nanoparticles include liposomes, polymeric-nanoparticles, lipid-polymer nanoparticles, and gold nanoparticles [28, 54-56]. Combinations of these common nanoparticle types allows for the tuning of nanoparticle properties for specific diagnostic or therapeutic applications that require overcoming biological barriers through the fulfillment of certain criteria that include: circulation time, payload capacity, and tissue targeting [57]. Alongside the use of multiscale animal models, the advancements of translational microtechnology has allowed for the development of nanoparticle screening and manufacturing tools using microfluidic technology (Fig. 1.4).

Microfluidic technology encompasses systems that manipulate fluids in microscale channels, and this technology has become a foundation in *in vitro* examinations and

controlling microscale reactions [11, 58]. This is possible with the control over the fluidic environment that microfluidic-based systems offer [59]. Nanoparticle translation has also benefited from microfluidics through high-throughput and continuous production methods while maintaining nanoparticle quality as defined by a polydispersity index that describes the homogeneity of nanoparticle sizes [11, 60].

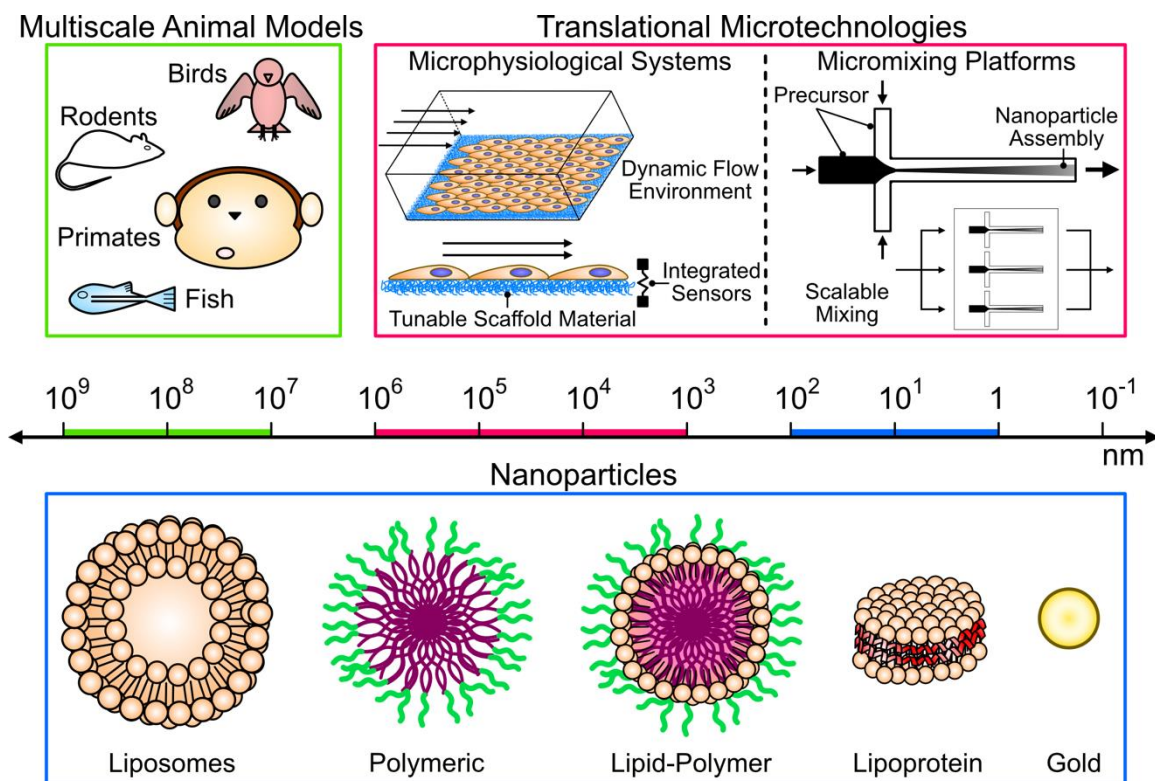


Figure 1.4. The scale of translational tools and technologies.

Translational tools that primarily consisted of animal models and static in vitro assays now include microtechnologies that can both screen nanoparticles on a microphysiological level, and that can upscale the manufacturing of nanoparticles with micromixing platforms on a parallelizable level.

Microfluidic mixing technologies drive the high-throughput synthesis strategies for nanoparticle translation. Microfluidic mixing was first identified as a crucial property to early lab-on-a-chip (LOC) or micro total analysis systems (μ TAS) due to the necessities of intimately mixing reagents in miniaturized reactors for biological, chemical, and medical applications [61]. Various mixing strategies, generally divided into passive or active forms of mixing, have been studied due to the challenges of mixing in a microenvironment where

viscous forces are dominant [62]. The mixing strategies employed in microfluidic platforms applied to the enhancement of nanoparticle self-assembly begin to address the challenges of nanoparticle batch-to-batch variation, shifting the nanoparticle synthesis paradigm from a bulk benchtop scheme to a more continuous and reliable manufacturing scheme [60]. Compared to the heterogeneous mixing environment of conventional bulk nanoparticle synthesis approaches, microfluidic approaches to nanoparticle synthesis use the small-scale fluidic interactions to control the fluidic mixing patterns, which results in a greater monodispersity of nanoparticles and ultimately reduces the batch-to-batch variation in the nanoparticle product. Advantages of microfluidic platforms in reducing nanoparticle polydispersity during self-assembly have been demonstrated across multiple mixing strategies including diffusion and microvortex formation (Fig. 1.5A and B) [54, 59, 60, 63]. The use of microvortices for the self-assembly of nanoparticles allows for higher

nanoparticle production rates compared to diffusion-based mixing approaches, which also promotes the formation of smaller nanoparticles [54, 63].

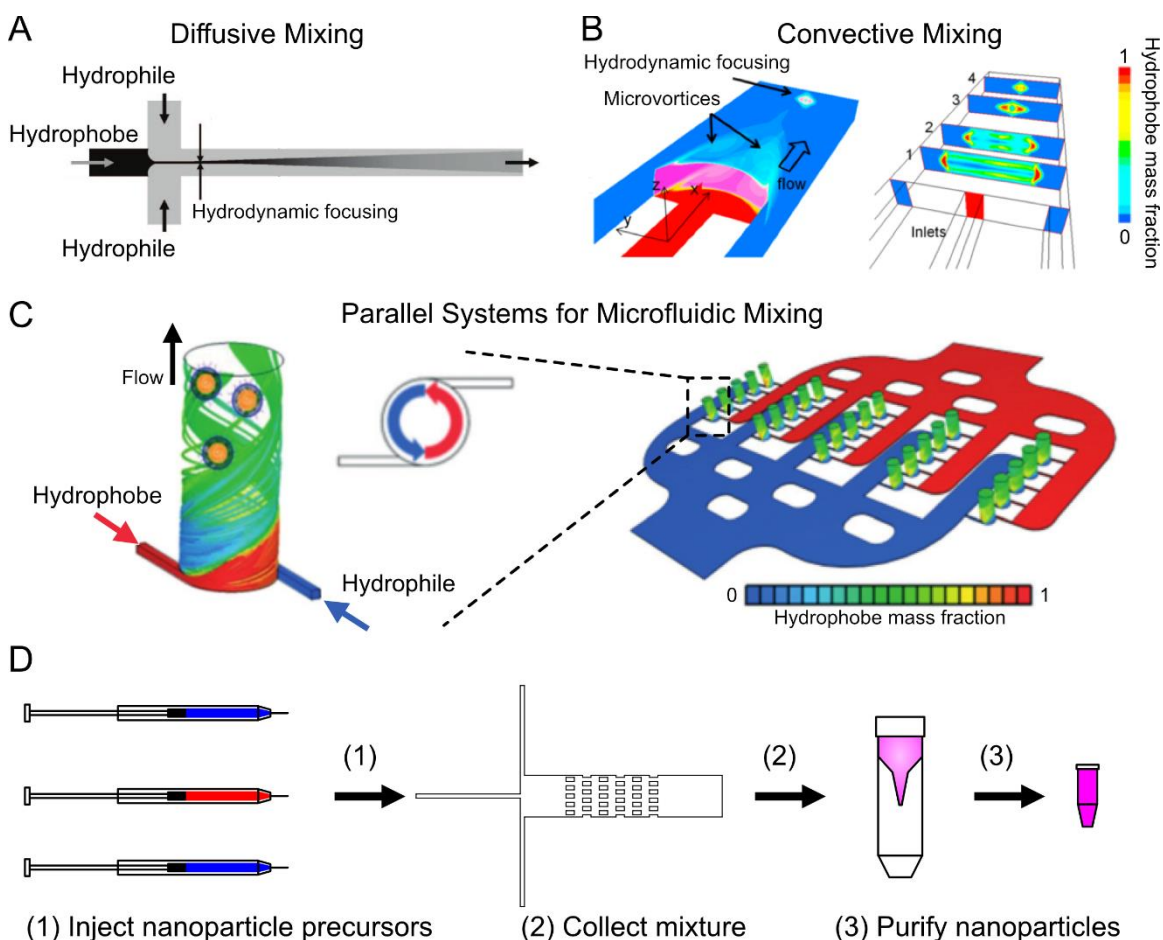


Figure 1.5 Microfluidic methods for nanoparticle synthesis.

(A) A diffusion-based synthesis typically occurs at low Re Numbers (< 1) and utilizes hydrodynamic focusing of the nanoparticle precursors to control their diffusion interface. (B) Convection-based synthesis occurs at high Re Numbers (> 50) to generate microvortices that can force the interactions of nanoparticle precursors while increasing the synthesis rate of the particle. (C) Parallelized systems may be implemented to scale-up a single microfluidic platform for industrially-relevant manufacturing. (D) The general synthesis scheme when implementing microfluidic methods for nanoparticle synthesis. This figure was adapted from [60, 63, 64].

The microfluidic nanoparticle synthesis strategy may also be scaled up through parallelized systems that increase the manufacturing rate of the nanoparticles while retaining nanoparticle quality (Fig. 1.5C) [64]. It should also be noted that the synthesis scheme between microfluidic methods of nanoparticle synthesis remains the same with 3 key steps: (1) injection of nanoparticle precursors into the microfluidic mixing system, (2)

collection of the nanoparticle mixture from the microfluidic system, and (3) purification of the nanoparticles from the precursor mixture (Fig. 1.5D). With regards to HDL, its microfluidic synthesis with the microvortex approach has not only allowed for HDL's efficient modification with diagnostic and therapeutic agents, but also in the retention of HDL's natural bioactive properties such as cholesterol efflux or the stimulation of endothelial nitric oxide [54, 65, 66]. In addition to the synthesis and manufacturing of nanoparticles, microfluidic platforms also allow for the implementation of microphysiological systems that may integrate various sensors and control systems to quantify cellular responses to a controllable mechanochemical microenvironment.

Biomimetic *in vitro* systems, or organ-on-a-chip systems, have shown considerable adaptability by balancing complexity and usability to study key physiological functions in a dynamic setting that cannot be offered through traditional static culture techniques [67]. This technique offers the ability to study cellular responses to various drugs and compounds in conjunction with mechanical stimuli, and has been used in the context of various organs including the lung, kidney, gut, bone, brain, heart, blood vasculature, and liver [67-73]. Devices for examination of endothelial and epithelial cell response to various mechanical and chemical stimuli have used the electrical resistance across the monolayer to monitor the endothelial barrier integrity [69, 73-76]. The electrical measurement, or the transendothelial electrical resistance (TEER), relates the permeability of an endothelial monolayer to the resistance across the endothelial monolayer in units of $\Omega \times \text{cm}^2$. As the endothelial cells proliferate and establish tight and adherens junctions with one another, the TEER value starts to rise before plateauing upon monolayer establishment. If the intercellular junctions are disrupted using inflammatory factors such as TNF- α , the TEER value will drop, reflecting an increase in the permeability of the endothelial layer [73]. Incorporation of this technique in a microfluidic platform for

examination of nanoparticle interactions with the endothelium allows for quantitative measurements for various therapies that may restore endothelial function. The confluence of microfluidics and biomimetic design has enabled accurate, high-throughput microenvironments for high-impact applications including the characterization of drug candidates in clinical studies, reducing the number of costly and highly variable *in vivo* animal models which may differ from the human response [77], as well as improving understanding of cellular responses to specific stimuli which prove difficult to monitor *in vivo*. Advances in *in vitro* model systems, such as 3D cell culture models with advanced materials (e.g. hydrogel), have contributed to a better understanding of the function of human cells and tissues in physiologically relevant environments [78].

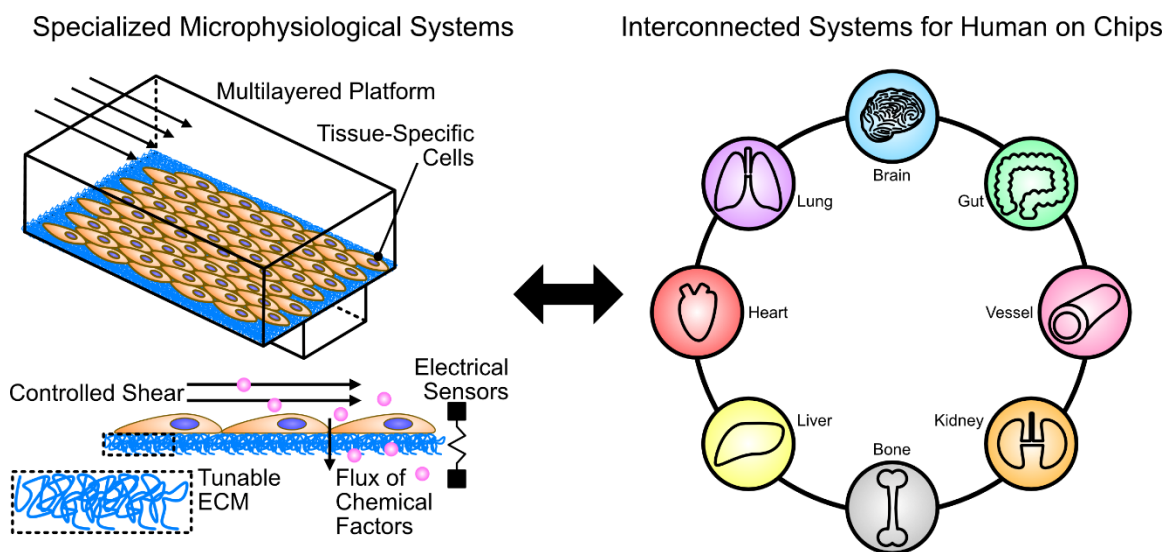


Figure 1.6. Engineering living systems on chips.

Mechanical and chemical cues may be controlled to tune the cellular microenvironment to mimic key *in vivo* conditions critical to tissue-specific cellular function. These tissue-specific microenvironments may be coupled together to develop interconnected systems for the realization of human-on-a-chip platforms for comprehensive drug screening applications.

However, the reproduction of physiologically critical features including dynamically changing mechanical, chemical, and electrical cues to recapitulate fully functional organs still poses technical challenges in the replication of living systems (Fig. 1.6) [79]. Developing physiologically accurate *in vitro* model systems requires precise control of the

dynamic properties at a scale comparable and applicable to human cells, tissues, and organs. Microfluidic technology is well-suited for these model systems by providing precise control over essential model components, including fluid flow, mechanical support, chemical factors, and electrical signals in a dynamically changing cellular microenvironment [80]. For example, compartmentalized microfluidic systems that allow independent control of defined cellular environments have been used in an attempt to reconstitute primary structure and function of human organs [81]. Recent development of model systems that mimic human organs include recapitulating the lung [82], the gut [83], the blood vessels [84], the liver [85], the kidney [86], bone [87], the brain/CNS (e.g. neurons-on-a-chip [88]), and muscle [89]. Development of these devices is a high-impact research area for drug screening in translational medicine and for advanced tissue engineering in regenerative medicine [90]. To better replicate the structure, function, and physiology of human organs, engineering living systems on chips includes the transformative combination of existing technologies from current functional cell and tissue-level test-beds to integrated organ and organism-level platforms.

Despite the potential benefits to fulfilling translational challenges with microfluidic technology, the implementation of microfluidic platforms in the development of nanomedicines is not common due to challenges that are characteristic to a developing technology: (1) a lack of accessibility to specialized tools and skills, and (2) non-standardized protocols for how to implement microfluidic platforms between research groups [11, 91]. The typical fabrication process for microfluidics relies on techniques adopted from the fabrication of micro-electro-mechanical systems (MEMS), which often requires a cleanroom facility with a spin coater and a photomask aligner [92]. In short, the common fabrication steps of a microfluidic device are to (1) spin coat a photocurable polymer onto a silicon wafer, (2) use the photomask aligner to cure the polymer to form a positive mold of the microchannels, (3) mold poly(dimethylsiloxane) (PDMS) to the

patterned silicon wafer to pattern the microchannels into the (PDMS) [92]. Beyond the basic fabrication techniques for microfluidic platforms, there is little standardization for the design and implementation of microfluidic devices for applications like nanoparticle synthesis or biomimicry of the cellular microenvironment. This lack of standardization and accessibility to microfluidic technology motivates this study to apply microfluidics to various processes in the translational pipeline within the context of disease.

1.2 RESEARCH OBJECTIVES

The primary objective of our study is to expand our understanding in the engineering of microfluidic translational tools to aid in the synthesis and screening of nanoparticles. We chose to specifically study engineered HDL-mimetic nanoparticles (eHNPs) in the pathophysiological context of CVD due to HDL's endogenous interactions with endothelial cells to promote an anti-inflammatory cellular response. Studying specific cellular responses to various HDL-components will be achievable not only through the precursor-dependent microfluidic synthesis of eHNPs, but also through high-resolution imaging and endothelial permeability measurements unique to *in vitro* microphysiological systems. To achieve our primary objective, the study is divided into the following aims:

1. Detect the functional differences of microfluidically engineered HDL-mimetic nanoparticles.
2. Engineer a microphysiological system to detect and monitor the endothelial response to a mechanically stimulated CVD pathology.
3. Probe the impact of oscillatory shear stresses on HDL-mimetic nanoparticle interactions with the endothelium.

CHAPTER 2. DETECTING THE FUNCTIONAL DIFFERENCES BETWEEN HIGH-DENSITY LIPOPROTEIN MIMETICS

2.1 ABSTRACT

High-density lipoprotein (HDL) is a key regulator of lipid homeostasis through its native roles like reverse cholesterol transport. The reconstitution of this natural nanoparticle (NP) has become a nexus between nanomedicine and multi-disease therapies, for which a major portion of HDL functionality is attributed to its primary scaffolding protein, apolipoprotein A1 (apoA1). ApoA1-mimetic peptides were formulated as cost-effective alternatives to apoA1-based therapies; reverse-4F (r4F) is one such peptide used as part of a nanoparticle platform. While similarities between r4F- and apoA1-based HDL-mimetic nanoparticles have been identified, key functional differences native to HDL have remained undetected. In the present study, we executed a multidisciplinary approach to uncover these differences by exploring the form, function, and medical applicability of engineered HDL-mimetic NPs (eHNPs) made from r4F (eHNP-r4F) and from apoA1 (eHNP-A1). Comparative analyses of the eHNPs through computational molecular dynamics (MD), advanced microfluidic NP synthesis and screening technologies, and *in vivo* animal model studies extracted distinguishable eHNP characteristics: the eHNPs share identical structural and compositional characteristics with distinct differences in NP stability and organization; eHNP-A1 could more significantly stimulate anti-inflammatory responses characteristic of the scavenger receptor class B type 1 (SR-B1) mediated pathways; and eHNP-A1 could outperform eHNP-r4F in the delivery of a model hydrophobic drug to an *in vivo* tumor. The biomimetic microfluidic technologies and MD simulations uniquely enabled our comparative analysis through which we determined that while eHNP-r4F is a capable NP with properties mimicking natural eHNP-A1, challenges remain in reconstituting the full functionality of NPs naturally

derived from humans. The contents of this chapter were previously published in Biomaterials [66].

2.2 INTRODUCTION

High-density lipoprotein (HDL) is an endogenous nanoparticle (NP) with anti-inflammatory properties and carrier capabilities. With an average diameter of 7-17 nm, HDL naturally transitions between spherical and discoidal configurations with the encapsulation and removal of cholesterol or other hydrophobic molecules from its hydrophobic core [33]. The impact of HDL and its transitioning structure is largely attributed to the functions of its primary protein component, apolipoprotein A1 (apoA1), which serves both as a scaffold to bind free lipids and cholesterol and as an agonist for anti-inflammatory processes like reverse cholesterol transport (RCT) from macrophages and the production of endothelial nitric oxide (NO) [33]. The most common receptors involved in the apoA1-stimulated regulatory processes include scavenger receptor class B type 1 (SR-B1), ATP-binding cassette transporter subfamily A member 1 (ABCA1), and ATP-binding cassette transporter subfamily G member 1 (ABCG1); while ABCA1 and ABCG1 are primarily attributed to RCT from macrophages, SR-B1 has been shown to be involved in both pathways of RCT and endothelial NO production [93]. Being a natural transporter for hydrophobic materials with the added anti-inflammatory benefits, HDL became a prime candidate for transporting therapeutic and diagnostic, or theranostic, agents for a variety of applications [56, 94]. These applications have been applied to engineered NPs mimicking the form and function of HDL, allowing for the additional benefit of controlling the NP composition. Simplifying the complex lipidome and proteome of HDL to apoA1 and phospholipids, the development of HDL-mimetic NPs first started with direct proteo-lipidic self-assembly or the sodium cholate dialysis methods to reconstitute HDL

(rHDL) [95], and has more recently incorporated microfluidic methods for a single-step assembly approach [54].

The engineering of HDL-mimetic NPs should involve a combination of computational and experimental approaches to comprehensively understand the form and function of the resulting NPs. For instance, the discoidal structure of HDL is often presented in a double-belt configuration, which has been commonly implemented in computational models of HDL self-assembly and is used to explain the structural stability of HDL [96-98]. Engineering HDL-mimetics has also resulted in the development of many apoA1-mimetic peptides for synthetic theranostic platforms to be used against diseases like cardiovascular disease (CVD), Alzheimer's disease, diabetes, and cancer [38, 99]. Compared to apoA1, which has more than 240 amino acids, apoA1-mimetic peptides are not sequence homologous and are 18-22 amino acids in length to make the class-A amphipathic helical motif from the apoA1 lipid binding domain (Fig. S2.1) [38]. These mimetic peptides are also relatively cost-effective synthetic alternatives to apoA1, the purification and use of which requires difficult and expensive tests to ensure that human plasma (from which natural apolipoproteins are purified) is infection and endotoxin free [100]. Of the mimetic peptides studied, reverse-4F (r4F) has shown promising results *in vivo* in combatting the pathogenesis of atherosclerotic mouse models, and in the delivery of drug therapeutics [52, 99, 101-103]. The development of r4F was spurred by the varied properties among the 4F and r4F mimetic peptides, of which r4F was engineered to combine the bioavailability of 4F with different lipid-binding and anti-inflammatory properties that were demonstrated in mouse models [101]. NPs formulated with r4F have already shown HDL-like structures and reactivity with the receptor SR-B1 for various theranostic applications [52, 99]. However, a direct comparison of r4F to apoA1 in the context of NP form, function, and drug delivery potential has yet to be conducted.

The applications promised in NP therapies show broad reaches inclusive of imaging agents for targeted areas in the body and treatments for various diseases. With an extensive library of possibilities, different methods have been used to synthesize NPs based on lipids, polymers, proteins/peptides, and their combinations [47]; the most common method is to use bulk benchtop mixing to enhance NP self-assembly, or the spontaneous organization of NP precursors. A major challenge associated with this bulk synthesis technique is the resultant high batch-to-batch variation of the NP physicochemical properties. To address this challenge, microfluidic technology has brought a new synthesis strategy presenting a continuous production platform for highly uniform NPs assembled through controlled mixing patterns (diffusive or convective means) [63], which facilitate precursor microscale interactions that were not achievable through traditional macroscale (centimeter to millimeter) benchtop synthesis techniques.

Additional critical barriers to translational studies for nanomedicine arise from the inability of conventional experimental model systems to conduct mechanistic studies of NP interactions with cells in pathophysiologically relevant microenvironments. Microfluidic technologies also offer a method through which to screen NP interactions with a biological microenvironment through *in vitro* microengineered physiological systems. These *in vitro* platforms, otherwise known as “organ-on-a-chip” systems, are capable of more accurately replicating the physiological tissue environment over traditional *in vitro* assays through the inclusion of key parameters needed for appropriate cellular functionality [104]. In the case of NPs delivered intravenously, studies examining the interactions between NPs and blood-vascular components are of great importance. Substantial research has presented 3D co-culture systems of vascular endothelial cells (ECs) and mural cells (e.g., smooth muscle cells, pericytes, fibroblasts) with a lumen structure that improves the physiological relevance over non-lumen based models [105]. With such a platform commonly used to study endothelial responses such as permeability and angiogenesis [106, 107], probing

the capacity of HDL-mimetics to exert hallmark properties of HDL, such as stimulating the production of endothelial NO [108], is a critical step in their comparative analysis.

In this work, we conducted a comparative analysis between the use of apoA1 and r4F in HDL-mimetics. We first developed and implemented a novel microfluidic platform with which to synthesize engineered HDL-mimetic NPs (eHNPs) made from r4F and apoA1. Through the combined results of experimental and computational NP characterization techniques, our findings initially drew parallels across the various physical and chemical properties shared between the eHNPs including NP structure, size, stability, and composition. We then applied an innovative translational nanomedicine approach by pairing a microengineered vasculature system to screen eHNP function *in vitro* with a murine model to examine eHNP drug delivery to vascularized tumors *in vivo*. Our initial comparisons included eHNP interactions with cells that commonly interact with HDL; we then probed eHNP interactions with macrophages and ECs in the context of prevalent diseases such as CVD and cancer for the purposes of delivering incorporated theranostic agents. Analyzing the computational and experimental results unraveled distinct differences between the eHNPs that were tied to NP stability and the mimicry of hallmark HDL functions linked to the SR-B1 pathway.

2.3 RESULTS AND DISCUSSION

eHNPs share similarities in form, but they have distinct temporal differences

The engineering of NPs benefits from incorporating both computational and experimental methods to comprehensively understand the similarities and differences between different NP formulations. Comparisons between eHNP-A1 and eHNP-r4F made through molecular dynamics (MD) simulations showed similar discoidal structures for the self-assembled NPs (Fig. 2.1A). Transmission electron microscopy (TEM) micrographs

also showed discoidal structures for both eHNP-A1 (Fig. 2.1B) and eHNP-r4F (Fig. 2.1C), the stacking structures of which were artifacts of the negative staining techniques in preparing the eHNPs for TEM imaging [109]. The synthesis of the eHNPs was accomplished using our new microfluidic platform that contains a micropost array to induce the generation of microvortices that propagate down the length of the channel to increase the overall mixing efficiency of the platform (Fig. 2.1D). This microvortex propagation mixer (μ VPM) mixed the precursor solutions more efficiently than our previous approach [54] to form eHNPs with a physiological composition with the addition of the micropost array (Fig. S2.2). With this increased mixing efficiency, synthesizing eHNPs with the μ VPM resulted in highly reproducible and uniform sizes that were more physiologically relevant to natural HDL; the μ VPM yielded particles closer to 10 nm with no lipid aggregates whereas the

platform without microposts yielded NPs greater than 20 nm (Fig. 2.1E). Both eHNPs not

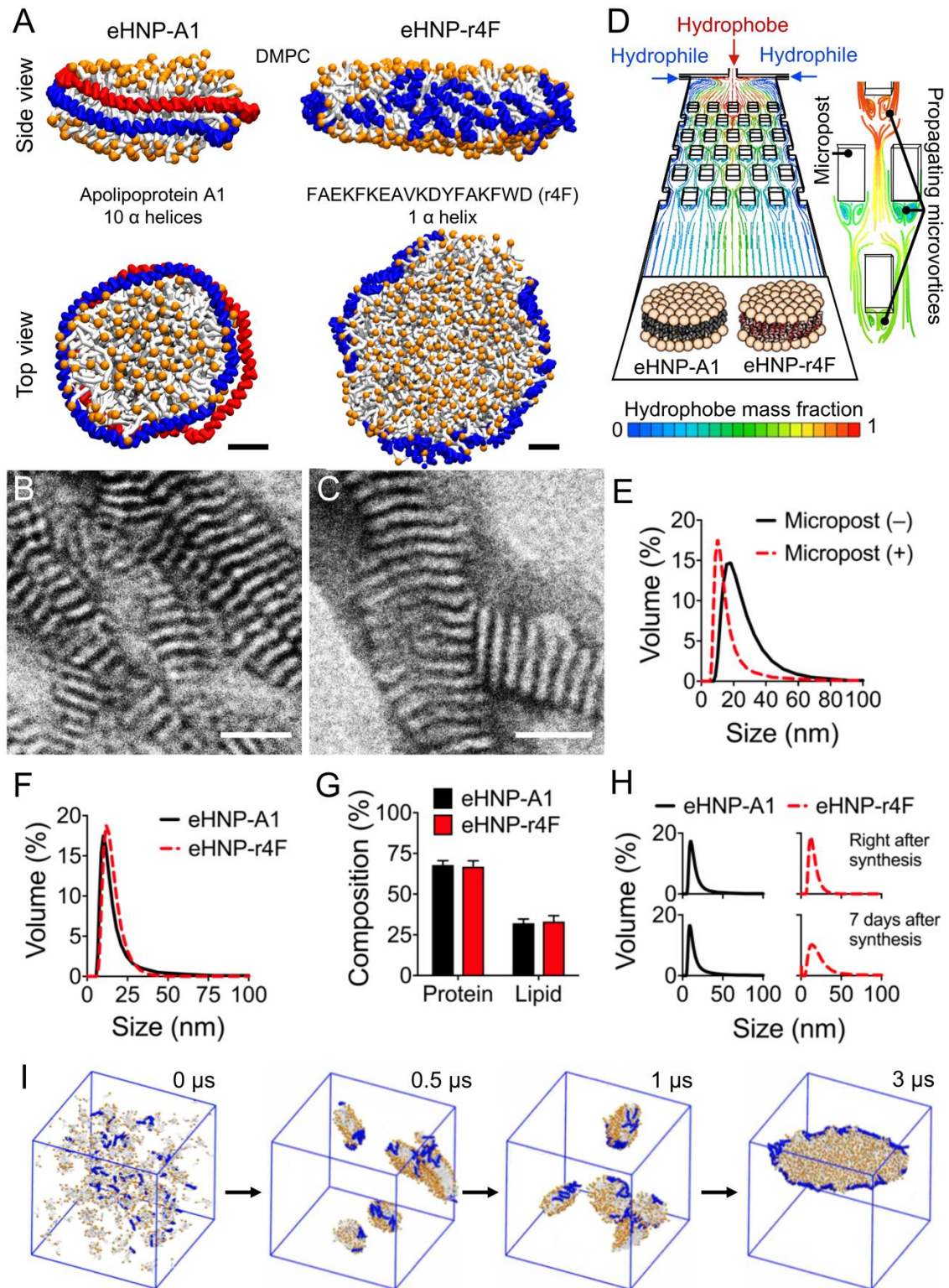


Figure 2.1. Comparison of engineered HDL-mimetic nanoparticles made from apoA1 or r4F.

(A) Molecular dynamics simulations show that 2.3 kDa peptide r4F self-assembles with lipids to produce discoidal eHNPs similar to those made with the 28 kDa apoA1 (scale bar is 2.5 nm). (B, C) TEM images of the synthesized eHNP-A1 (B) and eHNP-r4F (C) particles (scale bar is 25 nm). (D) A microvortex propagation mixer was engineered for the enhanced assembly of the NPs. (E) DLS size distribution of eHNPs synthesized with (+) and without (–) microposts. (F) DLS size distributions of the produced eHNPs. (G) Protein/lipid compositions of the produced eHNPs (n = 3). (H) Stability of the produced eHNPs at 4°C after 7 days post synthesis. (I) eHNP-r4F aggregation over time in a 30 nm simulation box with a trajectory of 3 μ s. Plotted as mean \pm SEM.

only shared this physiological size when synthesized, but they also shared a physiological protein-lipid composition [17]; eHNP-A1 and eHNP-r4F, with average diameters of 10.1 and 11.7 nm respectively (Fig. 2.1F), both had a composition of 65% protein and 35% lipid (Fig. 2.1G). However, in terms of size stability, eHNP-A1 was more stable over the course of a week compared to eHNP-r4F (Fig. 2.1H). The lower size stability of eHNP-r4F may be attributed to the aggregation of eHNP-r4F over time, which is consistent with MD simulations (Fig. 2.1I). The tendency of eHNP-r4F to aggregate may be due to the shorter 18 amino acid peptide length compared to the 240+ amino acids of apoA1. The impact of this difference is shown in the configuration of the scaffolding proteins in the MD simulations; eHNP-A1 consisted of two apoA1 proteins horizontally wrapped around the perimeter of the particle, whereas the smaller r4F peptides in eHNP-r4F were more vertically aligned around the perimeter of the particle. The shorter length of the peptides may facilitate a more dynamic exchange of lipids and peptides between particles that can cause particle aggregation.

eHNP reactivity is shared with macrophages, but not with ECs

With natural HDLs most notably interacting with macrophages and ECs [33], we examined eHNP interactions with these cell types to compare the bioreactivity of eHNP-A1 and eHNP-r4F. Both eHNP-A1 and eHNP-r4F were taken up by J774a.1 macrophages to a similar extent (Fig. 2.2A and B), however eHNP-A1 induced 15% more cholesterol

efflux compared to that of eHNP-r4F (Fig. 2.2C). Competition assays for endothelial and

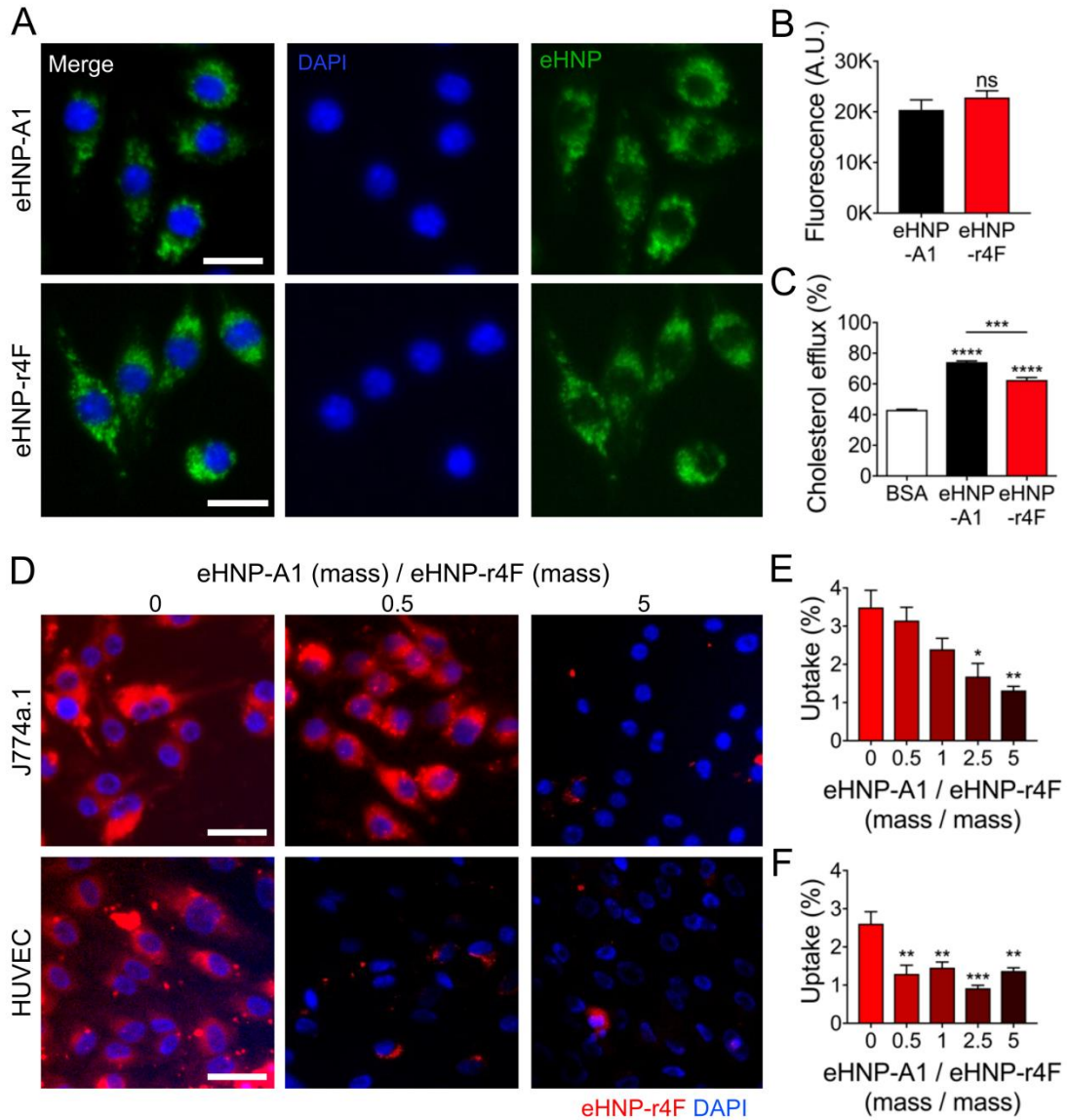


Figure 2.2. Comparison of eHNP bioactivity.

(A) DiO-labeled (green) eHNP uptake by DAPI (blue) labeled J774a.1 macrophages (scale bar is 20 μ m). (B) eHNPs uptake quantified with fluorescence intensity (n = 4). (C) Cholesterol efflux with eHNPs (n = 3). (D) eHNP-A1 and rhodamine-DMPE labeled eHNP-r4F (red) competitive uptake by DAPI (blue) labeled J774a.1 macrophages or HUVECs (scale bar is 50 μ m). (E, F) Comparison of eHNP-r4F retention by J774a.1 macrophages (E) and HUVECs (F) (n = 4). Plotted as mean \pm SEM where *, **, and *** are for p < 0.05, 0.01, and 0.001 respectively.

macrophage uptake of eHNP-A1 and eHNP-r4F also showed distinct difference between these 2 cell types (Fig. 2.2D); while J774a.1 macrophages showed a gradual decrease in uptake of rhodamine-labeled eHNP-r4F with the introduction of eHNP-A1 (Fig. 2.2E),

human umbilical vein ECs (HUVECs) showed more than a 2-fold decrease in eHNP-r4F uptake when adding an amount of eHNP-A1 equivalent to just half the amount of eHNP-r4F (Fig. 2.2F). While ECs and macrophages share certain HDL receptors such as SR-B1, ABCA1, and ABCG1, macrophages express more scavenger receptors, such as scavenger receptor class A (SR-A) [93], that allow macrophages to exhibit uptake characteristics that are less selective than those of ECs. This lack of selectivity may contribute to the lack of retardation in the J774a.1 uptake of eHNP-r4F with the addition of eHNP-A1. In addition, the differences between eHNP reactivity may be tied specifically to the receptor SR-B1 as seen with the differences in the cholesterol efflux measurements (Fig. 2.2C). Although the amino acid sequences between murine and human SR-B1 are 80% homologous, it should be noted that both murine and human models are appropriate for studying human lipoproteins [110, 111]. Since inhibition of SR-B1 in ECs does not necessarily completely inhibit the uptake of eHNPs due to redundant HDL uptake pathways [112], we determined it was necessary to examine hallmark endothelial responses to HDL that are classically stimulated through SR-B1 triggered pathways: the production of endothelial NO and its downstream anti-inflammatory effects [108].

Anti-inflammatory endothelial responses are more prominent with eHNP-A1

To further explore the preferential endothelial uptake of eHNP-A1 over eHNP-r4F, we used a microengineered vascular system (Fig. 2.3A) to measure 2 hallmark markers to quantify endothelial inflammation: the levels of endothelial NO production and the expression of intercellular adhesion molecule 1 (ICAM-1) [106]. While the responses of the microvascular network to the eHNPs were similar across all measurements for both eHNP-A1 and eHNP-r4F, the responses were more underscored in the cases of eHNP-A1 exposure. Both eHNPs were able to significantly stimulate endothelial NO synthase

(eNOS) and promote NO production, however eHNP-A1 elicited more than double the NO

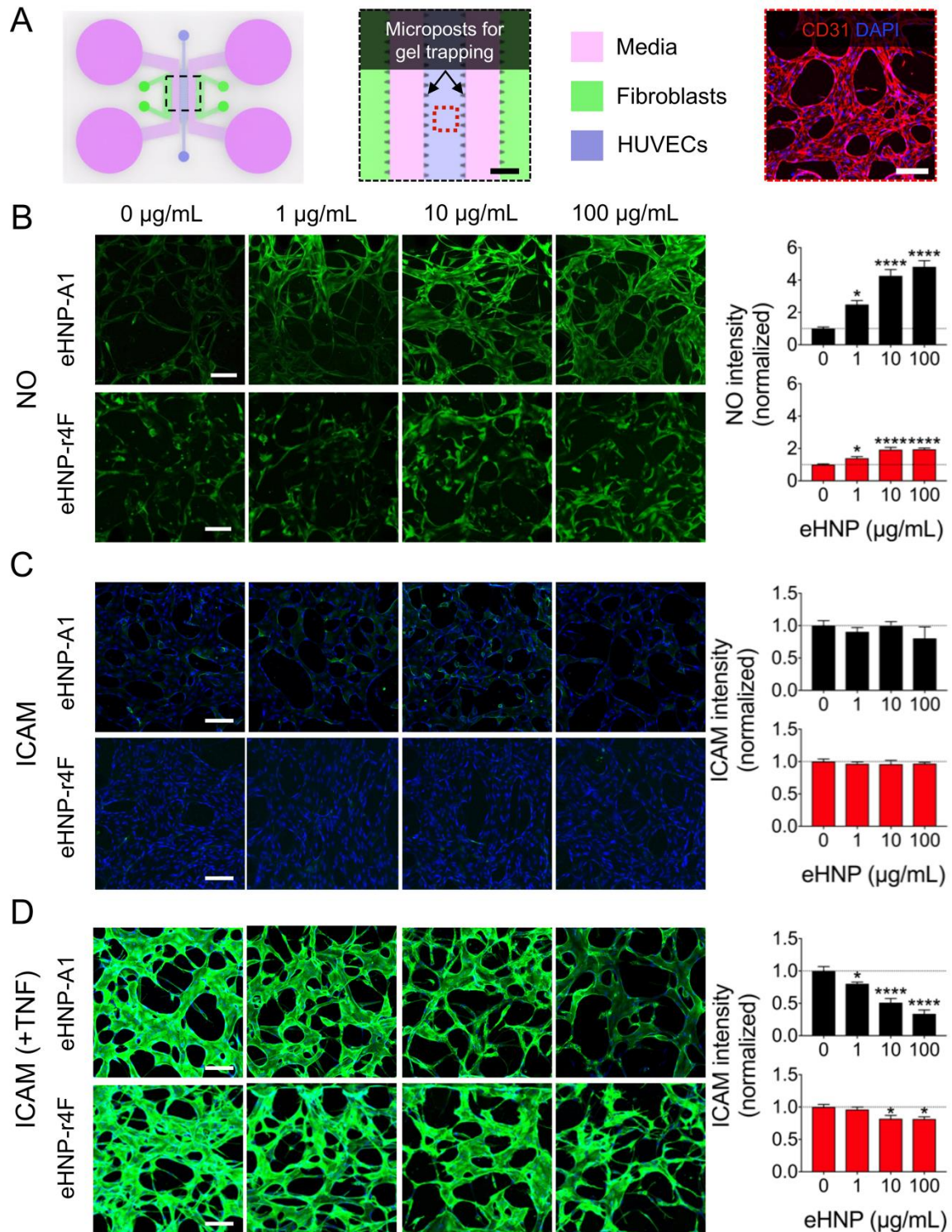


Figure 2.3. Endothelial response to eHNPs in microengineered vascular system.

(A) A schematic of a microengineered vascular system (Scale bar is 500 μm) that was used to screen the endothelial responses to eHNP-A1 and eHNP-r4F (Scale bar is 100 μm). (B-D) The endothelial responses to eHNP-A1 and eHNP-r4F were compared through nitric oxide (NO)

production (B) and ICAM expression (C) with and without the presence of TNF- α (D) (Scale bar is 100 μ m, n = 4-8). Plotted as mean \pm SEM where * and **** are for $p < 0.05$ and 0.0001 respectively.

levels compared to the levels eHNP-r4F stimulated (Fig. 2.3B). A primary marker of the endothelial inflammatory process is with the expression of surface adhesion proteins; endothelial cells activated through mechanochemical stimuli such as oscillatory shear stress or inflammatory cytokines like tumor necrosis factor α (TNF- α) express several adhesion proteins, including vascular cell adhesion molecule (VCAM-1), ICAM-1, and E-selectin [33]. The ability of HDL to inhibit cytokine-induced adhesion molecule expression has been demonstrated in the protective function against the development of atherosclerosis [113]. As seen with apoA1-based reconstituted HDLs (rHDL), both eHNPs did not trigger ICAM-1 expression (Fig. 2.3C) and were able to significantly reduce ICAM-1 levels induced with TNF- α stimulation (Fig. 2.3D) [114, 115]. In line with the magnified effects of eHNP-A1 on NO production however, the reduction of ICAM-1 was more than twice as prominent with eHNP-A1. These results are consistent with the competition assay (Fig. 2.2F) in that HUVECs responded more preferentially in the uptake of eHNP-A1 over eHNP-r4F. While both eHNPs could trigger SR-B1 related processes in ECs, eHNP-A1 outperformed eHNP-r4F in the magnitude to which these processes were stimulated.

DOX delivery to HL-60 is facilitated with eHNPs

The use of HDL and HDL-mimetics for therapeutic and diagnostic multi-disease applications is widely being explored due to its natural role as a stable transport vehicle for hydrophobic materials through the body [52, 94]. In the case of chemotherapeutics, patient treatments employing anthracyclines have been connected to cardiovascular side effects such as acute ischemic heart disease that are typically a result of atherosclerosis [116]. With the known cardioprotective properties of apoA1 and HDL, we examined the

drug delivery potential of eHNP-A1 and eHNP-r4F in the context of delivering

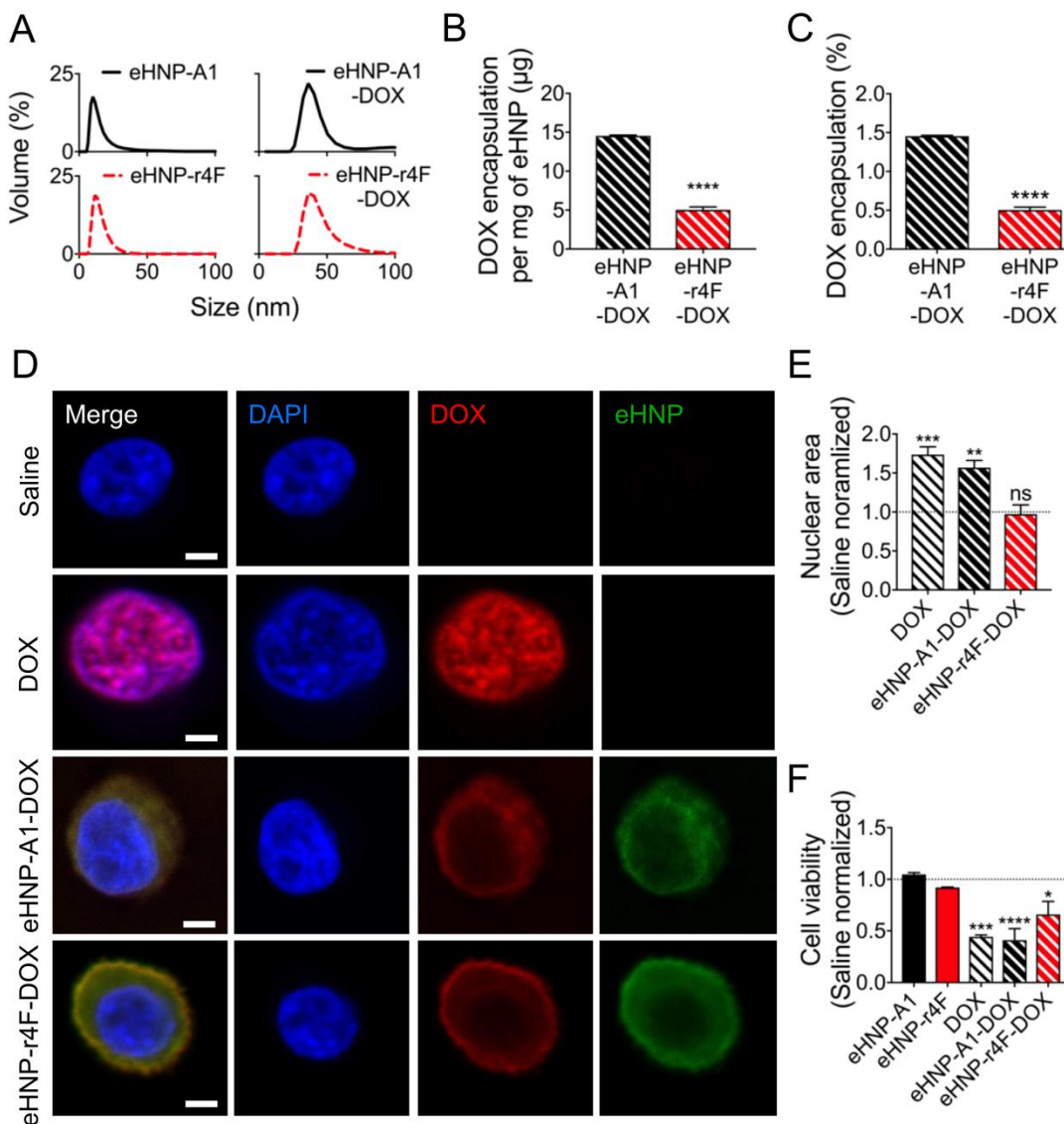


Figure 2.4. Incorporating DOX into eHNPs for in vitro delivery.

(A) DLS comparison of eHNP-A1-DOX and eHNP-r4F-DOX to eHNP-A1 and eHNP-r4F respectively. (B, C) Mass (B) and efficiency (C) of DOX loading into eHNPs (n = 3). (D) Co-localization of eHNP (green) and DOX (red) signal in HL-60 cells after 4 h of incubation (Scale bar is 5 µm). (E) Nuclear area of HL-60 cells in response to 4 h DOX treatment (n = 5-14). (F) Cancer cell (HL-60) viability after a 24 h incubation with DOX treatment (150 ng of DOX) (n = 3). Plotted as mean ± SEM where *, **, ***, and **** are for p < 0.05, 0.01, 0.001, and 0.0001 respectively.

anthracyclines. As a proof of concept for this notion, we incorporated a widely used anthracycline cancer drug, doxorubicin hydrochloride (DOX), into the eHNPs for which the resulting size distributions interestingly yielded similar peaks at 40 nm when adding equal

initial amounts of DOX to the synthesis of both eHNP types (Fig. 2.4A). Again, it is interesting that eHNP-r4F-DOX had the same size as eHNP-A1-DOX that uses a 10X larger scaffolding protein to incorporate this model drug. To confirm the presence of DOX in our eHNPs, we found that eHNP-A1-DOX had an improved loading concentration and encapsulation efficiency over eHNP-r4F-DOX with efficiencies of 1.5% and 0.5% respectively (Fig. 2.4B and C); the encapsulation efficiency, without additional conjugation between drugs and NPs, was comparable to values reported by other studies for HDL platforms used for drug encapsulation [56]. The discrepancy in DOX incorporation between eHNP-A1-DOX and eHNP-r4F-DOX may be a result of the weaker stabilizing intermolecular forces of r4F than those available to apoA1 [98]; this difference in stability was also observed with drug-free eHNPs in the context of size stability (Fig. 2.1H).

Having diseases treated with anthracyclines in mind, we cultured acute myeloid leukemia (AML) HL-60 promyeoblasts and administered our newly synthesized eHNP-DOX with either r4F or apoA1 and an equivalent amount of DOX. The examination of the short-term (4 h) uptake of eHNP-A1-DOX and eHNP-r4F-DOX by HL-60 cells showed the eHNPs and DOX fluorescent signals co-localized primarily in the same region of the cell cytoplasm (Fig. 2.4D). Compared to the naked DOX case for which DOX translocated into the nucleus, our eHNPs facilitated the delivery of DOX into this cancer cell with slower translocation of DOX into the nucleus [117]. It should also be noted that the HL-60 cells treated with naked DOX and eHNP-A1-DOX exhibited more swollen nuclei than the HL-60 cells treated with eHNP-r4F-DOX and saline (Fig. 2.4E); nuclear swelling is a characteristic of DOX treatment [118]. This difference in HL-60 morphology may be due to a difference in uptake between eHNP-A1-DOX and eHNP-r4F-DOX, for which we tested the cytotoxicity of the eHNPs. Over the course of a 24 h culture, we found significant drops in the HL-60 cell viability with eHNP-r4F-DOX and eHNP-A1-DOX (Fig. 2.4F). The cytotoxicity to the HL-60 cells proved to be more significant with eHNP-A1-DOX than with

eHNP-r4F-DOX, which was consistent with the DOX-induced nuclear effects that were observed in the confocal microscopy results.

To further explore the capabilities of both eHNP-A1 and eHNP-r4F in the context of drug delivery, we studied the tumor uptake of near-infrared (NIR) dye labeled eHNPs delivering DOX in a murine xenograft tumor model of HL-60 cells. The biodistribution of the eHNPs with DOX measured using an *in vivo* imaging system (IVIS) showed a distinct difference in the distribution between eHNP-A1-DOX and eHNP-r4F-DOX; eHNP-A1-DOX accumulation was significantly higher in the lung, kidney, spleen, and the tumor (Fig. 2.5A). Confocal imaging of the cyrosectioned tumor samples showed less delivery of DOX to the tumor site with the naked DOX treatment compared to the eHNP-DOX treatments (Fig. 2.5B), between which eHNP-A1-DOX treated mice showed the highest particle (Fig. 2.5C) and DOX (Fig. 2.5D) uptake by the tumor. The co-localization of eHNP and DOX signals in the tumor sections (Fig. 2.5B) was also consistent with the *in vitro* results (Fig. 2.4D). The discrepancy between eHNP-A1 and eHNP-r4F accumulation in the tumor may be dependent on the interactions between the eHNPs and the tumor microenvironment, which has been shown to be especially important in tumor growth through processes like angiogenesis [119].

Our previous work has shown that eHNP-A1 can interact with the endothelium to modulate the angiogenic process [107]. It has also been shown that the HDL-sensitive receptor SR-B1 is overexpressed in some cancers including myeloid leukemia [120]. Potential modes of SR-B1 mediated eHNP tumor retention include interactions with the tumor endothelium or the HL-60 tumor cells [93]. Thus, the differences between eHNP-A1-DOX interactions with the tumor over those of eHNP-r4F-DOX may be due to increased EC and/or HL-60 tumor cell interactions with eHNP-A1, which was already demonstrated with our *in vitro* results (Fig. 2.2-4). In addition, the lower stability of eHNP-r4F we found (Fig. 2.1H and I) may have affected the functionality through eHNP-r4F

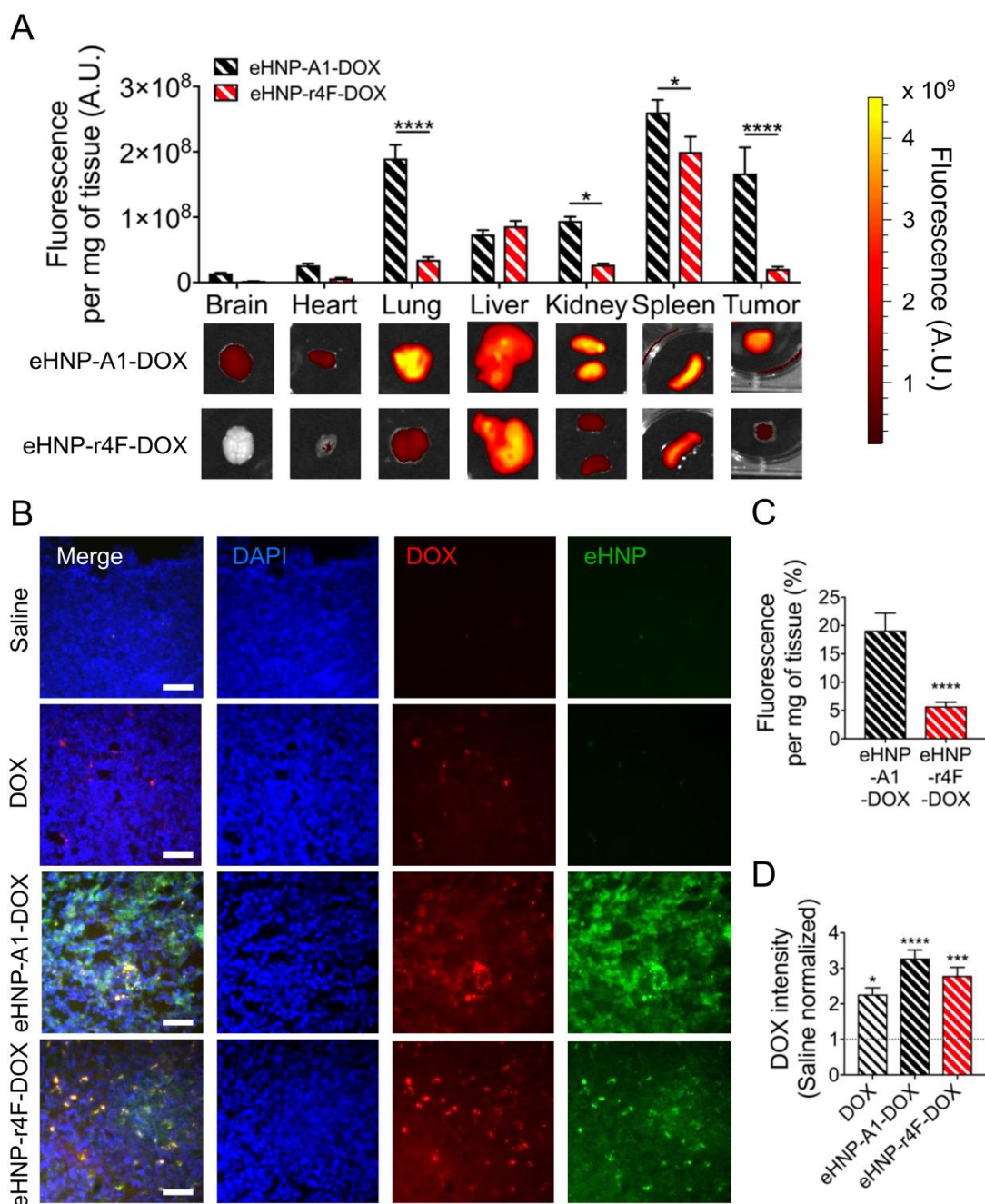


Figure 2.5. eHNP-facilitated DOX delivery to xenograft tumor in a murine model.

(A) Biodistribution of DiR labeled eHNPs loaded with DOX ($n = 7$). (B) Confocal images of DiR labeled eHNPs (pseudo-colored green) and DOX (red) in DAPI (blue) labeled HL-60 tumor sections (scale bar is 50 μm). (C) Biodistribution of eHNPs to the tumor site ($n = 7$). (D) DOX fluorescence intensity measurements in tumors (DOX: $n = 4$; eHNPs: $n = 7$). Plotted as mean \pm SEM where *, **, and **** are for $p < 0.05$, 0.001, and 0.0001 respectively.

aggregation *in vivo*, resulting in a different pharmacokinetic profile in the biodistribution of eHNP-r4F-DOX. Therefore, while r4F has potential in disease theranostics through the

retention of some of apoA1's properties, the challenge remains in fully mimicking the complex functions of apoA1 and other HDL associated proteins to stimulate key functional, and potentially therapeutic, cellular responses.

2.4 CONCLUSIONS

HDL-mimetics offer a multitude of avenues through which to explore disease therapy. We found that eHNP-r4F was comparable to eHNP-A1 in the basic physicochemical properties: size, structure, and composition. However, eHNP-A1 could elicit cellular responses such as cholesterol efflux from macrophages and NO production in ECs at a higher level than eHNP-r4F. When further compared to eHNP-r4F, eHNP-A1 more preferentially interacted with HUVECs and significantly reduced TNF- α stimulated ICAM-1 expression in the microvascular networks. In the context of drug delivery, eHNP-A1 was also better able to incorporate and deliver DOX to the tumor cells *in vitro* and *in vivo*. However, it should be noted that eHNP-r4F was still able to deliver more doxorubicin to the tumor site over the naked DOX treatment *in vivo*. More studies are needed to elucidate the possibilities of using apoA1-based nanocarriers like our eHNPs, as the development of apoA1-mimetic peptides such as r4F may be able to serve as a cost-effective alternative to apoA1. However, it is clear from our study that apoA1 has many properties that cannot yet be fully recapitulated using the apoA1-mimetic peptide r4F. Additional future work to be considered would be in the incorporation of other HDL-associated proteins and small molecules that modulate the functionality of HDL. By leveraging the combined insights provided from experimental and computational approaches, we may examine the functionality of eHNPs with these added components to further analyze one of the most complex and heterogeneous transporters of the body.

2.5 METHODS

eHNP synthesis materials

1,2-dimyristoyl-sn-glycero-3-phosphocholine (DMPC) and 1,2-dimyristoyl-sn-glycero-3-phosphoethanolamine-N-(lissamine rhodamine B sulfonyl) (Rhodamine-DMPE) were purchased from Avanti Polar Lipids, Inc. (Alabaster, AL). The near-infrared label for the eHNPs, 1,1'-Dioctadecyl-3,3,3',3'-Tetramethylindotricarbocyanine Iodide (DiR), was purchased from Thermo Fisher Scientific (Waltham, MA). ApoA1 from human plasma, 3,3'-dioctadecyloxacarbocyanine perchlorate (DiO), and DOX were purchased from Sigma-Aldrich Co. LLC. (St. Louis, MO). The peptide r4F was purchased from RS Synthesis, LLC. (Louisville, KY) using the sequence Ac-FAEKFKAEVVKDYFAKFWD [99]. Polydimethylsiloxane (PDMS) for fabrication of the μ VPM synthesis platform was made using the Sylgard 184 silicone elastomer kit purchased from Dow Corning Corporation (Auburn, MI).

Molecular dynamics simulations

The MD simulations were performed using the GROMACS software package [121]. The coarse grain model for the simulations was done with the MARTINI coarse grain force field for biomolecular systems [122]. Combining the ElneDyn elastic network model with the coarse grain molecular force field to maintain the secondary and tertiary structure of apoA1, we simulated the self-assembly of eHNP-A1 in a 15 x 15 x 15 nm simulation box with a periodic boundary and a trajectory of 500 ns [123]. The initial conditions of the simulation involved 2 apoA1 molecules arranged in antiparallel around 160 DMPC lipids using the *insane* method for lipid bilayers [124]. Using the same boundary box size of 15 x 15 x 15 nm and number of lipids, we initiated 1 μ s trajectory eHNP-r4F simulations with varying protein:lipid molecular ratios based on our eHNP-A1 simulations and on past

simulations using the apoA1-mimetic peptides 18A and 4F (Table S3.1) [125, 126]. To examine the aggregation of multiple eHNP-r4F particles, we used the initial conditions of a 30 x 30 x 30 nm simulation box and a protein:lipid molecular ratio of 1:16 for a trajectory of 3.5 μ s [125].

μ VPM design, analysis, and fabrication

The μ VPM was first conceptualized from previous platform designs using the CAD software SolidWorks from Dassault Systemes SolidWorks Corp. (Paris, France), after which we conducted computational flow studies using the solver SC/Tetra (Software Cradle Co., Ltd., Osaka, Japan) [59, 63, 127]. The diffusion coefficient was set for 10^{-9} m²/s for a small molecule in water at room temperature as previously determined [61]. Fabrication of prototype devices using PDMS allowed us to conduct flow visualization studies using phenol red and water imaged with an EVOS FL Auto microscope from ThermoFisher Scientific (Waltham, MA). Starting from reference inlet ratios and flowrates [54], we adjusted the flowrates of the phenol red and water while simultaneously comparing them to results yielded from the computational analysis. To evaluate the mixing efficiencies of the μ VPM, we used a mixing index to compare the lipid mass fraction distributions of the channel cross sections to reduce the under-mixed lipid mass fraction at the outlet (Fig. S2.2) [64]. The μ VPM uses three inlets and a single outlet, with a height of 100 μ m, outlet width of 2 mm, and 27 microposts with the dimensions 200 x 400 μ m. For the device fabrication, SU-8 was spun onto 100 mm silicon wafers to a height of 100 μ m before undergoing photolithography. The wafers were developed and dried before casting. PDMS was molded to the patterned silicon wafer using a 10:1 mass ratio of elastomer to curing agent before curing at 80°C. Molded devices were then bonded to glass slides using the PDC-32G plasma cleaner from Harrick Plasma (Ithaca, NY) for 1 minute.

eHNP synthesis and characterization

The synthesis conditions used for all NPs were with a Reynolds number of 50, where the flow ratio between the side streams and the center stream was 5.5:1 respectively. The NP precursor solutions included a lipid solution that was composed of DMPC with a concentration of 2.75 mg/mL in 200 proof ethanol, and a protein solution that had either apoA1 or r4F with a concentration of 0.2 mg/mL in PBS (1X, pH 7.4). Syringe pumps from Harvard Apparatus (Holliston, MA) were used to pump the solutions into the device, from which the mixed solution was collected and then triple washed with PBS using a 10,000 M.W. (30,000 M.W. when incorporating DOX or fluorescent labels) centrifugal filter from EMD Millipore Corporation (Darmstadt, Germany) at a speed of 3900 rpm for 20 minutes. The size distribution of the final washed sample was measured with a Zetasizer Nano ZS from Malvern Instruments (Worcestershire, United Kingdom). Protein and lipid precursor compositions between eHNP-A1 (Fig. S2.3) and eHNP-r4F (Fig. S2.4) were tuned to achieve an average size of 10 nm. Fluorescently labeled eHNPs used a modified lipid precursor solution with Rhodamine-DMPE, DiR, or DiO as 15% of the total lipid mass [52, 102]. Incorporation of DOX into the eHNP was done through mixing the protein precursor solution to accommodate a 1 mg/mL solution of DOX in DMSO for a final precursor solution containing 0.2 mg/mL of both apoA1 (or r4F) and DOX. The protein-DOX precursor was then microfluidically mixed with the lipid precursor followed by a triple wash in PBS all in the same way as for when synthesizing eHNPs without DOX. eHNP-DOX samples were placed into black well, clear bottom 96 wells plates and measured using the excitation/emission wavelengths of 490/580 nm [128, 129]. Samples were measured using with a Cytation 5 plate reader from BioTek (Winooski, VT). The Schiffer-Edmunson diagrams were made using the Membrane Protein Explorer (MPEx) research tool [130].

TEM preparation

Samples for TEM were prepared on nickel grids with a formvar coating from Electron Microscopy Sciences (Hatfield, PA). The NPs to be imaged were triple washed in an ammonium acetate buffer. The NPs were then loaded onto the TEM grids before they were negatively stained using a 2% phosphotungstic acid solution (PTA). The final samples were then imaged on an HT7700 TEM (Hitachi, Tokyo, Japan) at 120 kV coupled with the DigitalMicrograph camera and software suite from Gatan (Pleasanton, CA).

eHNP protein and lipid quantification

Protein quantification was done using the colorimetric Micro BCA Protein Assay kit from ThermoFisher. As per the recommendations from the instructions, SDS (1%) was added to all samples to prevent the interference of lipids on the protein measurement. Lipid quantification was done using the fluorometric Lipid Quantification Kit (neutral lipids) from Cell Biolabs, Inc. (San Diego, CA).

Cell culture

The macrophage adherent cell line J774a.1 from ATCC (Manassas, VA) was cultured in Dulbecco's Modified Eagle Medium supplemented with 1% penicillin streptomycin (PS) and 10% Fetal Bovine Serum (FBS). Human umbilical vein endothelial cells (HUVECs) were purchased from Lonza (Basel, Switzerland), and were cultured using complete endothelial growth medium 2 (EGM-2). Normal human lung fibroblasts (LFs, Lonza) were cultured in Fibroblast Growth Medium (FGM-2, Lonza); cell passages 3-4 were used for the microengineered vascular experiments. Human promyeoblast suspension cell line HL-60 originally purchased from ATCC, cultured in complete medium

consisting of Iscove's Modified Dulbecco's Medium supplemented with 20% FBS and 1% PS. Media was refreshed every 3 days.

eHNP uptake and competition assay

HUVECs and J774a.1 were cultured for 24 hours in a 96-well plate before triple washing with PBS and adding culture media with rhodamine-DMPE labeled eHNP-r4F (20 $\mu\text{g/mL}$ of protein) and/or eHNP-A1 (0, 10, 20, 50, or 100 $\mu\text{g/mL}$ of protein) overnight at 37°C. The cells were then triple washed with PBS before fixation with 4% paraformaldehyde and counter staining with DAPI. Samples were then imaged and the fluorescent intensity was analyzed using the Cytation 5 plate reader from BioTek.

Cholesterol efflux assay

J774a.1 cells were cultured in 96 well-plates (black well, clear bottom) at a density of 12,500 cells/well. Plates were cultured for 24 h before adding NBD cholesterol (ThermoFisher Scientific) overnight at a concentration of 100 $\mu\text{g/mL}$. The cells were washed the next day with PBS before incubating with 2 mg/mL fatty-acid free albumin overnight. Cells were then washed and incubated with eHNPs or BSA for 16 h. Supernatant media from each well was extracted and cells were washed with PBS. Supernatant and cell samples were measured with a Cytation 5 plate reader from BioTek using the excitation/emission wavelengths of 469/537 nm.

Cell seeding in the microengineered vascular system

A previously reported microengineered vascular system designed to probe endothelial cell responses in a 3D vascularized network was used to examine endothelial interactions with our eHNPs [65, 106, 131]. To fabricate the devices, SU-8 was spun onto 100 mm silicon wafers to a height of 100 μm before undergoing photolithography. The

wafers were developed and dried before casting. PDMS was molded to the patterned silicon wafer using a 10:1 mass ratio of elastomer to curing agent before curing at 80°C. Molded devices were then bonded to glass slides using the PDC-32G plasma cleaner from Harrick Plasma (Ithaca, NY) for 1 minute. Fibrinogen (Sigma) was dissolved in DPBS (w/calcium and magnesium, Gibco), filter-sterilized (0.22 µm pore) and then supplemented with aprotinin (0.15 U/mL, Sigma). Fibroblasts were re-suspended in the fibrinogen solution (2.5 mg/mL) at a concentration of 8×10^6 cells/mL. The cell solution was mixed with thrombin (1 U/mL, Sigma) immediately prior to injection into fibroblast channels. Following 3 minutes of polymerization at room temperature. The central channel was filled in the same manner as the peripheral channels; HUVECs were introduced into the gel at a concentration of 5×10^6 cells/mL instead of fibroblasts. After allowing the gels to polymerize for 3 minutes at room temperature, the inlet reservoirs of the cell culture medium channels were filled with EGM-2 medium, and then aspirated to fill the hydrophobic channels (Fig. S2.5). Following loading all four reservoirs, the microfluidic platforms were incubated at 37 °C for 5 days to allow for microvascular network formation (Fig. S2.6). Experiments were conducted under static conditions.

Quantifying endothelial NO production and ICAM expression

The perfusates were supplemented with L-arginine (5 mM, Sigma) and DAF-FM DA (5 µM, Molecular Probes) to support and detect the NO production by HUVECs. The levels of NO were quantified via confocal microscopy and the fluorescent intensity was analyzed with ImageJ. The background fluorescence of each image was eliminated to compare NO levels between different dosage conditions, and the total fluorescence was normalized to the 0 µg/mL dosage for comparisons between eHNP-A1 and eHNP-r4F. Z-stack projections were collected to obtain an average intensity value for each chip. To compare the effect of the eHNPs on ICAM-1 expression, each microvascular network was

pre-incubated with each dosage of eHNP (0, 1, 10 and 100 $\mu\text{g/mL}$) for 16 h before exposure to TNF- α (50 ng/mL) to maximize inhibition of ICAM-1 expression [114]. During TNF- α activation for 4 h, the concentration of eHNP was maintained. The devices were then fixed and stained for ICAM-1 expression before comparing the fluorescence intensity between the eHNP dosages with confocal microscopy. The fluorescence intensities were normalized to the 0 $\mu\text{g/mL}$ eHNP dosage. ICAM-1 expression without TNF- α was quantified in the same way with the exclusion of the TNF- α incubation step.

Immunostaining in microengineered vascular system

For immunofluorescence staining, cells in the device were fixed using 4% PFA for 15 minutes at room temperature (RT), permeabilized with Triton X-100 (0.15% v/v in PBS) for 15 minutes, and then blocked in bovine serum albumin (BSA 3% w/v in PBS) for 1 h at room temperature. Monoclonal antibodies specific for human ZO-1 (Alexa Fluor 488) were purchased from Thermo Fisher, CD31 (Alexa Fluor 647) were purchased from BioLegend and Hoechst 3342 were purchased from Molecular Probes. Mouse monoclonal antibodies specific for ICAM-1 (Alexa Fluor 488) were purchased from BioLegend. All the samples were washed three times and stored in PBS before imaging.

Cell viability assay

Trypan blue was used to evaluate the viability of HL-60 cells counted in a Countess II FL Auto from Life Technologies. Cells were cultured at 37°C in complete medium with Iscove's Modified Dulbecco's Medium and 20% FBS in a 96 well at a density of 20,000 cells/well. Viability was measured in triplicate every 24 h after addition of eHNPs and DOX at a dosage of 150 ng. The amount of eHNPs to be administered to achieve the appropriate DOX dosage was determined through the characterization of DOX loading

into the eHNPs (Fig. S2.7). All measurements were normalized to HL-60 cell samples cultured without the addition of eHNPs or DOX.

Co-localization of eHNPs and DOX

eHNPs were synthesized using a rhodamine-DMPE lipid to allow for visualization of both eHNPs and DOX. HL-60 cells were incubated with either eHNP-r4F-DOX or eHNP-A1-DOX for 4 h before being fixed for 15 minutes with 4% PFA at RT and spun onto poly-L-lysine coated glass coverslips and mounted to glass slides using VectaShield (Vector Laboratories, Burlingame, CA) with DAPI counterstain prior to fluorescent imaging with a LSM 700 confocal microscope from ZEISS (Oberkochen, Germany) [132, 133]. Images were pseudo-colored for consistency through the study; green for eHNPs, red for DOX, and blue for DAPI.

Murine xenograft tumor biodistribution of eHNPs

Nude female balb/c mice were ordered at 5 weeks of age and allowed to acclimate to the lab facility conditions for 1 week on an irradiated dietary regiment. Two million HL-60 cells were injected in 100 μ L of PBS into the rear right flank of the mouse. To maximize the amount of DOX delivered by the IVIS-trackable eHNPs, increasing amounts of DOX were added to the hydrophobic precursor with DiR to find an upper limit of loaded DOX. Using the 5:1 mass ratio between DOX and protein, a 200 μ L tail vein injection of saline, DOX, eHNP-A1-DOX, or eHNP-r4F-DOX was administered to the mouse after its tumor reached at least 100 mm³ in volume as measured by digital calipers (Fig. S2.8). The dosages for the injections were 5 mg/kg of protein, equivalent to 0.25 mg/kg of DOX. The animals were sacrificed and perfused with saline and 4% PFA for 15 minutes at RT 24 h after the tail-vein injection to allow for uptake of the eHNPs (12 h half-life for both) into the tumor [102, 134]. This 24 h time point was also consistent with the *in vitro* cytotoxicity

assay. The harvested organs were then imaged for their DiR content using an *in vivo* imaging system (IVIS) from Perkin Elmer (Waltham, MA) (Fig. S2.9). The organ masses were measured on a scale, and the biodistribution data was calculated from the IVIS data (Fig. S2.10). The tumors were first cryosectioned and mounted onto glass slides using the antifade mounting medium with DAPI (H-1200) from Vector Laboratories (Burlingame, CA) before being imaged under a confocal microscope (Zeiss LSM 780) [135]. Image analysis of the tumors was done using ImageJ for 3 sections per tumor.

Statistical Analysis

Statistical analyses were run in Prism 7 (GraphPad Software Inc, La Jolla, CA) and significance was defined as $P < 0.05$ (*). Statistical significance analysis was done via *t* tests or ANOVA.

2.6 SUPPLEMENTARY INFORMATION

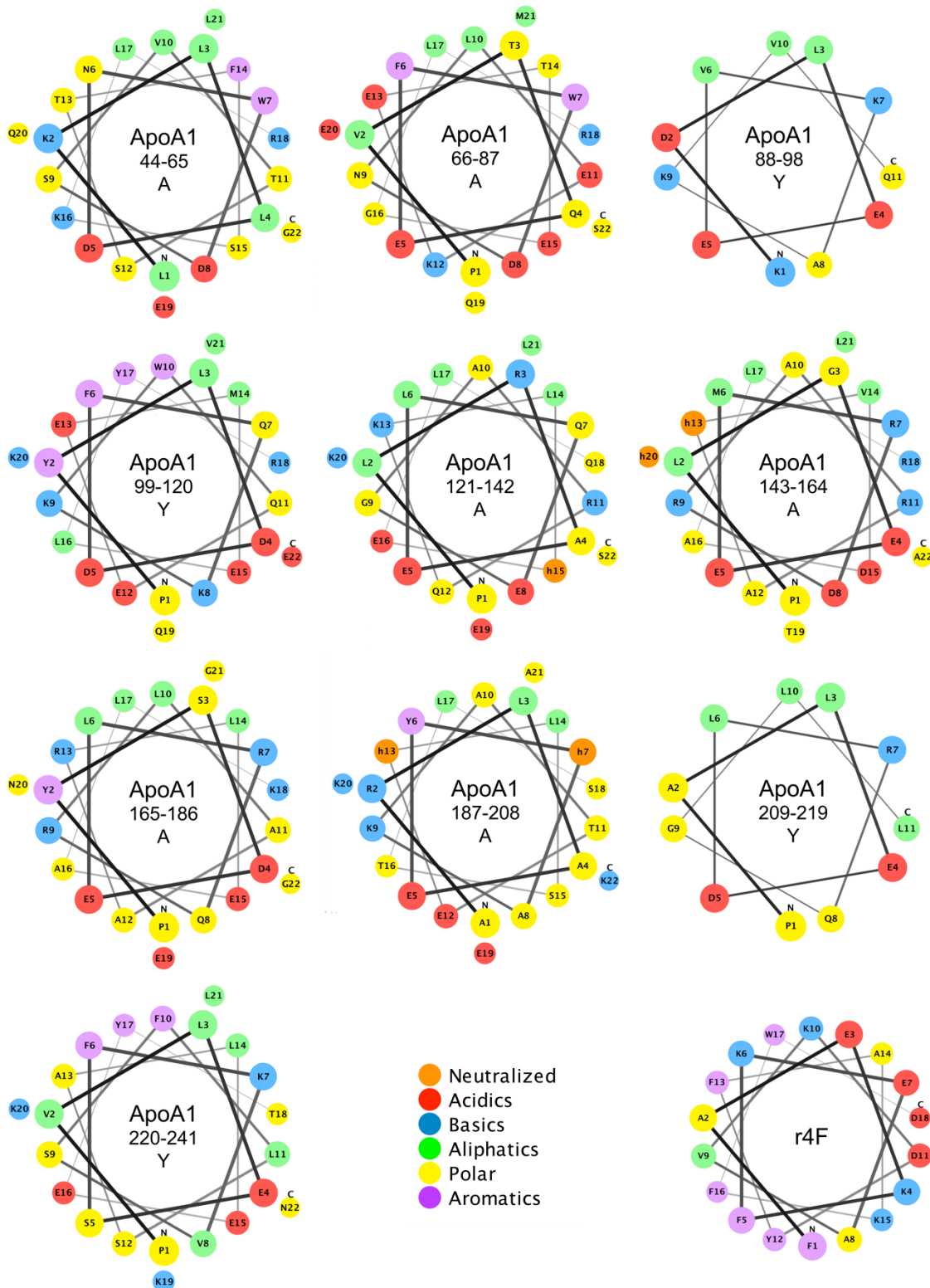


Figure S2.1. Schiffer-Edmunson diagram for r4F and the 10 alpha helices of apoA1.

The r4F peptide is not homologous to any of the apoA1 helices, however it mimics the class A helices that characteristically have a high mean hydrophobic moment with negative charges in the center of the polar face and positive charges near the polar-nonpolar interfaces.

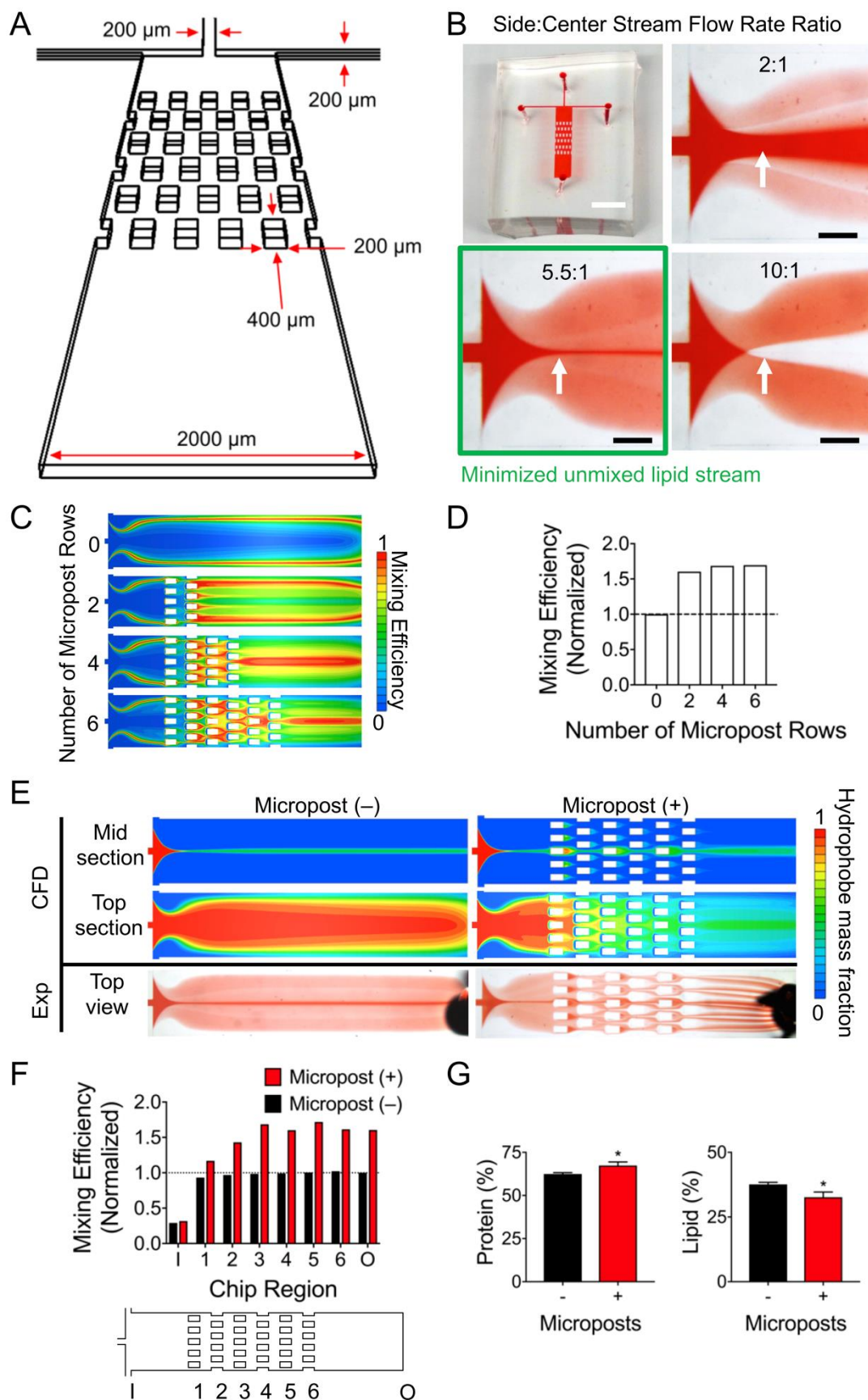


Figure S2.2. Engineering the microvortex propagation mixer (μ VPM).

(A) Critical dimensions of the μ VPM. (B) Image of μ VPM (Scale bar is 4 mm) and the determination of critical flow rates to minimize the unmixed lipid stream (white arrow) through experimental flow studies with phenol red (Scale bar is 400 μ m). (C, D) CFD simulations of the mixing efficiency based on the number of microposts in the μ VPM. (E) CFD simulations and experimental (EXP) results comparing the same platform with 6 rows (+) and 0 rows (–) of microposts through the mixing of the precursors given by the hydrophobe mass fraction. (F) A comparison of the simulated mixing efficiency of precursors between the platform with 6 rows (+) and 0 rows (–) of microposts spanning from the inlets (I) to the outlet (O); values are normalized to the micropost (–) case. (G) Protein and lipid quantification of eHNPs made with (+) and without (–) the micropost array ($n = 6$). Plotted as mean \pm SEM where * is for $p < 0.05$.

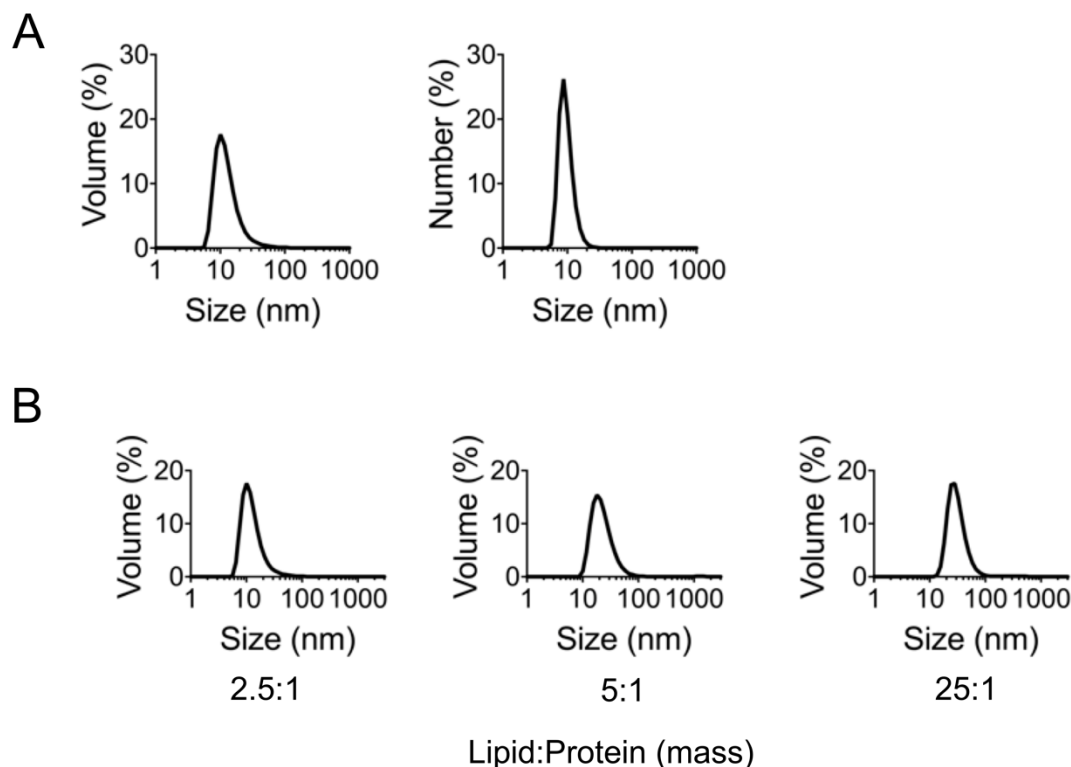


Figure S2.3. Size distributions of eHNP-A1

(A) Volume and number frequency distributions are given for the 2.5:1 (lipid:protein) mass ratio formulation for eHNP-A1. (B) Various formulations were examined to tune the size of the eHNPs to be around 10 nm for the volume (%) size frequency distribution for eHNP-A1.

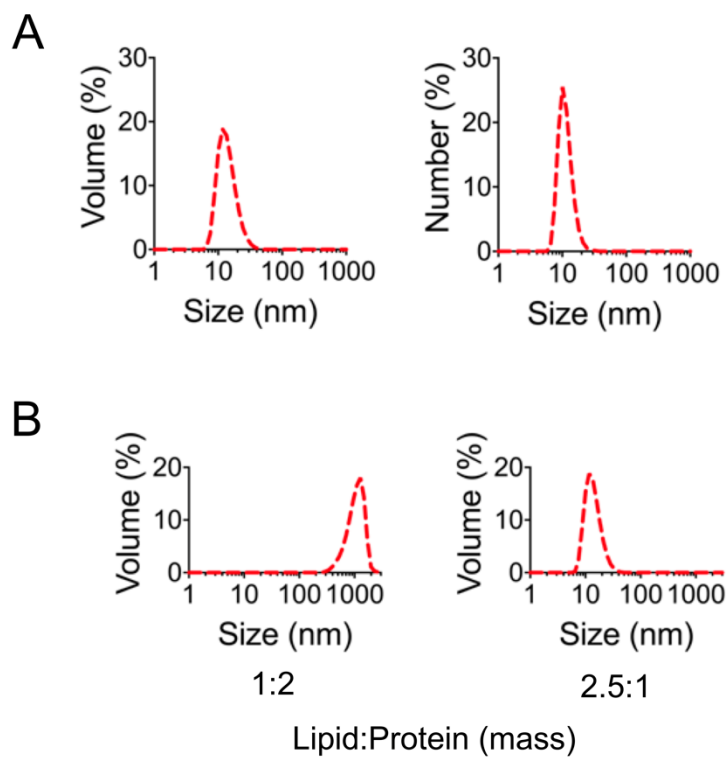


Figure S2.4. Size distributions of eHNP-r4F.

(A) Volume and number frequency distributions are given for the 2.5:1 (lipid:protein) mass ratio formulation for eHNP-r4F. (B) Various formulations were examined to tune the size of the eHNPs to be around 10 nm for the volume (%) size frequency distribution for eHNP-r4F.

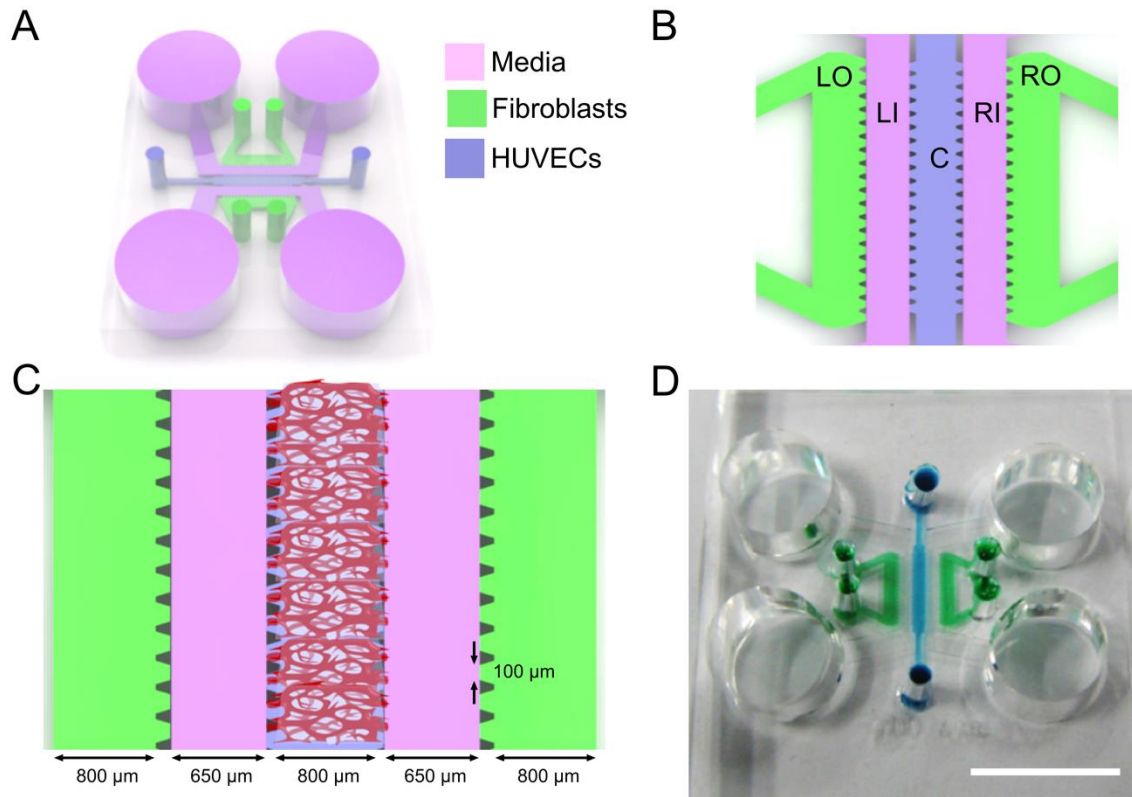


Figure S2.5. Microengineered vascular system components.

(A) Microengineered vascular system platform incorporates 5 channels; (B) the left outer (LO), left inner (LI), center (C), right inner (RI), and right outer (RO) channels. (C) Critical dimensions of the microengineered vascular system. (D) Photograph of microengineered vascular system (Scale bar is 1 cm).

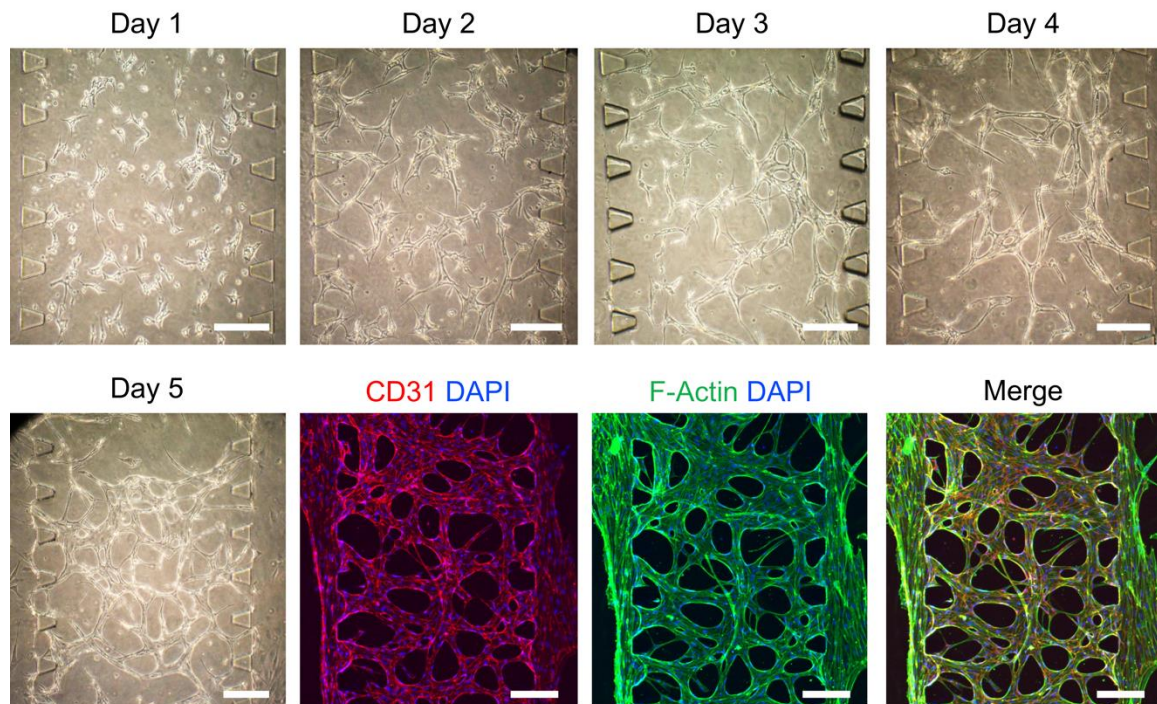


Figure S2.6. Microengineered vascular system timeline.

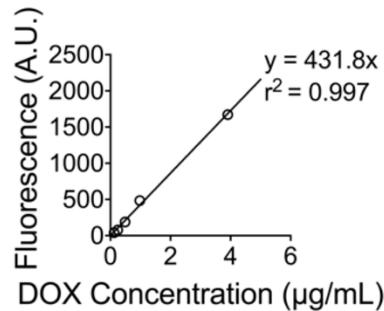
The HUVECs seeded into the C channel extend to the growth media filled LI and RI channels over the course of 5 days to fully form a perfusable microvascular network (scale bar is 150 μm).

A

	Measured Sample DOX Fluorescence (AU)	Sample DOX Concentration ($\mu\text{g/mL}$)	Sample Dilution*	Batch Volume (mL)	Encapsulated DOX per Batch (μg)	DOX used per Batch (μg)	Batch Yield (%)	Encapsulated DOX per mg of eHNP (μg)
eHNP-	1247.500	2.889	10.204	0.25	7.370	500	1.474	14.740
A1-	1223.500	2.833	10.204	0.25	7.228	500	1.446	14.457
DOX	748.000	1.732	16.667	0.25	7.218	500	1.444	14.436
eHNP-	163.000	0.377	10.204	0.74	2.850	500	0.570	5.701
r4F-	202.000	0.468	10.204	0.47	2.244	500	0.449	4.487
DOX	69.000	0.160	16.667	0.93	2.477	500	0.495	4.954

*Factor by which batch was diluted for sample to measure

B



C

Encapsulated DOX per batch (μg)
 $= (\text{Sample DOX Concentration}) \times (\text{Sample Dilution}) \times (\text{Batch Volume})$

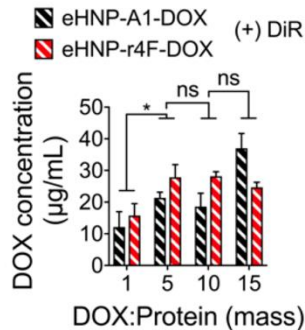
Batch Yield (%) $= \frac{(\text{Encapsulated DOX per Batch})}{(\text{DOX Precursor per Batch})} \times 100$

Encapsulated DOX per mg of eHNP (μg)
 $= (\text{Batch Yield}) \times 1000$

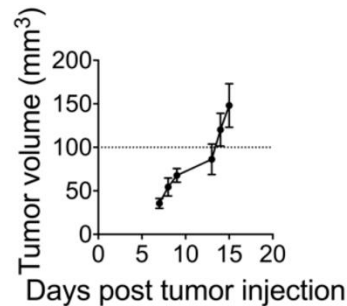
Figure S2.7. DOX loading measurements.

(A) Table of measurements for initial DOX loading measurements for Fig. 4. (B) Standard curve for DOX measurements. (C) Equations used to calculate DOX encapsulation amount and yield in eHNPs.

A



B



C

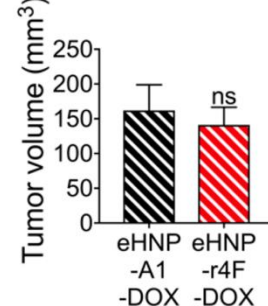


Figure S2.8. Preparation for in vivo experiment.

(A) DOX concentration in eHNPs with increasing DOX:Protein precursor mass ratios for in vivo experiments with the addition of DiR ($n = 3-6$). (B) Tumor volumes exceeded 100 mm^3 after growing for 15 days ($n = 12$). (C) Tumor volume difference prior to eHNP tail-vein injection between the experimental groups ($n = 7$). Plotted as mean \pm SEM where * is for $p < 0.05$.

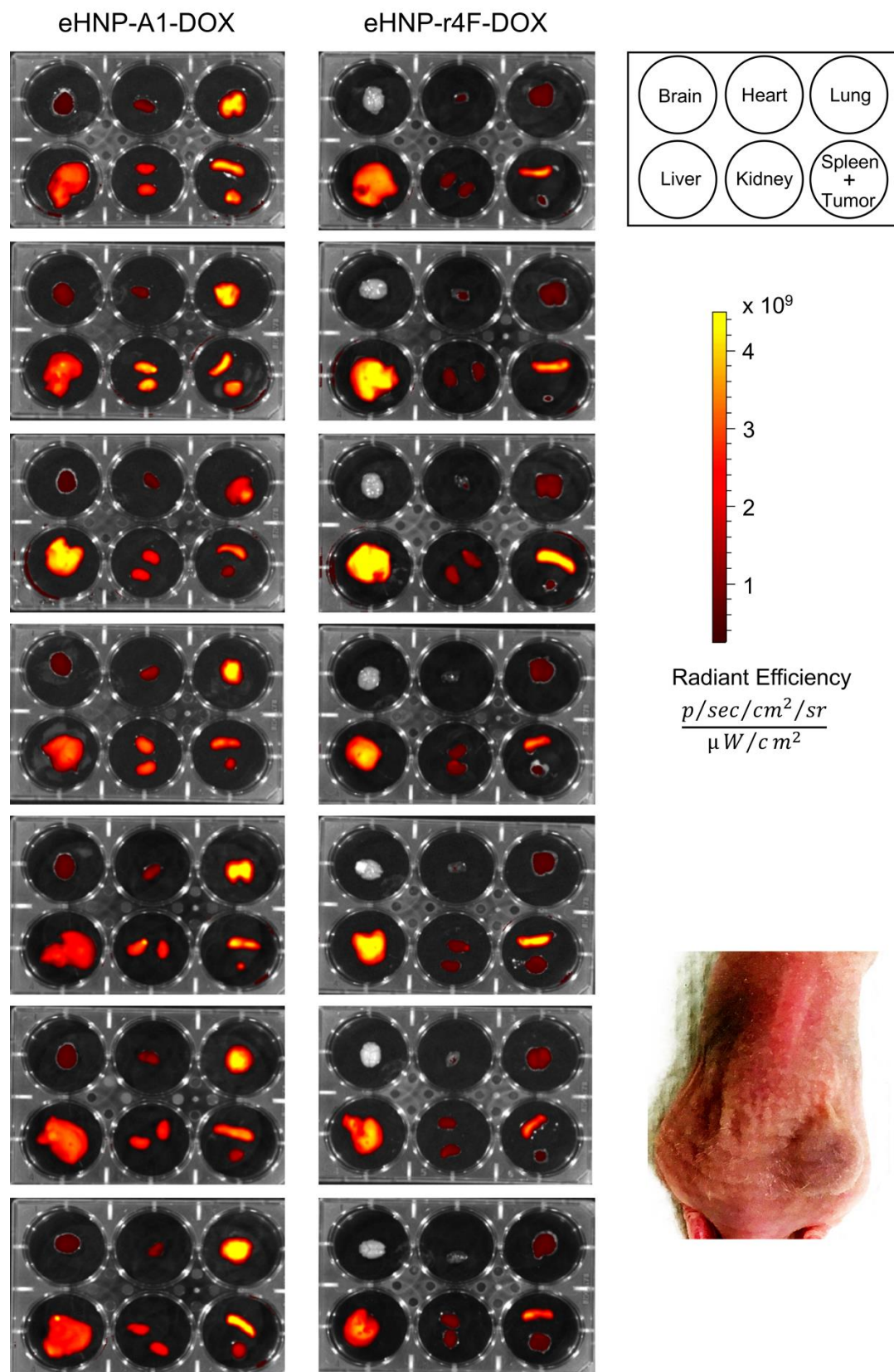


Figure S2.9. In vivo biodistribution measurements and setup.
 IVIS images 24 hs after tumor-bearing mice were treated with eHNP-A1-DOX or eHNP-r4F-DOX.

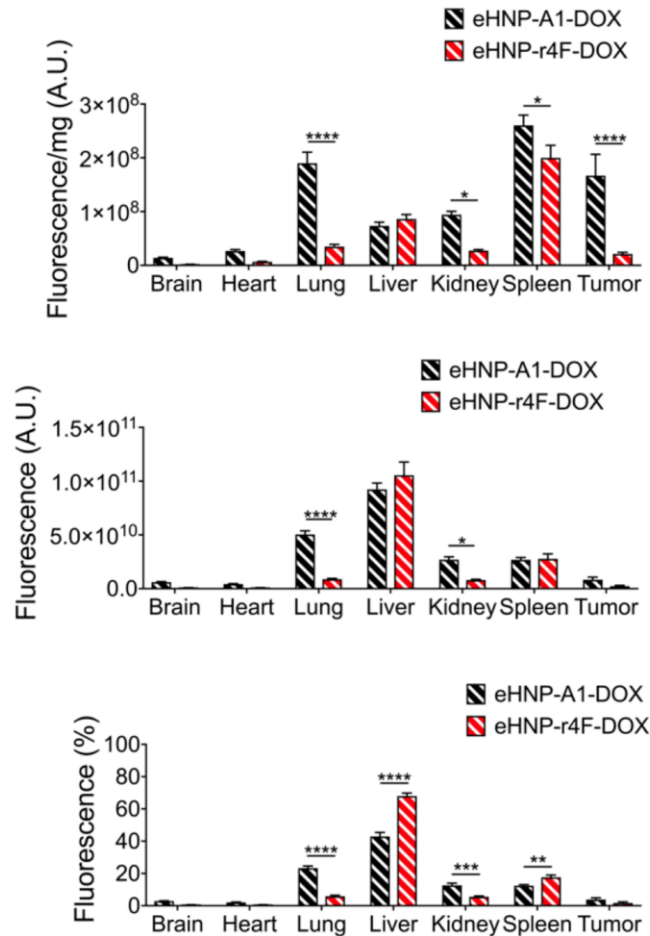


Figure S2.10. IVIS analysis for nude balb/c mice bearing HL-60 tumors.

Additional analysis of IVIS data (n = 7). Plotted as mean ± SEM where *, **, ***, and **** are for p < 0.05, 0.01, 0.001, and 0.0001 respectively.

Table S2.1. Molecular dynamics simulations for eHNP-r4F.

Molecular dynamics simulations for eHNP-r4F self-assembly based on increasing protein:lipid (mol) ratios and the resulting diameters of the particles that are formed (Scale bar is 5 nm).

Ratio (r4F:DMPC)	1:16	1:8	1:3
Size (nm)	5.02/8.62	7.54/7.37	7.29/6.81/7.01
View 1			
View 2			
View 3			

CHAPTER 3. A MICROPHYSIOLOGICAL SYSTEM FOR DETECTING AND MONITORING THE INFLAMED ENDOTHELIUM

3.1 ABSTRACT

The endothelial microenvironment is critical in maintaining the health and function of the intimal layer in vasculature. In the context of cardiovascular disease (CVD), the vascular endothelium is the layer of initiation for the progression of atherosclerosis. While laminar blood flows are known to maintain endothelial homeostasis, disturbed flow conditions including those the endothelium experiences in the carotid artery are responsible for determining the fate of CVD progression. We present a microfluidic device designed to monitor the endothelium on two fronts: the real-time monitoring of the endothelial permeability using integrated electrodes and the end-point characterization of the endothelium through immunostaining. Our key findings demonstrate endothelial monolayer permeability and adhesion protein expression change in response to oscillatory shear stress frequency. These changes were found to be significant at certain frequencies, suggesting that a frequency threshold is needed to elicit an endothelial response. Our device made possible the real-time monitoring of changes in the endothelial monolayer and its end-point inspection through a design previously absent from the literature. This system may serve as a reliable research platform to investigate the mechanisms of various inflammatory complications of endothelial disorders and screen their possible therapeutics in a mechanistic and high-throughput manner. The contents of this chapter were previously published in Scientific Reports [136].

3.2 INTRODUCTION

The vascular endothelium is a vessel-lining barrier that controls the transport of biologically active molecules and regulates inflammation, blood pressure and clotting, and immune cell trafficking. Endothelial homeostasis is critical for maintaining cardiovascular health against the onset of diseases that manifest from cardiovascular disease (CVD) [137]. Atherosclerosis is one such disease that stems from the chronic inflammation of the endothelium [3]. Studies examining the mechanotransduction of endothelial cells have linked endothelial inflammatory responses, including adhesion protein expression and nitric oxide production, to shear stress magnitude and direction [138-140]. Certain areas in the body, like the carotid sinus that has a unique expanding vasculature geometry, have localized disturbed flow acting back and forth against the vascular wall with shear stresses from $< 10\text{-}12 \text{ dyne/cm}^2$ in humans (Fig. 3.1A) [141, 142]. While endothelial homeostasis is maintained in laminar shear stress (LSS) conditions, the prolonged exposure of the endothelium to oscillatory shear stress (OSS) caused by disturbed flow leads to the chronic inflammatory response, adversely increasing the risk of atherosclerosis and CVD initiation [143-145]. Despite the understanding of the role of OSS-induced endothelial inflammation in several fatal diseases, challenges remain in sensing the inflamed endothelium under pathological blood flow (i.e. disturbed flow) and delivering sufficient therapeutic agents.

The implementation of atherosclerotic animal models has aided in the study of the disease progression and development of potential therapy options for the disease [146]. One such method to study the atherosclerotic pathology is to use the partial ligation surgery of the left carotid artery (LCA) in apoE^{-/-} mice [6] to apply disturbed flow and the resulting OSS to the endothelium and accelerate atherosclerotic plaque growth. While these findings have improved our understanding of OSS-derived pathology in CVD, further progress in this area is hampered by technical challenges of conducting mechanistic studies on targeted drug discovery and development in the human vasculature. Moreover,

extrapolation of animal data to human conditions has been frustratingly controversial, particularly for complex diseases afflicting dynamic microenvironments prevalent with mechanochemical stimuli such as blood flow and inflammatory cytokines [104]. Overcoming traditional in vitro models that predominantly rely on static culture of vascular endothelial cells, current advanced in vitro studies on endothelial mechanotransduction have taken the magnitude and direction of OSS into consideration to complement existing animal model research [138, 139, 143, 144, 147-149]. The frequencies typically associated to be characteristic of disease-causing OSS are based on measured physiological values in vivo; this value is about 5 Hz in mice, whereas in humans this level drops to approximately 1 Hz [7, 138, 145]. Despite sophisticated approaches to apply OSS in vitro, variations in endothelial cell responses to slight changes in the disturbed flow pattern may not be adequately reflected for studying certain mechanisms such as the dynamic interaction of the vascular endothelium with drugs in vivo [150, 151]. More importantly, little work has questioned whether the endothelial response is affected by the frequency of OSS, which may be key to influence expression of pro-inflammatory proteins like VCAM-1, ICAM-1, or IL-8 [152, 153]. Consequently, emerging technologies like biomimetic microfluidic platforms are being developed to address questions like these by implementing physiological and pathological conditions in a minimalist in vitro setting of OSS-induced vascular complications.

Microfluidic platforms, some of which are called organ-on-a-chip systems, provide an unprecedented ability to control the mechanical and chemical microenvironment in a spatial and temporal fashion, enabling the studies of dynamic cellular responses to a variety of mechanical and chemical stimuli [154]. The capabilities to measure cellular responses from dynamic environments typically found in physiological systems, as well as the potential for high-throughput applications, make microfluidic technology a suitable medium through which to study shear-dependent endothelial responses with

spatiotemporal manners and high precision. Microfluidic platforms have also grown to include screening tools to accelerate the development of therapeutics in physiological disease settings [11]. We present the design and implementation of a microfluidic transcellular monitor to dynamically examine the permeability and adhesion molecule expression of an endothelial monolayer to prolonged OSS-exposure of varying frequencies. Additionally, we report and address the challenges of widely used existing double-layered endothelialized microfluidic platforms; the endothelium near the channel wall fails to replicate physiologically relevant endothelial morphology and function in response to the application of shear, compromising the accuracy to investigate both the effect of mechanical and chemical cues on the endothelium and the translocation of nanoparticles across the endothelial barrier [73]. By imposing the accurate shear stress on primary human aortic endothelial cells (HAECs), as well as monitoring the endothelial permeability, our microfluidic transcellular monitor may provide a simple yet reliable platform to: (i) examine the underlying mechanisms by which vascular endothelial disorders occur and lead to complicated inflammatory pathologies, and (ii) efficiently test the efficacy of potential drug candidates targeting the dysfunctional endothelium in various mechanically (shear stress) and chemically (pro-inflammatory cytokines) stimulated pathophysiologically relevant conditions.

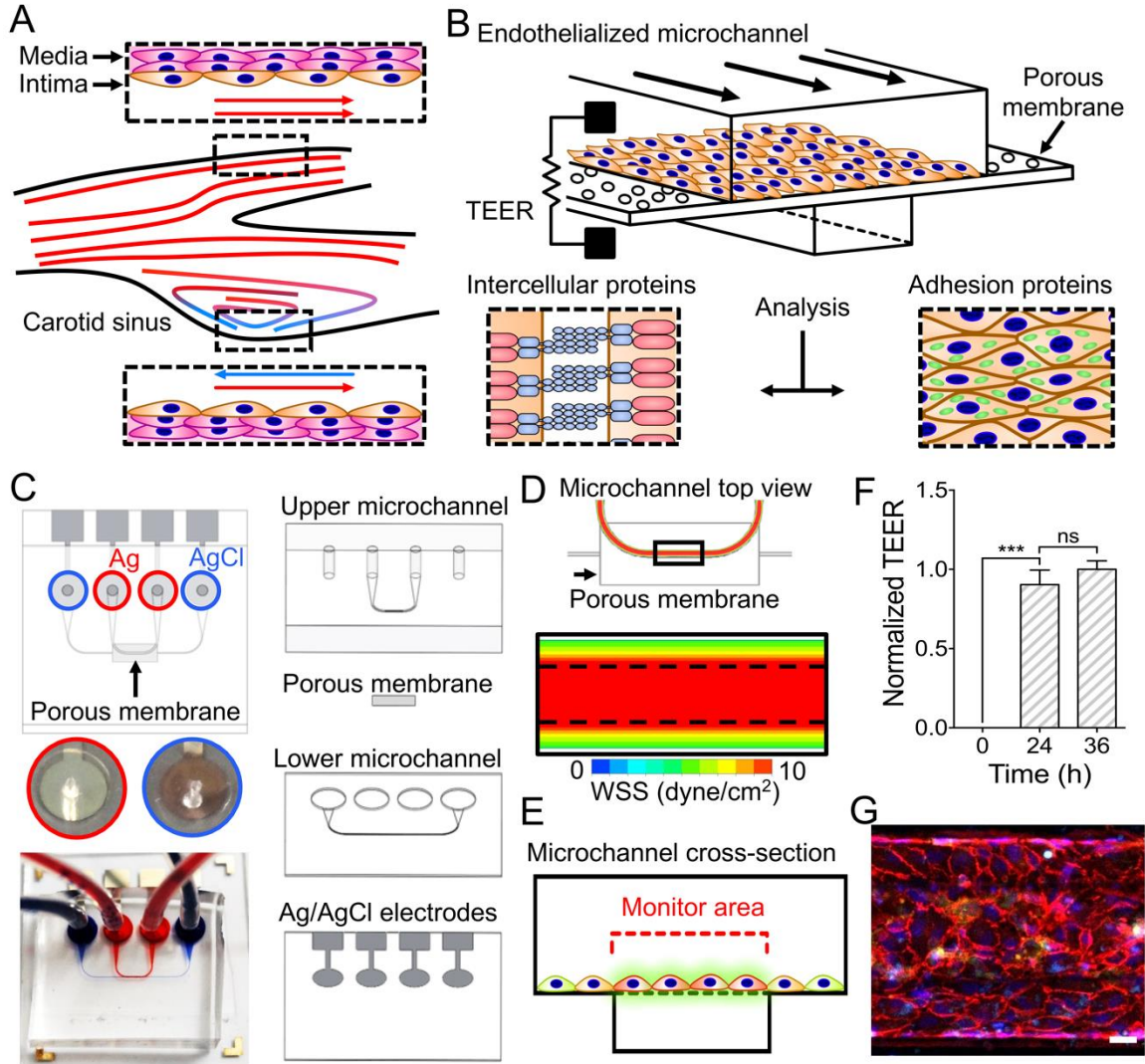


Figure 3.1. Monitoring of the endothelium for flow-based studies.

(A) Carotid bifurcation areas of LSS and OSS vary due to expanding sinus geometry. (B) A microfluidic transcellular monitor for probing endothelial responses to the flow microenvironment is capable of collecting both monolayer permeability data through TEER and monolayer images through a transparent porous membrane. (C) The device component overview highlighting the Ag/AgCl electrode integration directly into the platform to probe the monolayer growing on the porous membrane. (D) CFD simulations in the upper microchannel show the distribution of the wall shear stress (WSS) and the lower microchannel boundary (dotted line). (E) Cross-section schematic of upper and lower microchannels shows where the localization of ICAM should occur due to the calculated WSS distribution. (F) Monolayer maturity is determined through stabilization of TEER values ($N = 3$). Plotted as mean \pm SEM where * is for $p < 0.05$. (G) Confocal microscopy of an endothelial monolayer stained for adherens junctions (red) and ICAM (green) with DAPI counterstaining on a porous membrane with 8 μm pores. Scale bar is 25 μm .

3.3 RESULTS AND DISCUSSION

Microfluidic transcellular monitor design

The microfluidic transcellular monitor platform was designed to study the endothelial responses through electrical measurements and microscopy data that track the intercellular permeability and overall visual health of the monolayer in a multi-layer design (Fig. 3.1B). High-throughput and real-time monitoring of the endothelium was accomplished through an array of devices implementing the transendothelial electrical resistance (TEER) across the upper and lower microchannels using Ag/AgCl electrodes integrated on the device (Fig. 3.1C and Supplementary Fig. S3.1). This double-layered microfluidic platform with a high endothelial cell seeding density to allow for the uniform coverage of endothelial cells across the microchannel. To address the issue of the non-homogenous morphological and functional responses of endothelial cells due to their proximity to the sharp corner of the microchannel wall and better model the vascular endothelium, we performed computational fluid dynamics (CFD) analyses to find that the endothelial monolayer would only experience the greatest directional changes in response to flow within the middle 50% of the upper microchannel width (Fig. 3.1D). We validated these CFD simulation results using human umbilical vein endothelial cells (HUVECs), a widely used endothelial cell type in vitro, cultured in the upper microchannel geometry on a glass substrate to show nearly a 30% decrease in mean cell area for cells growing in the middle of the microchannel under flow, the absence of which resulted in an insignificant difference in the mean cell area between the cells growing in the two regions (Supplementary Fig. S3.2). Taking into account both the TEER dependency on the overlapping area of the upper and lower microchannels and the CFD simulation results, the upper microchannel was designed to have twice the width as the lower microchannel (200 μm and 100 μm , respectively) so that we could monitor an area that would only include the middle 50% region of the upper microchannel (Fig. 3.1E). With this microchannel configuration, we were able to efficiently inspect the HAEC monolayer growth and maturation using TEER, the leveling-off of which identified the monolayer

maturity with high reproducibility (Fig. 3.1F). Visual inspection of the HAEC monolayer through confocal microscopy was used in conjunction with TEER to gain a more representative understanding over how the endothelial monolayer responded to our flow-based stimuli (Fig. 3.1G).

Tailored platform more suitable for endothelial response monitoring

Using this new design that can accurately impose both the specific quantity and direction of shear stress on the endothelium cultured in the middle microchannel, we then investigated whether our microfluidic transcellular monitor was capable of accurately reconstituting pathophysiological conditions caused by shear stress profiles. We first cultured HAECs to form a monolayer and get exposed to LSS of $+10 \text{ dyne/cm}^2$ to investigate whether or not there is locally distinct expression of EC proteins in the center region (defined as the middle 50% region) of the upper microchannel (Fig. 3.2A). Comparing the center region to the remaining area of the upper microchannel (defined as the edge region) yielded a non-significant difference in the β -catenin (Fig. 4.2B) and ICAM intensity (Fig. 3.2C). We then examined this effect with an HAEC monolayer exposed to OSS of $+10$ and -9 dyne/cm^2 at 1 Hz (Fig. 3.2D). The comparison of the center region to the edge region yielded a non-significant difference in β -catenin intensity (Fig. 3.2E). However, there was nearly double the ICAM intensity expressed in the center region compared to that in the edge region (Fig. 3.2F). Following the verification of our simulation results with the observation of ICAM localization to the center region of the microchannel, the confocal imaging area for comparisons across devices with varying shear stress conditions was then defined to only include the center region due to the verified non-negligible effects of the microchannel wall. In following the same design intent, the choice to make the lower microchannel half as wide as the upper microchannel was to minimize the effect of the wall on TEER measurements. This is especially important for the accurate

monitoring of the endothelial permeability in response to varying shear stress conditions, such as shear oscillation frequency, due to the direct influence the overlapping area of the upper and lower microchannels has on TEER measurements [75].

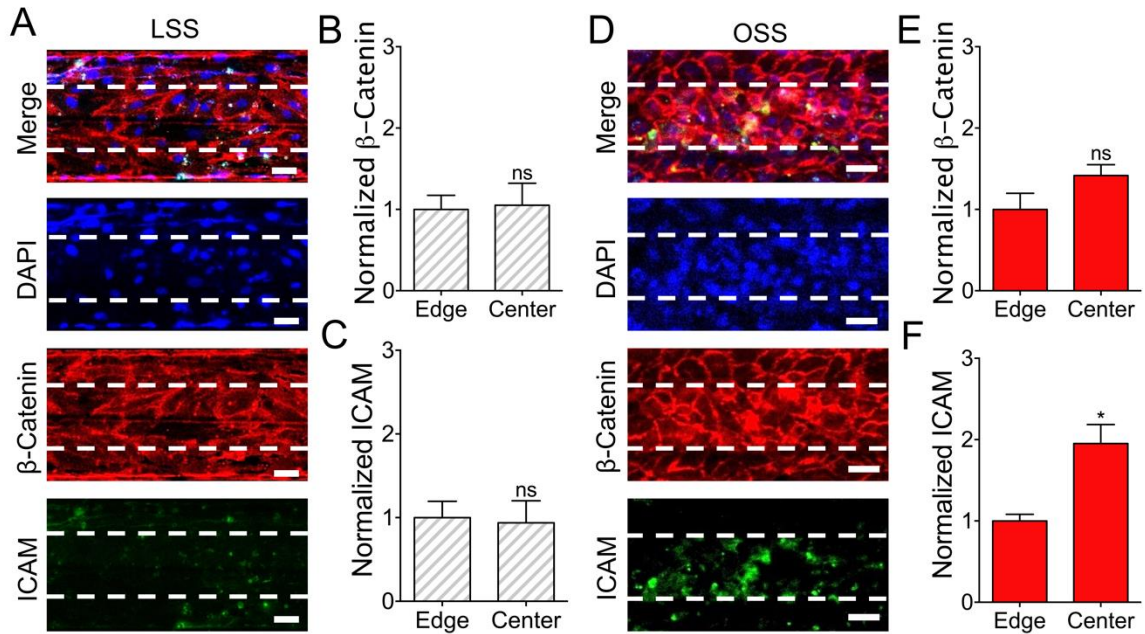


Figure 3.2. Microfluidic transcellular monitor design.

(A) Confocal microscopy images were taken through the underside of the porous membrane of an HAEC monolayer cultured in the upper microchannel under LSS at 10 dyne/cm² that were stained for β -catenin and ICAM (lower microchannel outlined with dotted white lines). Scale bar is 40 μ m. (B) β -catenin channel intensity measurements and (C) ICAM channel intensity measurements for the LSS case comparing the center and edge regions normalized to the edge region (N = 3). (D) Confocal microscopy images were taken through the underside of the porous membrane of an HAEC monolayer cultured in the upper microchannel under OSS at 1 Hz that were stained for β -catenin and ICAM (lower microchannel outlined with dotted white lines). Scale bar is 40 μ m. (E) β -catenin channel intensity measurements and (F) ICAM channel intensity measurements for the OSS case comparing the center and edge regions normalized to the edge region (N = 3). Plotted as mean \pm SEM where * is for $p < 0.05$.

Endothelial response is dependent on the OSS frequency.

The carotid artery is a region of interest in CVD research due to its unique geometry to produce locally recirculating or disturbed flows. The shear stresses in these regions average to about 10 dyne/cm², which is a commonly used shear stress value with HAECs under laminar flow in vitro [141, 142, 155, 156]. Shear stresses of +10 and +10/-9 dyne/cm² were used for the LSS and OSS conditions respectively to minimize variations in the flow conditions to be in OSS frequency while still allowing the refreshment of media

in the devices. The average shear stress magnitude across the microchannel width between the OSS and LSS cases, +1 and + 10 dyne/cm² respectively, were compared through CFD-calculated WSS distributions, β -catenin intensity measurements, and ICAM intensity measurements in the center channel region (Fig. 3.3A and B). The HAEC monolayers matured in 24 hours under LSS of +10 dyne/cm² (Fig. 3.1F), after which the various shear conditions were imposed for 12 hours (Supplementary Fig. S3.3). Between the +1 and +10 dyne/cm² cases under LSS, the differences in TEER, β -catenin intensities, and ICAM intensities were insignificant (Fig. 3.3C-E).

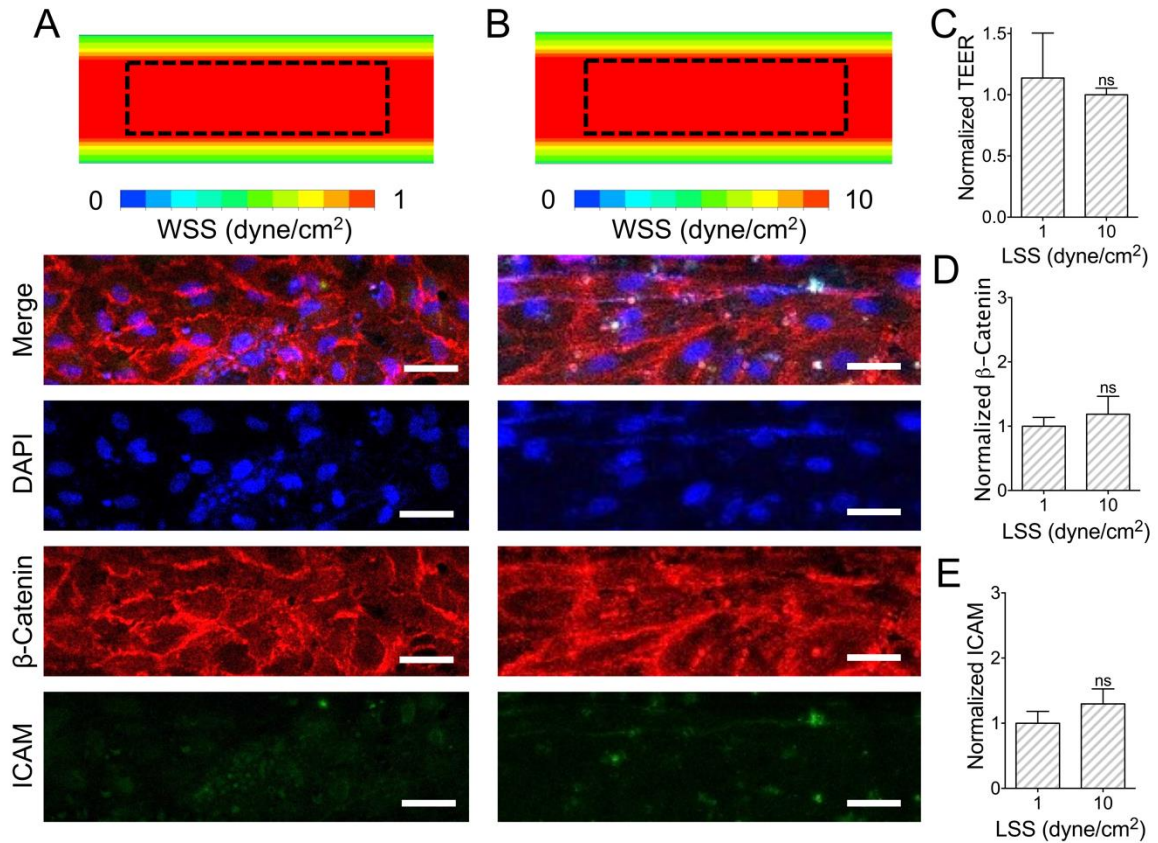


Figure 3.3. Comparing LSS cases for +1 and +10 dyne/cm².

(A) Upper microchannel WSS distribution and confocal microscopy of an HAEC monolayer cultured under +1 dyne/cm² and (B) + 10 dyne/cm² as viewed through the underside of the porous membrane. Confocal images used for comparison were taken from a region in the center of the upper microchannel (outlined). Scale bar is 40 μ m. (C) Normalized TEER of HAEC monolayer cultured under +1 or +10 dyne/cm². (D) β -catenin channel intensity measurements and (E) ICAM channel intensity measurements for the LSS cases comparing +1 and +10 dyne/cm² normalized to 1 dyne/cm² case (N = 3). Plotted as mean \pm SEM where * is for $p < 0.05$.

The HAEC monolayers were cultured under 0 X (LSS), 0.1 X (OSS), and 1 X (OSS) of the 1 Hz OSS frequency typically used in vitro to approximate the average resting heart rate of an individual [138]. The immunostaining comparisons showed disruptions in the endothelial monolayer and increased ICAM expression for 1 Hz case (Fig. 3.4A and B). Measuring the ICAM and β -catenin channel intensities revealed that while there was no significant difference in β -catenin expression, the 1 Hz case had a significantly higher expression of ICAM (Fig. 3.4C and D). Monitoring of the endothelial permeability revealed that the TEER significantly decreased for the HAEC monolayers exposed to OSS of 1 Hz compared to monolayers exposed to OSS of 0.1 Hz (Fig. 3.4E). TEER measurements with iMAECs instead of HAECs also showed the TEER to drop significantly after passing a certain frequency (Supplementary Fig. S3.4).

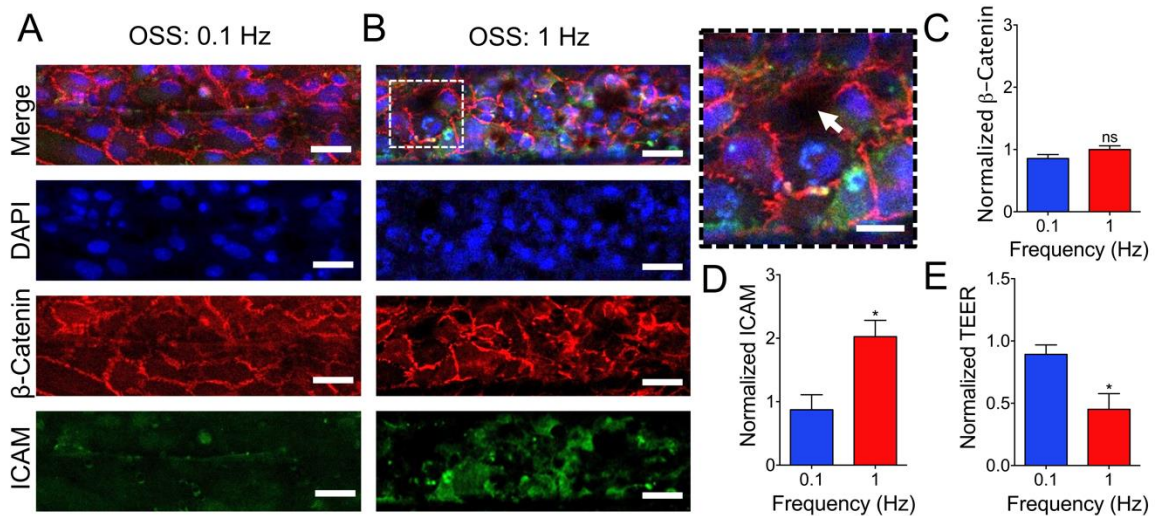


Figure 3.4. Monitoring of endothelial frequency response.

(A) Top view confocal images of HAEC monolayer in the center region cultured under 0.1 Hz. (B) Top view confocal images of HAEC monolayer in the center region cultured under 1 Hz with disrupted endothelial junction (white arrow). Scale bar is 40 μ m and 20 μ m for enlarged image. (C) β -catenin intensity channel measurements for the OSS cases comparing 0.1 and 1 Hz normalized to 10 dyne/cm² case (N = 3). (D) ICAM intensity channel measurements for the OSS cases comparing 0.1 and 1 Hz normalized to 10 dyne/cm² LSS case (N = 3). (E) Normalized TEER of HAEC monolayer after 36 hrs of culture under 12 hrs of 0.1 or 1 Hz normalized to the 10 dyne/cm² LSS case. Plotted as mean \pm SEM where * is for $p < 0.05$.

3.4 CONCLUSION

The design of the microfluidic transcellular monitor was based on the rationale that the endothelial cells cultured closer to the side walls of the microchannel with a rectangular cross section would exhibit different morphologies from experiencing different shear stress profiles, specifically in our case, less of the oscillatory fluid flow effects compared to endothelial cells cultured in the middle of the channel. Our results change the status quo of key design parameters to keep in mind when concerning microfluidic analyses of endothelial monolayers; there is now a cause for future double-layer microchannel platforms to more carefully take the microchannel configuration into consideration to minimize the influence of the microchannel wall on the experiment. With TEER measurements depending on the overlapping microchannel area, we took this design criteria into consideration by limiting the lower microchannel width to be half that of the upper microchannel [75]. The cultures of HUVECs under LSS and of HAECs under LSS and 1 Hz OSS were immunostained to validate our rationale and computational results with comparisons of mean cell area, β -catenin expression, and ICAM expression between the center (middle 50%) and edge regions (remaining 25% area on either side) of the upper microchannel.

Our validations of the insignificant differences between the net shears of +1 and +10 dyne/cm² determined that the differences observed between our cases were due to the different flow frequency cases and not in the shear magnitudes. The monitoring of the endothelium during different OSS frequencies showed consistent results across both human and mouse endothelial cells, indicating that the endothelial sensitivity to OSS frequency was not species-limited. Our results also indicate that there is a frequency threshold that must be reached in order to stimulate endothelial inflammation with OSS, suggesting that there may be a range of frequencies over which endothelial cells will respond in a pro-inflammatory manner. While it is still unclear as to what the breadth of

this endothelial pro-inflammatory frequency range includes, comparisons of our results with prior studies on the risks of resting heart rate and CVD suggest that higher resting heart rates, and thus potentially higher OSS frequencies, have higher risks of experiencing a CVD-related episode [157, 158].

Our findings suggest that the inflammatory response of endothelial cells to OSS may be triggered by meeting a minimum frequency requirement. We demonstrated the design rationale behind our platform to take advantage of its capabilities to detect changes in both monolayer permeability and inflammatory marker expression in response to changes in OSS frequency. Future work to consider with this device would be to explore the extent of the frequency dependency by pairing the device with a more sophisticated fluid flow controller to impose high frequency flows, as well as to screen extensive libraries of nanomedicines and therapeutics targeting the endothelium to rapidly identify and catalogue endothelial responses [159]. The translation of these results across humans and mice may also be further pursued to help bridge the gap between human and animal models.

3.5 METHODS

Materials and chemicals

The reagent (3-aminopropyl)triethoxysilane (APTES) was purchased from Sigma-Aldrich Co. LLC. (St. Louis, MO). Polydimethylsiloxane (PDMS) was purchased as Sylgard 184 from Dow Corning (Midland, MI). The photoresist SU-8 and its developer were purchased from MicroChem Corp (Westborough, MA). HAECs and HUVECs were purchased from ATCC (Manassas, VA) and ScienCell Research Laboratories (Carlsbad, CA) respectively. The iMAECs were generously donated from the lab of Dr. Hanjoong Jo.

Microfluidic transcellular monitor design and fabrication

The microfluidic transcellular monitor was first conceptualized using the CAD software SolidWorks from Dassault Systemes SolidWorks Corp. (Paris, France), after which we conducted computational flow studies using the Fluent solver (ANSYS, Inc. Concord, MA). The dimensions of the upper and lower microchannels were 200 μm x 100 μm and 100 μm x 50 μm respectively (width x height). All simulations were solved for a single fluid with the Newtonian properties of water and using a structured mesh for the device microchannel [127, 160]. The boundary condition at the device inlet was set to 20 $\mu\text{L}/\text{min}$ and 2 $\mu\text{L}/\text{min}$ for the average +10 and +1 dyne/cm^2 conditions respectively to examine the distribution of the WSS in the cell-culture region of the upper microchannel. Fabrication of the device started with Ag electrodes patterned onto glass slides using metal evaporation deposition [161]. The thin PDMS sheet for the lower microchannel was made by spin coating PDMS to 250 μm in height onto an SU-8 patterned silicon wafer. The upper microchannel was constructed using standard soft lithography to a patterned wafer. An 8 μm pore polycarbonate membrane (Sterlitech Corp, Kent, WA) was then treated in a 5% APTES solution at 80°C for device assembly prior to device housing [162]. The lower microchannel AgCl electrodes were produced using household bleach to soak the Ag electrodes for 1 hour at room temperature [163]. The fabricated device was housed in a polystyrene box for microfluidic cell culture using syringe pumps (Supplementary Fig. S3.1).

Microfluidic endothelial cell culture preparation

Prior to seeding cells into devices, HAECs, iMAECs, and HUVECs were cultured in EGM-2 (Lonza, Basel, Switzerland) and complete endothelial growth medium (DMEM with 10% FBS, 1% endothelial cell growth supplement (ECGS), and 1% penicillin and streptomycin) respectively. Cell media was replaced every 3 days, with cultures being split

at confluence. The device, housing, and tubing were sterilized with 70% ethanol and washed with DI-water and PBS (1X, pH 7.4) prior to coating the microchannels with fibronectin (50 µg/mL) for 2 hs at 37°C. Cells were seeded into the devices at a concentration of approximately 1×10^7 cells/mL. Following a 1 h incubation at 37°C, devices were connected to Harvard Apparatus (Holliston, MA) PhD Ultra syringe pumps and exposed to 20 µL/min (HAECs and HUVECs) or 14 µL/min (iMAECs) while incubating at 37°C. To study the effects of OSS frequency, monolayers were cultured for 24 hours and 48 hours for HAECs and iMAECs respectively before applying the different shear frequencies (Supplementary Fig. S3.3 and S3.4).

TEER measurements

TEER measurements were taken every 12-24 hrs at 37°C using the EVOM2 volt-ohmmeter (World Precision Instruments, Sarasota, FL). A potential source of error is from noise in the TEER measurements, which was reduced by averaging multiple readings for each device at every time point, and by taking all measurements at the same temperature inside of a cell culture incubator, as TEER can also be affected by temperature fluctuations. Measurements were normalized to the mature monolayer value in each device relative to when there were no cells in the device (0 h).

Immunostaining of endothelial cells

Cell fixation was done using 4% paraformaldehyde (PFA) in PBS before permeabilizing in 0.1% triton. Samples were blocked with 1% bovine serum albumin (BSA) in PBS. Antibody incubation was with anti-β-catenin antibody (ab32572, Abcam, Cambridge, UK) and anti-ICAM-1 antibody (322713, BioLegend, San Diego, CA) at 4°C overnight followed by Cy5 conjugated secondary antibody (ab150075, Abcam). Confocal

microscopy imaging of the stained devices was done with a Zeiss LSM 700 microscope (Zeiss, Oberkochen, Germany).

Image analysis

Confocal images of each device were analyzed using the regions of interest (ROI) manager in ImageJ. For comparisons of the center and edge regions of the microchannel, the microchannel was parsed into 8 sections; the center 4 sections were used to define the center ROI, and the outer 4 sections were used to define the edge ROI. For the frequency dependency analyses, only the center ROI of the microchannels was compared. The individual channels for ICAM and β -catenin were used for ROI comparisons. HUVEC areas were calculated using ImageJ ROI manager, where cells were sorted into center and edge regions based on the area the cell occupied the most.

Statistical analysis

Statistical analyses were run in Prism 6 (GraphPad Software Inc, La Jolla, CA) and significance was defined as $p < 0.05$ (*). ANOVA tests were used to compare the TEER and immunostaining results of 0X, 0.1X, and 1X frequency cases, and t-tests were used for comparisons between the LSS groups and center/edge image analyses.

3.6 SUPPLEMENTARY INFORMATION

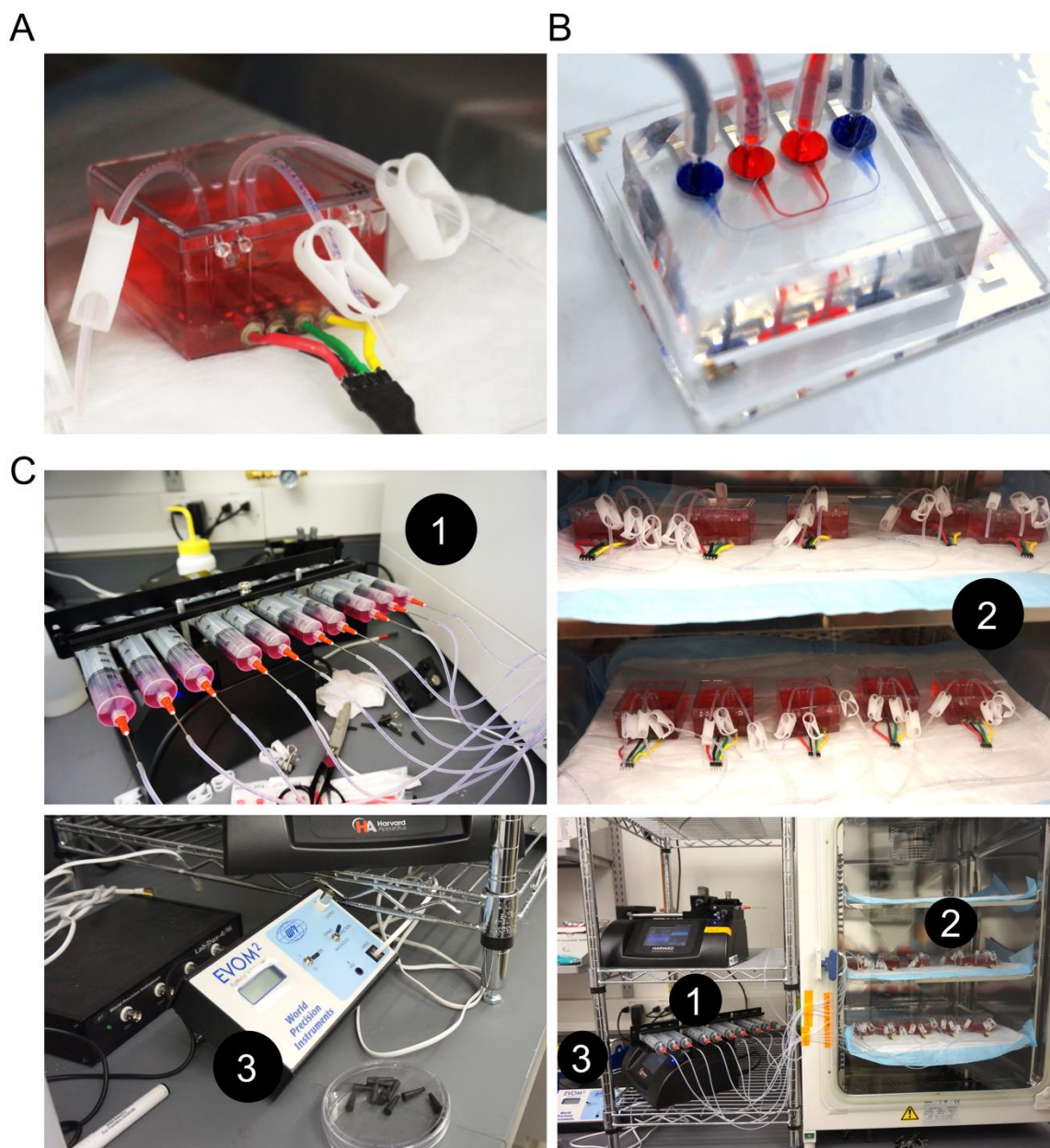


Figure S3.1. Microfluidic transcellular monitor setup.

(A) The device during cell culture is enclosed in a polystyrene box with a wire connector interface to communicate with an EVOM2 volt-ohmmeter. (B) Image of device highlighting the upper microchannel (red) and lower microchannel (blue) which are separated by a transparent porous membrane. (C) High throughput experimental setup using multi-rack syringe pumps (1) to apply flow to incubated devices (2) that are monitored with the EVOM2 volt-ohmmeter (3).

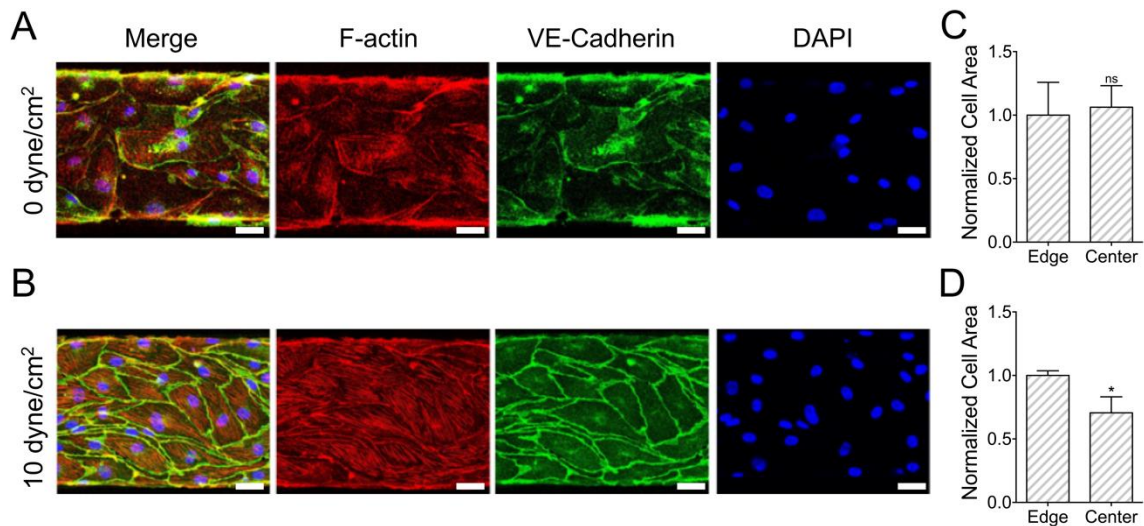


Figure S3.2. The effect of the microchannel wall.

(A) Confocal images of HUVECs that were cultured in a single layer device with the upper microchannel geometry and a glass bottom substrate under 0 dyne/cm² and (B) +10 dyne/cm² LSS conditions. Scale bar is 25 μm. (C) The mean area was compared between cells growing near the edge of the channel and cells growing in the center of the channel for 0 dyne/cm² and (D) +10 dyne/cm² normalized to the mean cell area at the edge of the channel (N = 7-8). Plotted as mean ± SEM where * is for p < 0.05.

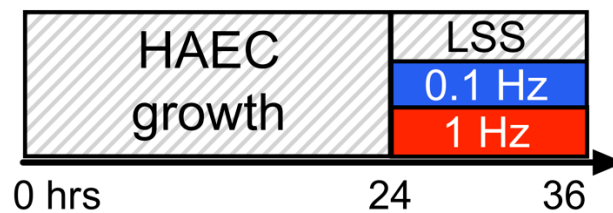


Figure S3.3. OSS culture timeline for HAECs.

Timeline of monolayer growth in devices for HAECs to compare OSS frequency effects on a mature endothelial monolayer.

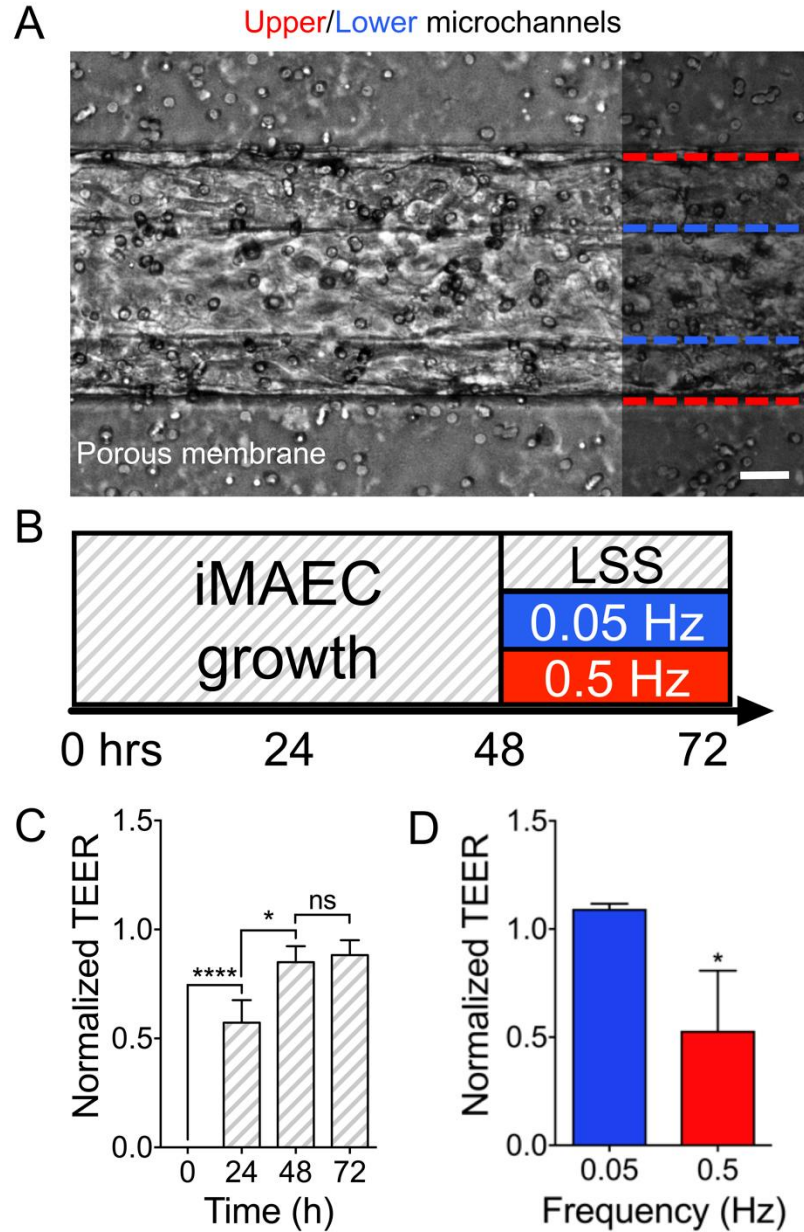


Figure S3.4. OSS frequency response in iMAECs.

(A) Contrast image of iMAEC monolayer growing in device with upper (red) and lower (blue) microchannels highlighted. Scale bar is 40 μm . (B) Timeline of monolayer growth in devices for iMAECs to compare OSS frequency effects on a mature endothelial monolayer. (C) Normalized TEER tracking of iMAEC monolayer growth over 72 hrs (N = 4-13). (D) Normalized TEER of iMAEC monolayer after 72 hrs of culture under 24 hrs of 0.05 or 0.5 Hz normalized to the LSS case (N = 3-5). Plotted as mean \pm SEM where * is for $p < 0.05$.

CHAPTER 4. PROBING THE IMPACT OF OSCILLATORY SHEAR STRESS ON HDL-MIMETIC NANOPARTICLE INTERACTIONS WITH THE ENDOTHELIUM

4.1 ABSTRACT

Translational issues continue to persist in the development of therapies from the benchtop to the clinic. In the context of cardiovascular disease (CVD), high-density lipoprotein (HDL) therapies have shown promising results in benchtop experiments. However, translating these results to the clinic have been mixed at best, causing confusion in identifying the role of HDLs in CVD progression and prevention. In this study we implement microfluidic technologies to synthesize and screen HDL-mimetic nanoparticles engineered to visualize cellular uptake and isolate any protein-based interactions to be with apolipoprotein-A1 (apoA1), the most abundant apolipoprotein in the HDL proteome. The resulting experiments identified that when above a threshold concentration, our HDL-mimetic nanoparticles could induce a pro-inflammatory response from human aortic endothelial cells cultured under oscillatory shear stress (OSS). However, the same response was not observed when the culture conditions used LSS instead of OSS, and when the apoA1 receptor scavenger receptor class B type 1 (SR-B1) was inhibited. This would indicate that a pro-inflammatory response from the endothelial cells is dependent on both the OSS condition and the interaction between SR-B1 and apoA1.

4.2 INTRODUCTION

Natural high-density lipoproteins (HDLs) are 10 nm transporters of fats and nucleic acids that have been studied for cardiovascular disease (CVD) therapies due to their innate properties that can reduce endothelial inflammation [66, 164]. Identified as the primary functional component for HDL, apolipoprotein-A1 (apoA1) is the scaffolding

protein of HDL with the purpose of binding lipids and stabilizing the endogenous nanoparticle [165, 166]. ApoA1 is also accredited for HDL's receptor-specific interactions, the most common of which is with scavenger receptor class B type 1 (SR-B1); it is the primary mode of HDL uptake into a cell and triggering pathways for reverse cholesterol transport (RCT) and endothelial nitric oxide (NO) production [93, 167, 168]. With these functional properties of HDL in mind, the HDL hypothesis stipulates that increasing the concentration of HDL in CVD patients will lower CVD-related incidents; however, mixed results in HDL-based therapies suggest an underlying mechanism that can influence HDL functionality that has yet to be fully elucidated [27]. To tackle such complicated and sensitive mechanistic questions, it becomes necessary to have control over the complex composition of HDL; studies focusing on HDL-therapeutics commonly simplify the diverse HDL-proteome and lipidome into the combination of a single type of phosphocholine (PC) lipid with apoA1 in order to isolate any protein-based interactions with the particle [19, 34, 37]. Through the simplification of its core components, reconstituted HDLs (rHDLs) may be engineered for specific diagnostic or therapeutic applications. The design and realization of these engineered HDL-mimetic nanoparticles (eHNPs) may be accomplished and accelerated with the application of microfluidic technologies [66].

Microfluidic technologies have enabled the development of various tools with which to produce, characterize, and screen nanoparticles like HDL [11]. Microfluidic platforms for the single-step synthesis of NPs enable precise control over the mixing patterns that encourage the monodisperse self-assembly of NPs [54, 60, 63]. The implementation of these microfluidic NP synthesis enables the recovery of a more monodisperse batch of NPs with little batch-to-batch variation. Microfluidic platforms may also be designed to probe the interactions of nanoparticles in biological settings that more accurately mimic physiological conditions when compared to static *in vitro* culture systems [73]. These microphysiological systems, or organ-on-a-chip systems, are designed to

culture tissue-specific cells under their respective dynamic culture conditions through the use of shear stress, 3D culture environments, or other forms of mechanochemical or electrical stimuli [104]. In the case of probing endothelial responses to physiologically relevant pathological conditions for CVD, it is critical to consider the magnitude, directionality, and frequency of flow [6, 136, 138, 143]. The flow condition credited for the initiation of CVD is known as disturbed flow, which involves the flow profile having a bi-directional pattern over the endothelium at a frequency of about 1 Hz in humans [136]. This oscillatory shear stress (OSS) enhances the inflammatory response of the endothelium, triggering its enhanced permeabilization and its upregulation of adhesion molecules like intercellular adhesion molecule-1 (ICAM-1) and vascular adhesion molecule-1 (VCAM-1) relative to when the endothelium is cultured under laminar shear stress (LSS) conditions [136, 138, 139]. These responses may be characterized through immunostaining of the monolayer and the transendothelial electrical resistance (TEER), the real-time resistance measurement across the endothelial monolayer that correlates with the permeability of the monolayer [73, 136]. However, due to the technical challenges that need to be overcome in order to implement microfluidic platforms for both NP research and biomimetic platforms, there is a lack in the number of studies that utilize microfluidics to synthesize and screen NPs despite the many advantages microfluidics may provide.

In order to uncover portions of the complex interactions between HDL and the inflamed endothelium, it is necessary to monitor the response of the endothelium in a dynamic microenvironment with compositionally homogenous HDLs (Fig. 4.1A). With the purpose of isolating the interactions between HDL and the inflamed endothelium to be apoA1-dependent, we implemented our microvortex propagation mixer (μ VPM) to synthesize eHNPs for which we controlled the NP composition (Fig. 4.1B). We then probed the permeability and adhesion molecule expression levels of the endothelium to our eHNPs under both LSS and OSS conditions in a microfluidic transcellular monitor

(μ TM) to discover if there was a flow-dependent endothelial response to our apoA1-based eHNPs (Fig. 4.1C).

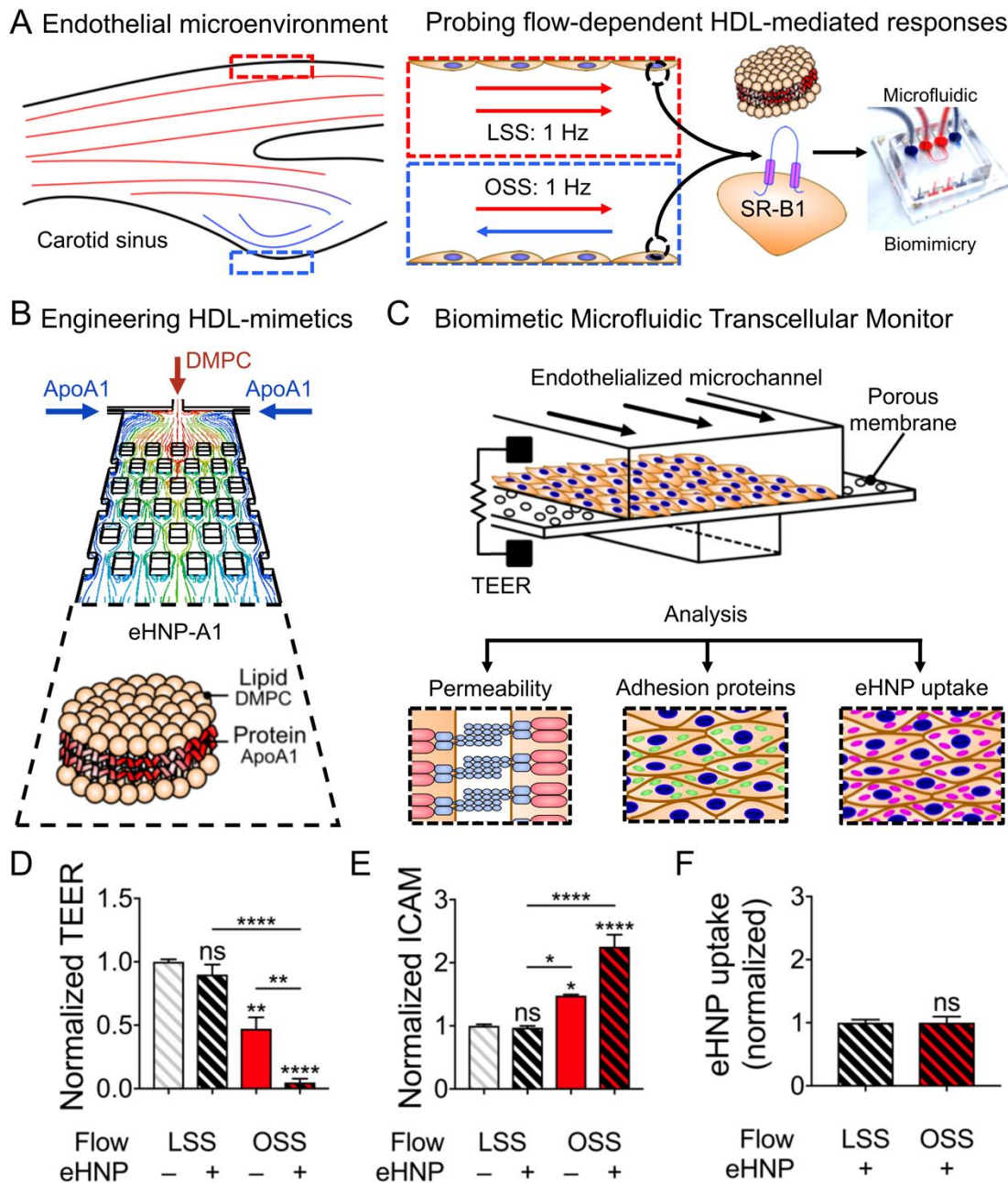


Figure 4.1. Detecting flow-dependent interactions of HDL with the endothelium.

(A) Oscillatory flow conditions relevant to CVD in humans is achieved using biomimetic microphysiological systems in order to study HDL interactions with the endothelium. (B) Engineered HDL-mimetic nanoparticles (eHNPs) with microfluidics enables control over composition. (C) The microfluidic transcellular monitor allows for both real-time and endpoint measurements of the monolayer through TEER and confocal analysis. (D) TEER, (E) ICAM, and (F) eHNP uptake LSS-

normalized measurements in response to LSS or OSS with eHNPs at a concentration of 25 $\mu\text{g/mL}$ (N = 3-4). *, **, and **** are for $p < 0.05$, 0.01 , and 0.0001 respectively.

4.3 RESULTS AND DISCUSSION

Endothelial cells respond to eHNPs depending on the oscillatory flow condition.

Upon conditioning with LSS, or the non-oscillating shear stress (0 Hz), endothelial cells (ECs) showed no detectable changes in monolayer permeability or ICAM expression when stimulated with eHNPs (Fig. 4.1D and E). However, ECs stimulated with both OSS at 1 Hz and eHNPs displayed a significantly different response to when ECs were stimulated with OSS at 1 Hz alone; the endothelial permeability and ICAM expression were both amplified in the presence of both OSS and eHNPs (Fig. 4.1D and E). Despite the significant differences in responses to eHNPs when under 0 or 1 Hz flows, there was no significant difference in the fluorescent signal of eHNPs in ECs (Fig. 4.1F). This would indicate that the rate of endothelial eHNP uptake was the same between 0 and 1 Hz stimulation conditions, and that such a rate is not influenced by the oscillatory condition of the shear stress. However, from these initial results we found that interactions between the endothelium and the eHNPs are modulated with the flow conditions with which the ECs are stimulated; eHNPs appear to stimulate a non- or pro-inflammatory response from ECs depending on stimulation with LSS or OSS flow. While it is not unheard of for natural HDLs to be dysfunctional under certain oxidative conditions [33], this finding connects the endothelial-HDL interactions with the endothelial flow condition. To gain a better understanding over the mechanisms of this response, it is imperative to identify other parameters that may change the ICAM expression and endothelial monolayer permeability. One such parameter is the eHNP concentration.

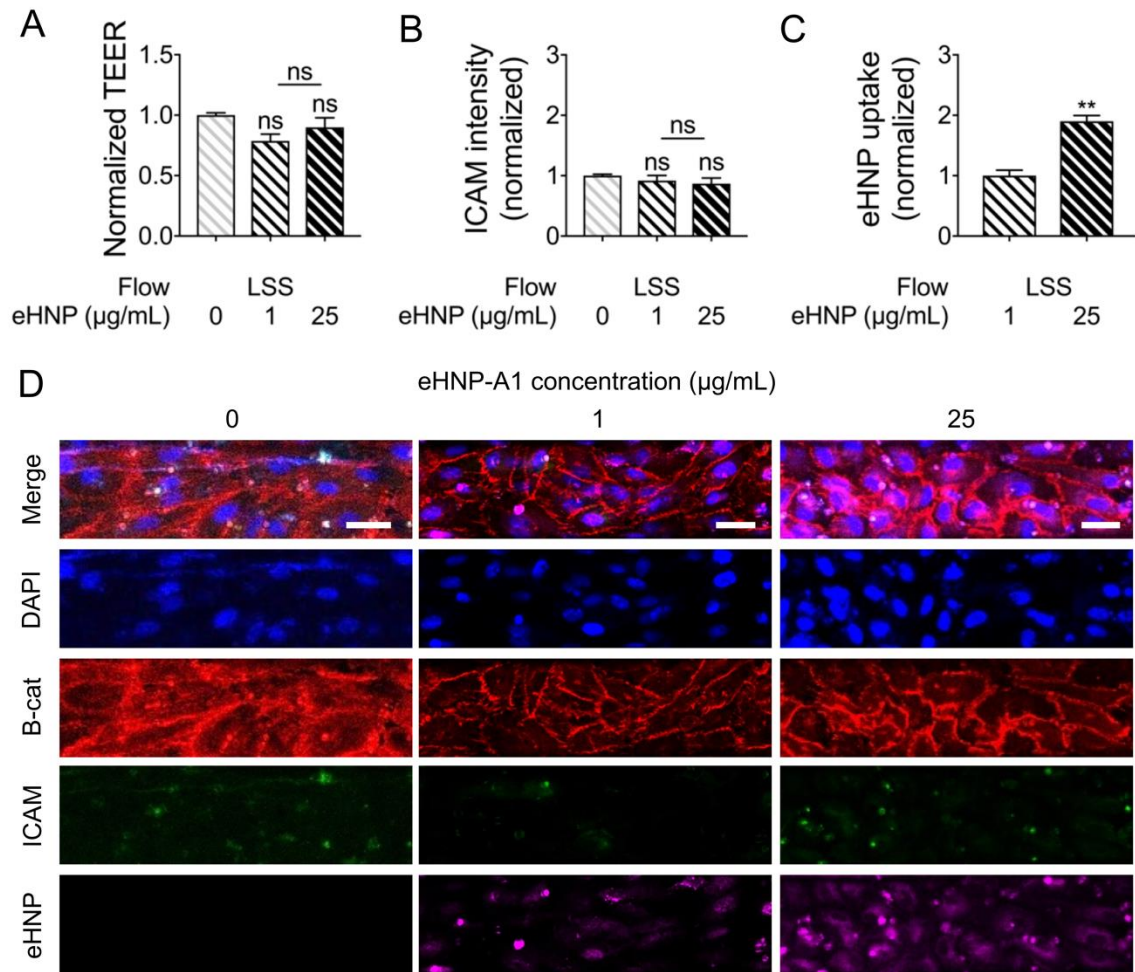


Figure 4.2. eHNP concentration dependent analysis with LSS.

(A) TEER, (B) ICAM, and (C) eHNP uptake LSS-normalized measurements (0 Hz & 0 µg/mL) under LSS conditions (N = 3-4). (D) Confocal images of the endothelium in response to varying eHNP concentrations (scale bar is 40 µm). ** is for $p < 0.01$.

The endothelial response to eHNPs is conditionally concentration-dependent.

When increasing the concentration of eHNPs stimulating ECs from 1 to 25 µg/mL under 0 Hz flow, there were no significant differences in either the TEER or ICAM intensity measurements (Fig. 4.2A and B). With the exception of a 2-fold increase in the fluorescent intensity measurements for eHNP uptake (Fig. 4.2C), the monolayer showed no significant differences in the fluorescent channels when increasing the eHNP concentration under 0 Hz flow (Fig. 4.2D). Upon changing the condition to a 1 Hz OSS flow however, varying the concentration of eHNPs from 1 and 25 µg/mL had significant impacts on both the TEER

and ICAM expression measurements (Fig. 4.3A and B). With the same 2-fold increase in eHNP uptake (Fig. 4.3C) as the 0 Hz flow case, confocal analysis of the endothelial monolayer shows a clear distinction in the 25 $\mu\text{g/mL}$ eHNP group from both the 0 and 1 $\mu\text{g/mL}$ groups under 1 Hz flow (Fig. 4.3D).

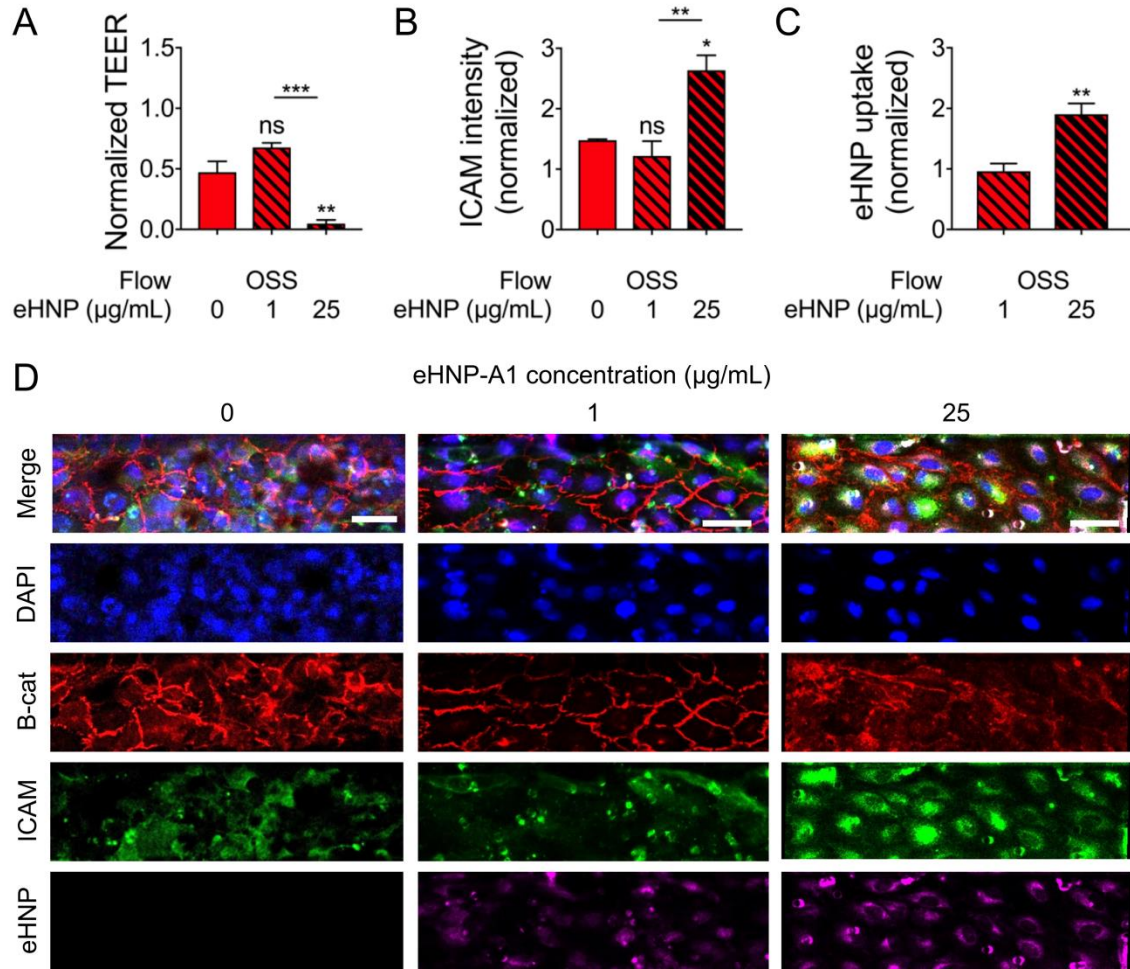


Figure 4.3. eHNP concentration dependent analysis with OSS.

(A) TEER, (B) ICAM, and (C) eHNP uptake LSS-normalized measurements (0 Hz and 0 $\mu\text{g/mL}$) under OSS conditions (N = 3-4). (D) Confocal images of the endothelium in response to varying eHNP concentrations (scale bar is 40 μm). *, **, and *** are for $p < 0.05$, 0.01, and 0.001 respectively.

This conditional dependency on eHNP concentration presents a threshold at which the concentration of eHNPs may trigger a pro-inflammatory phenotype depending on the oscillatory flow condition. However, it remains unclear if there is another threshold at which

there is an eHNP concentration that could be anti-inflammatory under OSS conditions. The rationale for such a stipulation stems from our previous study that presented the biphasic response of ECs to varying eHNP concentrations, for which a certain range would stimulate angiogenic sprouting while another range would inhibit angiogenic sprouting [107]. The significance of our finding is still impactful despite this possibility; the differences between 0 and 1 Hz flow cases with regards to the endothelial response to varying eHNP concentrations exemplifies a flow-dependent and concentration-dependent response that requires meeting multiple criteria: the oscillatory flow frequency [136], and the eHNP concentration. Determining the mode through which this flow- and concentration-dependent interaction between eHNPs and ECs is mediated necessitates exploring the role of SR-B1, the primary receptor for apoA1.

The amplified endothelial response to OSS and eHNPs is absent without SR-B1.

Should the primary interaction between our eHNPs and the ECs be mediated through apoA1, then the inhibition of its primary receptor, SR-B1, should temper the endothelial response to the eHNPs under 1 Hz OSS flow. The agent block lipid transport-1 (BLT-1) has been routinely used to block SR-B1 in studies involving cellular uptake of HDL and the induction of RCT [169, 170]. Inhibition of SR-B1 with BLT-1 in our μ TM platform resulted in the absence of the amplified effects of eHNP and 1 Hz OSS flow, as reflected in both the TEER and ICAM measurements (Fig. 4.4A and B). The uptake of eHNPs was halved with the endothelial treatment of BLT-1 for both 0 Hz LSS and 1 Hz OSS flow conditions (Fig. 4.4C). The non-significant differences in eHNP uptake between 0 and 1 Hz flows are consistent with the uptake of eHNPs when BLT-1 was not used (Fig. 4.1F), which showcases that the uptake of the eHNPs with or without BLT-1 does not depend on the oscillatory flow condition. Confocal analysis of the endothelial monolayer also shows decreased uptake in both 0 and 1 Hz flows without affecting the pro-

inflammatory stimulation of the 1 Hz OSS flow, which retained a comparable level of ICAM stimulation (~1.5X that of the 0 Hz LSS cases) to when ECs were conditioned under 1 Hz OSS without BLT-1 (Fig. 4.4D and E). This result is indicative of the endothelial response to eHNPs at 25 µg/mL with the 1 Hz OSS condition to be dependent on the availability of SR-B1. The significance of this conclusion is in the identification of multiple roles that SR-B1 may have when interacting with apoA1; while it has been known that interactions between SR-B1 and apoA1 could promote anti-inflammatory processes such as the production of endothelial NO and RCT, a pro-inflammatory response resulted from this interaction only when OSS was present.

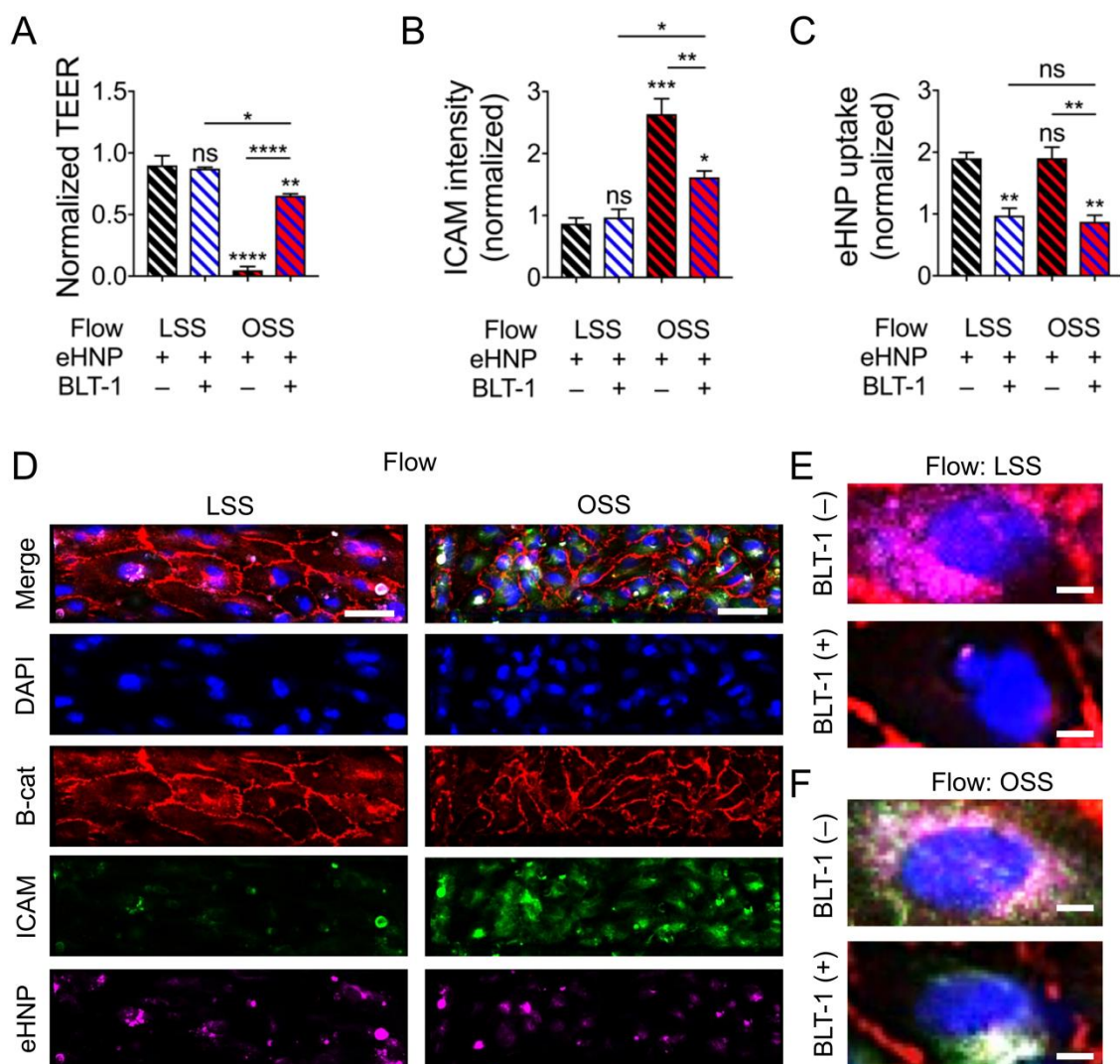


Figure 4.4. Endothelial response to eHNPs when SR-B1 is blocked.

(A) TEER, (B) ICAM, and (C) eHNP uptake LSS-normalized measurements under LSS or OSS conditions when BLT-1 is used (N = 3-4). TEER and ICAM values were normalized to LSS without eHNPs (0 μ g/mL), whereas eHNP uptake was normalized to LSS with eHNPs (1 μ g/mL). (D) Confocal images of the endothelium in response to BLT-1 pretreatment (scale bar is 40 μ m). (E) Zoomed confocal images comparing eHNP localization near nucleus under LSS and (F) OSS flow in response to BLT-1 (scale bar is 5 μ m). *, **, ***, and **** are for $p < 0.05$, 0.01, 0.001, and 0.0001 respectively.

4.4 CONCLUSIONS

This study applied a μ TM platform to track the interactions of the endothelium with microfluidically synthesized eHNP-A1, isolating the mechanism of protein-based interactions to be through apoA1. We identified a complex interaction between ECs and

eHNP-A1, which was dependent on several key factors: the flow profile of the microenvironment, the concentration of eHNP-A1, and the availability of SR-B1. Under the influence of LSS flow, eHNPs did not elicit a response from the endothelium over the range of concentrations from 0-25 $\mu\text{g/mL}$. Unlike with the LSS case, eHNPs did elicit a pro-inflammatory phenotype in ECs stimulated with an OSS flow. However, this pro-inflammatory response was only observed with the higher eHNP-A1 concentration (25 $\mu\text{g/mL}$). In order to determine if apoA1 was playing a key role in this inflammatory response, the apoA1 receptor SR-B1 was inhibited with BLT-1. The inhibition of SR-B1 still resulted in a proinflammatory response from the endothelium exposed to both OSS and eHNP-A1, however the degree of inflammation closely matched that of the OSS only case. The significance of these findings stems back to the original HDL hypothesis, which stipulates that increased blood concentrations of HDL could lead to lower CVD-related events. With much confusion surrounding clinical trials involving HDL-related therapies and their mixed results, the findings from this study help to elucidate some of this confusion. An apoA1-mediated pro-inflammatory EC response was found under OSS conditions, but was not found under LSS conditions. This was accomplished through the combination of our μVPM and μTM , which serve to synthesize and monitor our eHNPs under biomimetic conditions for CVD initiation. With these findings, future work that may be conducted to further expand our study could probe different parameters that we have yet to test. These parameters may include other compositions for eHNPs, a wider range of eHNP concentrations, and the use of gene sequencing or proteomics to visualize the endothelial gene/protein expression profile.

4.5 METHODS

Materials and chemicals

The reagent (3-aminopropyl)triethoxysilane (APTES) was purchased from Sigma-Aldrich Co. LLC. (St. Louis, MO). Polydimethylsiloxane (PDMS) was purchased as Sylgard 184 from Dow Corning (Midland, MI). The photoresist SU-8 and its developer were purchased from MicroChem Corp (Westborough, MA). HAECs were purchased from ATCC (Manassas, VA). 1,2-dimyristoyl-sn-glycero-3-phosphocholine (DMPC) and 1,2-dimyristoyl-sn-glycero-3-phosphoethanolamine-N-(lissamine rhodamine B sulfonyl) (Rhodamine-DMPE) were purchased from Avanti Polar Lipids, Inc. (Alabaster, AL). ApoA1 from human plasma and BLT-1 were purchased from Sigma-Aldrich Co. LLC. (St. Louis, MO).

Microfluidic transcellular monitor fabrication

The dimensions of the upper and lower microchannels were 200 μm x 100 μm and 100 μm x 50 μm respectively (width x height) [136]. Fabrication of the device started with Ag electrodes patterned onto glass slides using metal evaporation deposition [161]. The thin PDMS sheet for the lower microchannel was made by spin coating PDMS to 250 μm in height onto an SU-8 patterned silicon wafer. The upper microchannel was constructed using standard soft lithography to a patterned wafer. An 8 μm pore polycarbonate membrane (Sterlitech Corp, Kent, WA) was then treated in a 5% APTES solution at 80°C for device assembly prior to device housing [162]. The lower microchannel AgCl electrodes were produced using household bleach to soak the Ag electrodes for 1 hour at room temperature [163]. The fabricated device was housed in a polystyrene box for microfluidic cell culture using syringe pumps.

eHNP synthesis

The NP precursor solutions included a lipid solution that was composed of DMPC and Rhodamine-DMPE with a concentration of 2.75 mg/mL in 200 proof ethanol, and a

protein solution that had apoA1 with a concentration of 0.2 mg/mL in PBS (1X, pH 7.4). Syringe pumps from Harvard Apparatus (Holliston, MA) were used to pump the solutions into the μ VPM as previously described, from which the mixed solution was collected and then triple washed with PBS using a 30,000 MW centrifugal filter from EMD Millipore Corporation (Darmstadt, Germany) at a speed of 3900 rpm for 20 minutes [66]. The size distribution of the final washed sample was measured with a Zetasizer Nano ZS from Malvern Instruments (Worcestershire, United Kingdom).

Microfluidic endothelial cell culture

Prior to seeding cells into devices, HAECs were cultured in EGM-2 (Lonza, Basel, Switzerland) with 0.1% gelatin. Cell media was replaced every 3 days, with cultures being split at confluence. The device, housing, and tubing were sterilized with 70% ethanol and washed with DI-water and PBS (1X, pH 7.4) prior to coating the microchannels with fibronectin (50 μ g/mL) for 2 hs at 37°C. Cells were seeded into the devices at a concentration of approximately 1×10^7 cells/mL. Following a 1 h incubation at 37°C, devices were connected to Harvard Apparatus (Holliston, MA) PhD Ultra syringe pumps and exposed to 20 μ L/min while incubating at 37°C. Monolayers were allowed to culture for at least 24 h in order to mature before the addition of eHNPs or OSS [136]. For the SR-B1 inhibition studies, BLT-1 was incubated with the ECs at a concentration of 150 μ M for 1 h at 37°C before rinsing and adding eHNPs to the culture media.

TEER measurements

TEER measurements were taken every 12-24 hrs at 37°C using the EVOM2 volt-ohmmeter (World Precision Instruments, Sarasota, FL). A potential source of error is from noise in the TEER measurements, which was reduced by averaging multiple readings for

each device at every time point, and by taking all measurements at the same temperature inside of a cell culture incubator, as TEER can also be affected by temperature fluctuations. Measurements were normalized to the mature monolayer value developed under LSS relative to when there were no cells in the device (0 h).

Immunostaining of endothelial cells

Cell fixation was done using 4% paraformaldehyde (PFA) in PBS before permeabilizing in 0.1% triton. Samples were blocked with 1% bovine serum albumin (BSA) in PBS. Antibody incubation was with anti- β -catenin antibody (ab32572, Abcam, Cambridge, UK) and anti-ICAM-1 antibody (322713, BioLegend, San Diego, CA) or anti-VCAM-1 antibody (305806, BioLegend, San Diego, CA) at 4°C overnight followed by an Alexa Fluor 647 conjugated secondary antibody (ab150075, Abcam). Confocal microscopy imaging of the stained devices was done at 10X with a Zeiss LSM 700 microscope (Zeiss, Oberkochen, Germany).

Image analysis

Confocal images of each device were analyzed using the regions of interest (ROI) manager in ImageJ. Only the center ROI of the microchannels was compared between cases, as the center of the microchannel is the region where the endothelium experiences the desired shear stress [136]. The individual channels for eHNPs, VCAM/ICAM and β -catenin were used for ROI comparisons. Cell angles were calculated using ImageJ, and were defined as the angle between the vertical axis of the channel and the long axis of the cell, which was defined as the longest edge-to-edge distance through the center of the cell [67].

Statistical analysis

Statistical analyses were run in Prism 7 (GraphPad Software Inc, La Jolla, CA) and significance was defined as $p < 0.05$ (*). ANOVA tests were used for multiple comparisons.

4.6 SUPPLEMENTARY INFORMATION

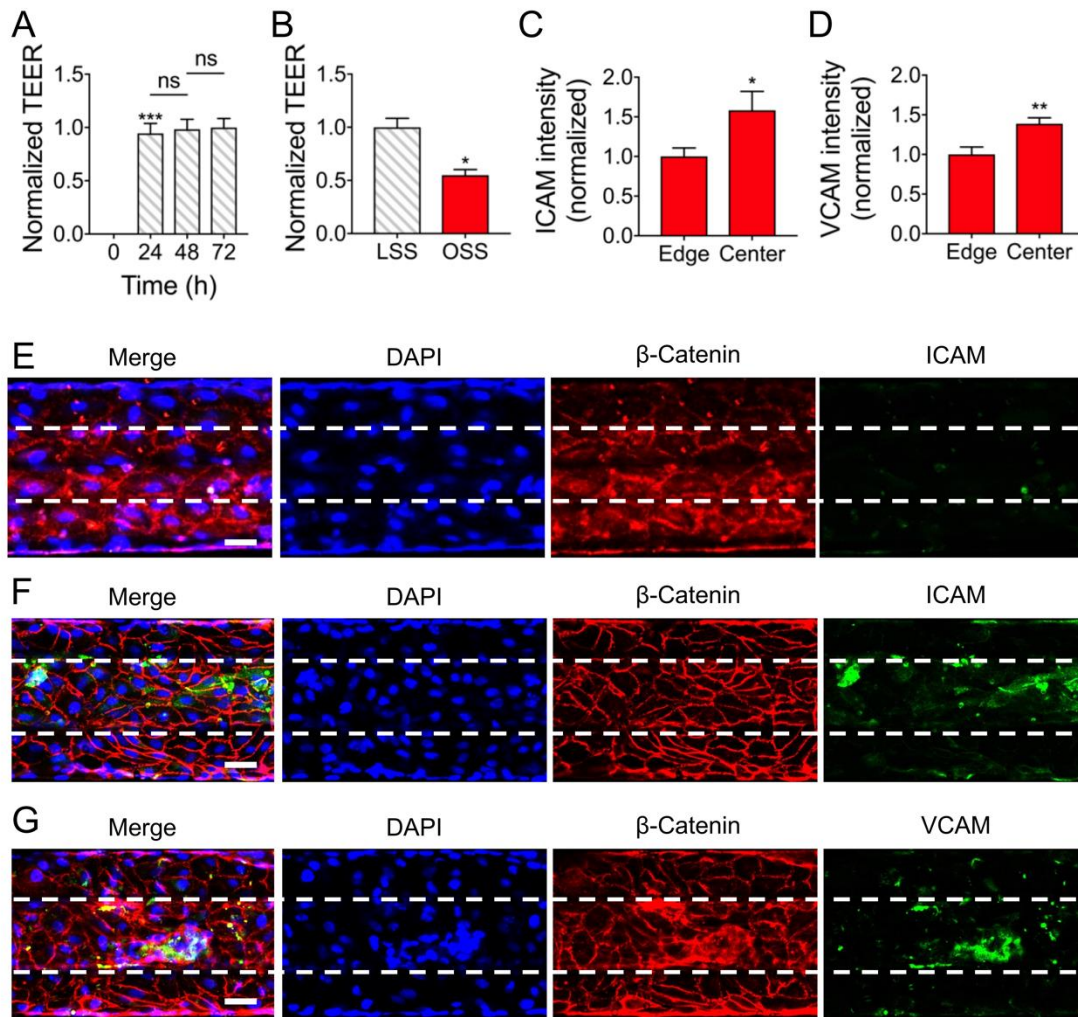


Figure S4.1. HAEC culture using collagen 1.

(A) Monolayer development was tracked with TEER over 72 hours (N = 3). (B) TEER LSS-normalized measurements under LSS or OSS conditions after 72 hours of LSS culture (N = 3). (C) ICAM and (D) VCAM localization to the center region of the HAEC monolayer (N = 8). (E) Confocal images of the LSS and (F) OSS stimulated monolayer stained for ICAM and (G) VCAM (scale bar is 40 μ m). *, **, and *** are for $p < 0.05$, 0.01, and 0.001 respectively.

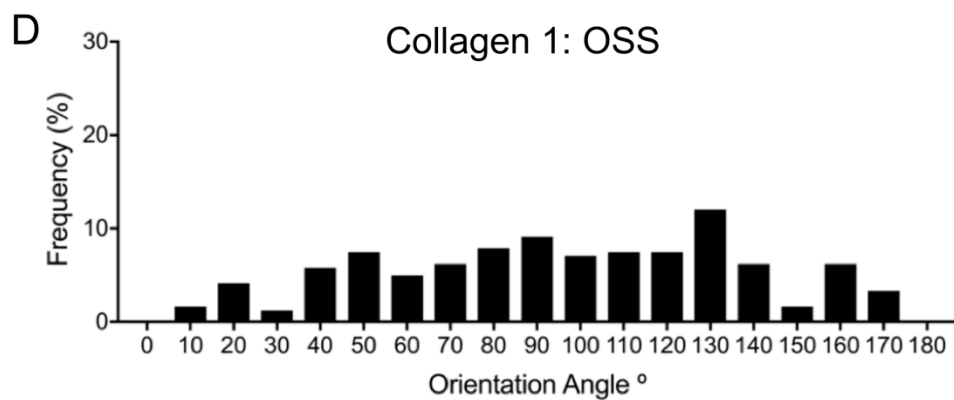
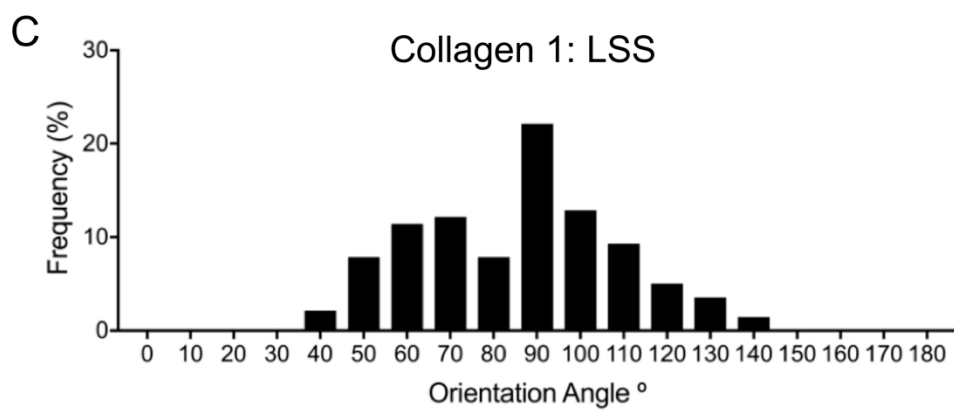
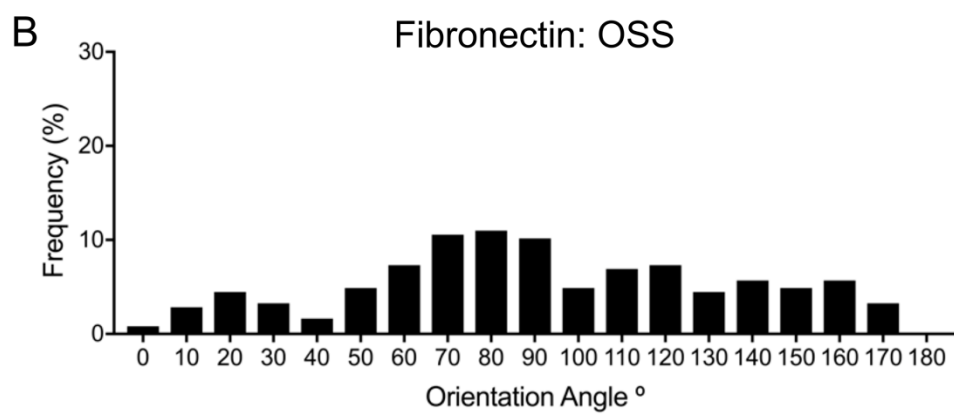
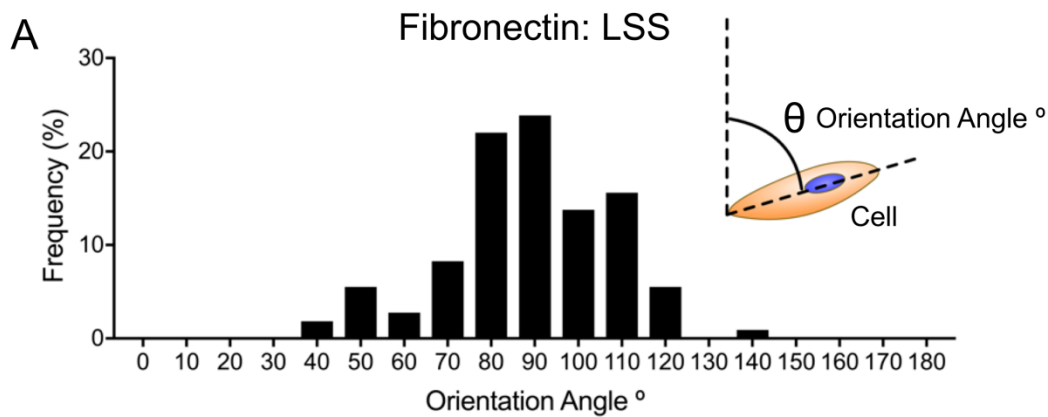


Figure S4.2. Orientation of HAECs under LSS or OSS.

(A) HAEC orientation relative to the vertical axis of the microchannel when cultured on fibronectin and treated with LSS or (B) OSS. (C) HAEC orientation when cultured on collagen 1 and treated with LSS or (D) OSS.

CHAPTER 5. CONCLUSIONS

5.1 CONCLUDING REMARKS

The vision for this work was centered around exploring the microfluidic methods in the engineering and screening of multifunctional nanomedicines. The studies conducted in helping to realize this vision reflect accomplishments in the detection of functional differences between HDL-mimetic NPs using microfluidics [66], the development of a biomimetic pathological microenvironment to study CVD-mediated endothelial responses [136], and the screening of interactions between HDL-mimetic NPs and endothelial cells cultured in the CVD-mimetic pathological microenvironment. These studies first required the development of the μ VPM platform that could continuously produce the necessary amount of NPs while maintaining NP monodispersity through efficient mixing of the nanoparticle precursors. The μ VPM was implemented alongside computational MD simulations and a microengineered vascular system to functionally compare eHNPs made from either natural apoA1 or a synthetic apoA1-mimetic peptide known as r4F, which showed that eHNPs made from natural apoA1 were more stable and could better trigger SR-B1 dependent endothelial responses. The need to develop the μ TM stemmed from the desire to study the endothelium under an oscillatory flow condition with real-time permeability measurements and end-point confocal analysis. This platform was implemented to both probe how the endothelium would respond to different oscillatory flow frequencies and to the addition of our eHNPs synthesized with our μ VPM. The resulting conclusions from these experiments that were enabled through microfluidics contribute to the understanding of how various microfluidic platforms may be implemented together for the translational process of experimental therapeutics. As a disclaimer, it is important to point out that the terms OSS and LSS were adopted for consistency with the terms used in the CVD community. However, flow in microfluidic channels is laminar. In our case, the

“LSS” flow profile was a unidirectional steady laminar flow and the “OSS” flow profile was a laminar flow that changed direction every half second.

5.2 CURRENT CHALLENGES AND FUTURE WORK

Currently, the initial challenge in designing and implementing microfluidic platforms is in the limited access to cleanroom facilities and the tools required to fabricate the molds for microfluidic channels. While some work has been done by various companies to make such tools more accessible without the need for a cleanroom, there still exists a substantially high investment that is required to enter the specialized field of microfluidics. This thesis aims to assist in standardizing the workflow for the development and the implementation of microfluidic platforms by providing a perspective into designing and applying microfluidic platforms through the context of both the synthesis of HDL-mimetic nanoparticles and the mimicry of a CVD-affected endothelial microenvironment. It should be noted that there is a key difference between the standardization of workflow and the standardization of design; the standardization of workflow identifies checkpoints in platform development that are to be kept constant, whereas the standardization of design identifies key parameters or characteristics of the engineered platform that need to be kept constant. Other challenges include the technical difficulty in assembling complex multi-layer platforms, as well as the determination of key design parameters during the conceptualization of new microfluidic platforms. The studies to follow-up the results from chapters 2-4 have been outlined below.

ApoA1-mimetic peptide potential

The results of chapter 2 showed that for a given composition of HDL-mimetic nanoparticles, apoA1-based nanoparticles were more stable and effective in soliciting

cellular responses than r4F-based nanoparticles. The work that should immediately follow this study should explore additional HDL-mimetic compositions. It should be well noted that the comparisons between apoA1 and r4F were done in the context of a single simplified composition used for both diagnostic and therapeutic applications. With this study using the simplest form of reconstituted HDL to compare apoA1 to r4F, the modification of the nanoparticle formulation to compare their respective functionalities would provide further insight into ways nanoparticle formulation may modulate the degree to which r4F and apoA1 differ. For instance, modifying the composition to incorporate polyethylene glycol (PEG) to the surface of the nanoparticles may improve the stability [171], and overall performance, of the r4F-based nanoparticles while maintaining the stable properties of apoA1-based nanoparticles. In addition, applying this same comparison method with additional well-used apoA1-mimetic peptides, such as ETC-642 [172], could be insightful to how other apoA1-mimetic peptides may trigger known apoA1 pathways. Having multiple apoA1-mimetic peptides to compare may also enable studies to understanding the intricacies of how apoA1 functions.

Balancing the complexity and robustness of the μ TM

The microfluidic transcellular monitor (μ TM) is a robust platform that can monitor the permeability of an endothelial monolayer, which was shown in a simplified cellular microenvironment with endothelial cells. Biology is much more complicated; striking a balance between complexity and usability for microphysiological systems is a major challenge. The immediate work to follow the μ TM would be to try and find this balance by including additional peripheral cell types, such as fibroblasts or vascular smooth muscle cells, to shift the endothelial microenvironment to be more physiologically relevant. This could be done by culturing these peripheral cells under static conditions on the underside of the porous membrane to monitor how the peripheral cells may interact with the

endothelium that is under flow. In addition, several groups have begun to shift to impedance-based measurements for endothelial permeability due to its robustness in fine-tuning measurements across multiple frequencies [75]. Incorporating platinum or gold electrodes in place of the silver chloride electrodes may improve the accuracy of the TEER measurements taken with the μ TM.

Exploring the pro-inflammatory effects of eHNP-A1

Since it has been reported that natural HDL functionality can be modulated through its oxidation by reactive oxygen species (ROS) [33], measurements of the ROS levels generated in the μ TM during OSS and LSS conditioning of the endothelium could provide insightful data to the endothelial microenvironment affecting eHNP-A1. Should there be a significant difference between the levels of ROS generated between LSS and OSS conditions, an antioxidant should be then used to see if there is any change in the response of the endothelium to eHNP-A1 under OSS and LSS conditions. In addition, comparing this response to purified natural HDL and purified oxidized HDL may provide further insights into the contributions of oxidation. This study should take into account the lot from which the HDLs are purified due to the compositional variation of natural HDLs. Therefore, multiple lots must be used across purified HDL and purified oxidized HDL during comparisons.

Long-term vision

Long-term future directions for the studies presented in this work may include the development of an eHNP library to track how the endothelium may respond to various compositions of eHNPs, and to comparing the responses between human and animal-derived endothelial cells in order to determine the sensitivity of these cells to physiological conditions specific to their species. Natural HDLs have a complex lipidome and proteome.

It is known that various lipids and proteins like sphingosine-1-phosphate (S1P), cholesterylester transfer protein (CETP), and paraoxonase-1 (PON1) can be a part of HDL's composition while contributing to and modulating HDL's functionality [33]. The difficulty in studying these processes from human purified HDLs is in the heterogeneity of HDL's composition; however, with our compositional control over the eHNP formulations, microfluidic platforms are well-positioned to tackling this challenging question. A library that can track all these responses would be an incredibly powerful tool to multiple research communities, as it will provide a way to organize and relate the functional contributions of each component within a controlled microenvironment.

Microfluidic platforms mimicking organ-specific microenvironments use parameters most physiologically relevant to that of humans in order to study cellular responses in human-like conditions. However, many of these studies may end up being paired with animal models to validate how the microfluidic model responds to certain external stimuli. An important factor to keep in mind when conducting such validation studies is that the motivation of developing microfluidic human-like *in vitro* models originates from the inherent differences between animal models and humans. Therefore, it would be imperative to compare how animal and human cells respond to their respective physiological microenvironments within a microfluidic platform before comparing the results obtained from the microfluidic platform to results obtained from an animal model. In the case of CVD and the endothelium, parameters over which to study these differences would include flow frequency and shear stress between mouse and human aortic endothelial cells. Depending on the availability of aortic endothelial cells from various species, the study could also be extended to probing therapies that failed in clinical studies that also succeeded in various animal trials. Such comparisons would yield highly impactful results that would help to uncover explanations to the differences between animal and human models.

APPENDIX A. MICROFLUIDIC CELL CULTURE AND ELECTRODE FABRICATION

A.1. OVERVIEW

This protocol describes the process flow for the assembly and use of the μ TM. The μ TM is a microfluidic tool for studying the barrier function of cells in response to changes in mechanochemical environments that can be changed through the flow conditions and media composition. This device combines the recording of TEER, fluorescent microscopy, and media sampling for the collection of data.

The basic points to making and using this device are as follows:

1. Fabrication of the electrodes and silicon wafers
2. Softlithography of PDMS to the silicon wafers
3. Assembly of the device through plasma cleaning
4. Assembly of the device housing
5. Prep needed for cell seeding
6. Seeding cells
7. Initiating culture under flow

A.2. ELECTRODE FABRICATION

Materials and equipment by process flow:

1. Cut and clean glass wafers
 1. Large glass slide (Ted Pella 260233 6"x4.5")
 2. Glass cutter (McMaster-Carr 3867A11)

2. Pattern glass wafers with photoresist
 1. Teflon dish for 100mm wafers
 2. Large glass dish for wafers larger than 100mm
 3. Transparency mask for electrode pattern
 4. Timer
 5. Wafer tweezers
 6. Provided by IEN
 1. Buffered oxide etch (BOE) **WARNING: CONTAINS HF**
 2. Futurrex NR9-1500py positive photoresist
 3. Futurrex RD6 Developer
 4. DI Water
 5. Texwipes
 6. Oven
 7. Hot Plate
 8. Nitrogen gun
 9. Aluminum foil or parafilm
 10. Spin Coater (BLE or SCS)
3. Deposit metal onto patterned glass wafers (material/equipment provided by IEN)
 1. Vision RIE 2
 2. Titanium
 3. Silver
 4. CHA E-Beam Evaporator 2
4. Metal liftoff
 1. Large glass dish for 100mm wafer
 2. Acetone
 3. Waste container (empty acetone bottle)

4. DI water
5. Glass cutter

Cutting glass slides

Cut the glass slides as per the following drawing - these cut glass slides will now be referred to as wafers:

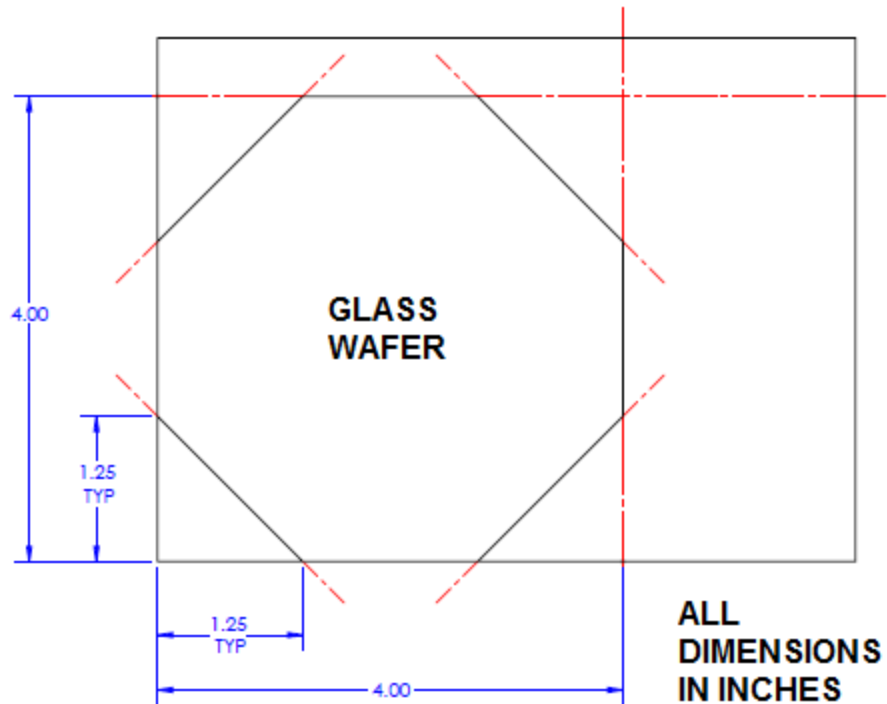


Figure A.1. Cutting diagram for glass slide.

Patterning the glass

1. Pour BOE (Located in "A" cabinet) into a teflon dish, and submerge one glass wafer at a time into the dish for 1 minute each.
2. After soaking the glass wafer in BOE for 1 minute, thoroughly rinse the glass slide under cold running DI water.

3. Use the nitrogen gun to blow off the water while using a paper towel to absorb any water that run to the edges of the glass.
 - a. Always start the nitrogen gun at the center of the wafer and then move away from the center. Do not move the nitrogen gun back to the center while on as it risks water being blown back onto the wafer. Do this step as carefully as possible.
4. Place the cleaned wafer into a 100°C oven for a minimum of 15 minutes as a dehydration bake.
5. Set one hotplate to 100°C and another for 150°C and label that they are in use.
6. While the wafers are baking, set the spin coater for a 30 second spin at 2000rpm with a 1000rpm/s ramp.
7. Spin the NR9-1500py photoresist onto the wafers.
 - a. if using the BLE spinner, use a 6 in wafer chuck and seal the chuck with aluminum foil (or parafilm). After sealing the foil to the chuck, poke holes at the center ridges of the chuck so that the vacuum will have a tight seal with the glass wafer.
8. Place the coated wafers onto the 150°C hotplate for 7 minutes as a softbake.
9. Expose the wafers with a mask aligner holding the electrode mask using 780mJ/cm².
10. Place the newly exposed wafers onto the 100°C hotplate and bake for 17 minutes as a post exposure bake.
11. In the hood, fill a glass dish half way with RD6 and set a timer for 12 seconds.
12. **Have gentle running DI water ready for this next step** - Immerse the baked glass wafers into the developer for **11.5** seconds and then **IMMEDIATELY** place the wafer under the running DI water to wash off the developer (do this for

roughly 1 minute) - the development is extremely time sensitive, have the glass wafer under running DI water at the 12 second mark.

13. Dry the wafers with a nitrogen gun.

Metal deposition

1. Use an RIE (ex. the Vision RIE 2) to run a descum process on the wafers:
 - a. Process Pressure and RF setpoint - 250 torr.
 - b. Stabilization time - 45 seconds.
 - c. Gases: Argon-5 Oxygen-50.
2. After running the descum, deposit metal onto the wafer surface using a metal evaporator:
 - a. a 50nm (0.5kÅ) layer of Ti with a deposition rate of 1Å/s.
 - b. a 500nm (5kÅ) layer of Ag with a deposition rate of 3Å/s.

Metal liftoff

1. Fill a glass dish with acetone and another dish with DI water.
2. Immerse silver coated wafer in the acetone and use wafer tweezers to rock the wafer up and down until the silver lifts off the surface.
3. Remove the wafer from the acetone and place in the DI water.
 - a. If the acetone dish is full of detached silver, dispose of solvent waste into a labeled waste container and refill with new acetone.
4. Use the nitrogen gun to remove any water or detached silver from the wafer.
5. Cut out each individual device using the glass cutter.

A.3. μ TM ASSEMBLY

Materials and equipment:

1. PDMS (Sylgard 184 Elastomer Kit)
2. Glass electrodes
3. Silicon wafer molds (Upper and Lower channel molds)
4. Polycarbonate membrane - 8 μ m pore (Sterlitech PCTB8025100)
5. (3-Aminopropyl)triethoxysilane a.k.a. APTES 5% solution in DI water (Sigma 440140)
6. Biopsy punch 1mm
7. Biopsy punch 4mm
8. Tygon silicon tubing (Cole Parmer 95702-00)
9. PE60 tubing (BD Intramedic 427415)
10. Clear plastic container (Ted Pella 139-75)
11. 100mm petri dish filled with cured PDMS
12. 100mm petri dish filled with kimwipes
13. 60mm petri dish
14. Benchtop microscope
15. Scissors
16. Precision knife
17. Tweezers
18. Hot plate (80°C)
19. Plasma cleaner
20. Oven (80°C)
21. Microscope glass slide
22. Paper-based masking tape – for clamping
23. Scotch magic tape (3M 810) – for cleaning
24. Soldering Iron

- 25. Solder
- 26. Silver wire (A-M systems 783000)
- 27. Socket connector (Digikey ED10864-ND)
- 28. Shrink tubing (McMaster-Carr 7856K72)
- 29. Sealant glazing rope (McMaster-Carr 1049A31)
- 30. Silver epoxy (MG Chemicals 8330S-21G)

Procedure:

- 1. Cure PDMS to the upper channel mold so that the height is between 5 and 10mm from the surface of the silicon wafer.
- 2. Spin PDMS onto the lower channel mold using the following recipe:
 - 1. Step 1: 100rpm at 50rpm/s for 10 seconds.
 - 2. Step 2: 250rpm at 50rpm/s for 93 seconds.
 - 3. Cure on hotplate at 100°C for 5 minutes -or- 80°C for 20 minutes.
- 3. Plasma bond a lower channel PDMS device to the glass electrode
 - 1. Clean the glass electrode slide 3 times with tape and leave tape on after 3rd cleaning.
 - 2. Place a lower channel section cutout channel side **UP** onto the PDMS petri dish (make sure that the cutout lower channel section is not large enough to cover the electrode pads).
 - 3. Punch the 4mm holes all the way through the 4mm hole markers and remove punches using tweezers.
 - 4. Place lower channel flat onto a clean glass slide channel side **DOWN**.
 - 5. Clean the backside of the lower channel with tape 3 times.

6. Remove the lower channel from the glass slide and place it channel side **DOWN** into the plasma cleaner with the glass electrode (make sure to remove all tape from devices).
 7. Plasma clean for 1 minute on the RF Hi setting.
 8. Making sure to align the 4mm holes with the 4mm electrodes, bond the glass slide to the lower channel PDMS (handle glass electrode instead of lower channel while doing this).
 9. Place a paper-taped glass slide on top of the device (tape side to the PDMS) and clamp with a binder clip before placing in an 80°C oven for at least 20 minutes.
4. Cut and treat polycarbonate membranes for bonding
 1. Place glass vial APTES solution onto a 80°C hot plate - **Loosen lid to avoid pressure buildup.**
 2. Roughly cut out 5mmx10mm sections of the polycarbonate membrane.
 3. Place the membrane cutouts into a 60mm dish (without the lid).
 4. Plasma clean membrane cutouts for 1 min.
 5. Place the plasma cleaned membrane cutouts into the warmed APTES solution for at least 20 minutes.
 6. Dry the membrane cutouts on kimwipes in a petri dish - **Separate overlapping/folded membranes before fully dry.**
 5. Assembling PDMS components together
 1. Take the lower channel assembly out of the oven and remove the clamp taped glass slide.
 2. Clean the lower channel assembly with tape 3 times.
 - i. **IMPORTANT:** check to make sure that the PDMS is firmly bonded to the glass slide, if not then dispose of the assembly immediately.

3. Cut out and punch inlet/outlet holes for the upper channel using a 1mm biopsy punch (punch into the PDMS from the channel side).
4. Clean the upper channel, channel side **UP**, with tape 3 times.
5. Plasma clean the lower channel assembly and upper channel; both should be channel side **UP**.
6. Immediately apply a dried membrane cutout onto the lower channel, making sure to center and cover the majority of the long straight section
7. Bring lower channel assembly and upper channel to the microscope, and bond the two together using the following procedure:
 - i. Clamp down the lower channel assembly with the microscope sample clips.
 - ii. Adjust the microscope lens so it is focusing slightly above the lower channel surface.
 - iii. Hold the upper channel PDMS above the lower channel assembly.
 - iv. Carefully align the upper and lower channels so that the lower channel is centered between the upper channel.
 - v. Gently press the two sections together and clamp them together with a taped glass slide and binder clip.
 - vi. Leave the assembly in the oven for 15 minutes.
6. Prepare the silver epoxy (1:1 ratio) and dip one end of a 2" length of silver wire into the epoxy.
7. Place the epoxy coated end of the wire on the electrode pad and push down using tweezers to insure adequate adhesion (1 wire per pad).
8. Allow the silver epoxy to cure in an 80°C oven for 24 hours.
9. Apply heat shrink to the wires, leaving 1cm at the un-adhered end of the wire exposed.

10. Drill four 7/64" holes (marked red) into the back of a box using the diagram / image below as a reference:

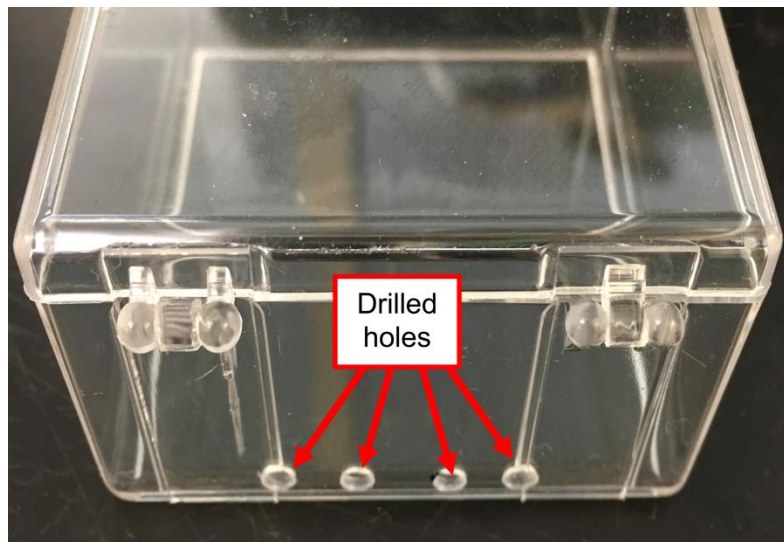
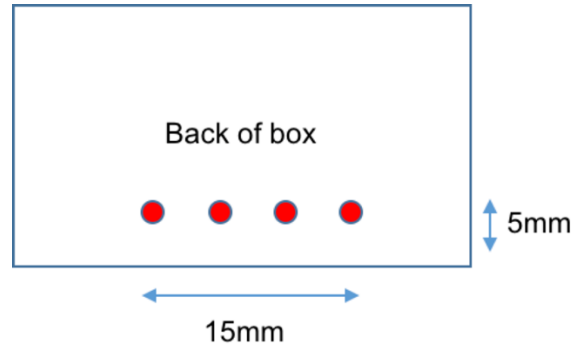


Figure A.2. Location of drilled holes for wires of μ TM.

11. Clean out the machined box and place the soldered chip into the box with the 4 wires coming out of the holes.
12. Cut out small pieces of the sealant glazing rope.
1. Use one piece to secure the device to the bottom of the container -
Smaller pieces are better imaging.
 2. Using tweezers, surround the wires where they come out of the holes and push the glazing into any open gaps. See images below for reference.

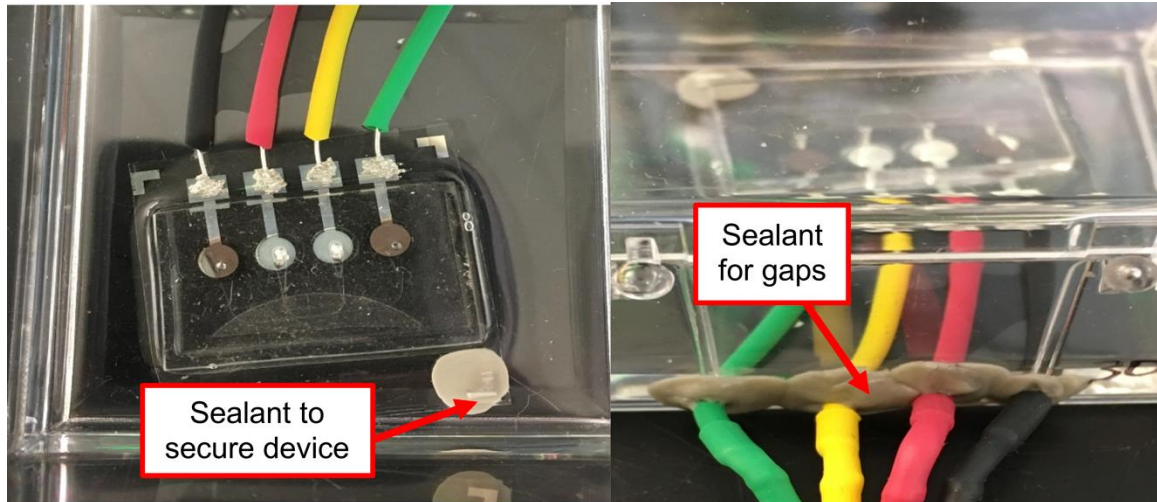


Figure A.3. Location of sealant for μ TM.

13. Pour roughly 10 grams of PDMS around the device to fix it in place, making sure to pour over the wires. **The silver epoxy and wires must be completely submerged in PDMS.** Bake in the 80°C oven to cure.
14. Solder the connectors to the end of each exposed wire and insulate the solder joint with heat shrink tubing.
15. Dip the end of the connectors in silver solder and insert them into a strip of four socket connectors. **Use as little epoxy as possible to avoid shorts.** Allow epoxy to cure in an 80°C oven for 24 hours.
16. Mark the inlets/outlets on the lid of the box, and drill a hole into the lid for each inlet/outlet using the 7/64" bit (remove the lid from the device before doing this, and the reattach when complete). See below image for reference.

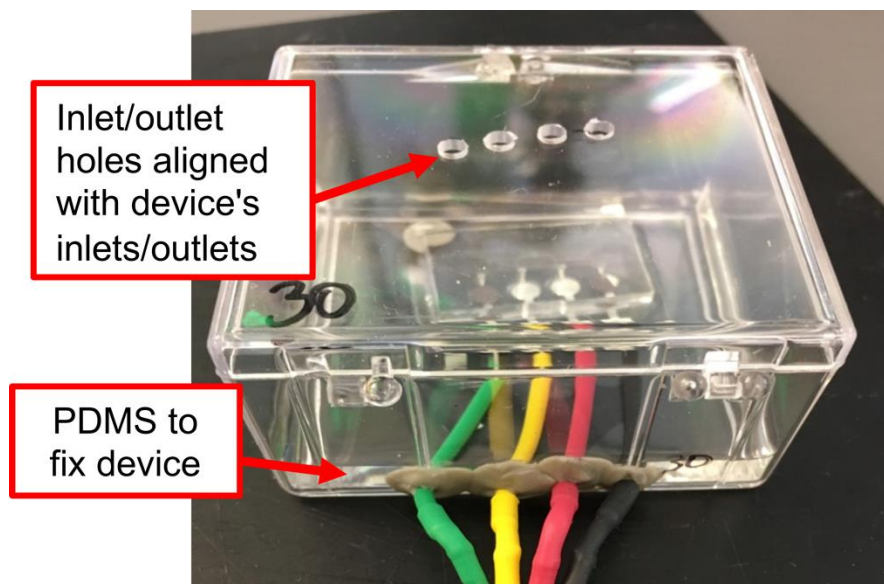


Figure A.4. Final device ready for cell culture.

17. Prepare 3 sets of tygon tubing at least 10cm long with 1cm long PE60 tubing adapters.
 1. DO NOT autoclave the PE60 tubing adapters. To sterilize, leave the tubing sets under UV overnight.
 2. Do not place the device in UV or the autoclave because the polycarbonate membrane is not autoclavable and the silver electrodes are sensitive UV light. Sterilization will be done with ethanol.

A.4. CELL CULTURE

Materials and equipment:

1. Assembled device with tygon/PE60 tubing sets
2. Syringe pump (Harvard apparatus PhD Ultra)
3. Tygon silicon tubing (Cole Parmer 95702-00)
4. PE60 tubing (BD Intramedic 427415)
5. 3mL syringes (BD 309657)

6. 30mL syringes (BD 302832)
7. 18G needles (BD 305180)
8. 70% ethanol
9. PBS 1X
10. Fibronectin (50 μ g/mL)
11. Cell sample (1 confluent T25 flask) and cell growth media
12. Bleach (to chlorinate electrodes)
13. 1-10 μ L pipette and tips
14. 20-200 μ L pipette and tips
15. 100-1000 μ L pipette and tips
16. Centrifuge
17. Tweezers

Procedure:

1. Add a 3 μ L droplet of bleach to the lower channel inlet/outlet (the outer inlet/outlet) and let set for 1hr at room temperature
 1. Make sure the entire electrode is covered
2. Add a 3 μ L droplet of ethanol to the upper channel inlet/outlet (the inner inlet/outlet pair) and fill completely without an air bubble developing inside.
3. Fill a 3mL syringe with 70% ethanol and connect it to an 18G needle with tygon tubing and PE60 tubing assembled together
4. Connect one of the upper channel inlet/outlet to the ethanol containing 3mL syringe and use a syringe pump to flow ethanol through the device at 100 μ L/min
 1. It is important to let the whole 3mL flow through the device to avoid the bleach in the lower channel from coming in contact with the upper channel electrodes

5. Aspirate out the ethanol with bleach and immerse the chip in ethanol by filling the box with 10mL of 70% ethanol.
6. Bring the device into the tissue culture hood after spraying it down with ethanol, and aspirate the ethanol covering the device.
7. Cover the device in PBS 1X, and using a 200 μ L pipette SLOWLY INFUSE 200 μ L of PBS through the upper channel. You should see the ethanol leaving the upper channel. Do this 3 times.
8. Aspirate out the the PBS covering device, and replace with an additional 10mL of PBS.
9. Using a 200 μ L pipette, SLOWLY WITHDRAW 200 μ L of PBS from the lower channel (making sure to withdraw liquid from both inlets/outlets). Repeat this 3 times and replace the PBS with new 10mL of PBS.
10. Thread the tubing sets for the device through the holes in the lid for the inlets/outlets.
 1. Since there are only 3 tubes and 4 holes, thread two of the tubes through the lower channel holes and one of the tubes through the upper channel hole. The red circles will indicate which holes to use.

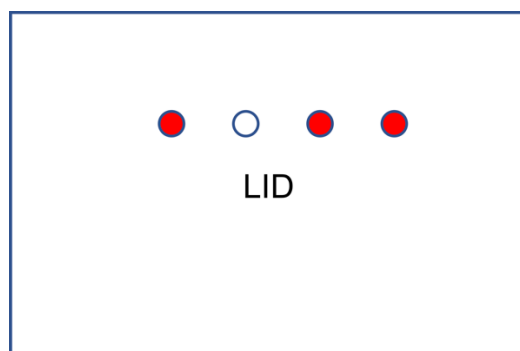


Figure A.5. Location of holes in lid for tubing.

11. Fill the tubes with PBS using a 3mL syringe, and insert them into the corresponding inlet/outlet for the hole the tube was threaded through.
12. Clamp each of the tubes and check for bubbles. If any bubbles exist then gently withdraw PBS through the device to dislodge them.
13. Aspirate out the PBS ontop of the device, and unclamp the upper channel tube.
14. Infuse 100 μ L of fibronectin solution through upper channel inlet/outlet that is not connected to the tube. Reclamp the tube and incubate the device at 37°C for 1 hour.
15. Flush out the fibronectin by infusing another 100 μ L of PBS1X.
16. Using a 200 μ L pipette and slowly infusing through the tube-free upper channel inlet, displace the PBS in the device with cell growth media. Use the clamps on the tubes to direct flow. Thread a lower channel inlet through the top of the second box lid that will act as a media reservoir for the lower channel.
17. Trypsinize the cells in the T25 flask and aspirate out as much media as possible before adding 100 μ L of media. Mix well using a 1000 μ L pipette set to 100 μ L.
18. Making sure to have the lower channel tubes clamped and the upper channel tube unclamped, infuse 60 μ L of cell solution into the tube-free upper channel inlet.
19. Remove the pipette tip first, and then clamp the upper channel tube **immediately**
20. Allow the device to incubate for 1 hour at 37°C.
21. Add 30mL of media to the top of the device as well as the media reservoir for the lower channel.
22. Having one syringe pump set to Upper and the other set to Lower, withdraw media through the device for 24 hours before checking on status of monolayer.
 - i. UPPER:

1. Ramp up flow rate from 2 μ L/min to appropriate shear stress for cell type
- ii. NOTE: Make sure all of the tubing is prefilled with media – air is a compressible fluid and will affect the ability of the syringe pump to pull media through the device.

APPENDIX B. NANOPARTICLE SYNTHESIS WITH MICROFLUIDICS

B.1 OVERVIEW

This protocol describes the process flow for the synthesis of eHNPs using the μ VPM platform. The μ VPM is a microfluidic tool for mixing precursor solutions together for the synthesis of nanoparticles. This device was primarily used for the synthesis of the eHNPs we used for the studies presented in this work.

B.2 SYNTHESIS PROTOCOL

Materials:

1. Harvard Apparatus PhD syringe pump (x2)
2. μ VPM chip
3. Becton Dickinson (BD) Intramedic polyethylene (PE) tubing, ID0.03in x OD0.048in, num. 427416
4. Cole Parmer Tygon Silicone (CP) tubing, ID0.031in x OD0.093in, num. 95702-00
5. BD blunt fill needle 18G (1.2mm x 40mm), num 305180 (from VWR)
6. Plastic BD syringe (need a total of 4 syringes, one of which is 10mL)
7. Scissors
8. Calipers
9. Binder clips (need at least 4)
10. Synthesis Table (last page of protocol)
11. Precursors and solvents
 - a. For eHNP-A1: apoA1, DMPC lipid, 1X PBS, and 200 proof ethanol.
12. Collection bottle/tube.

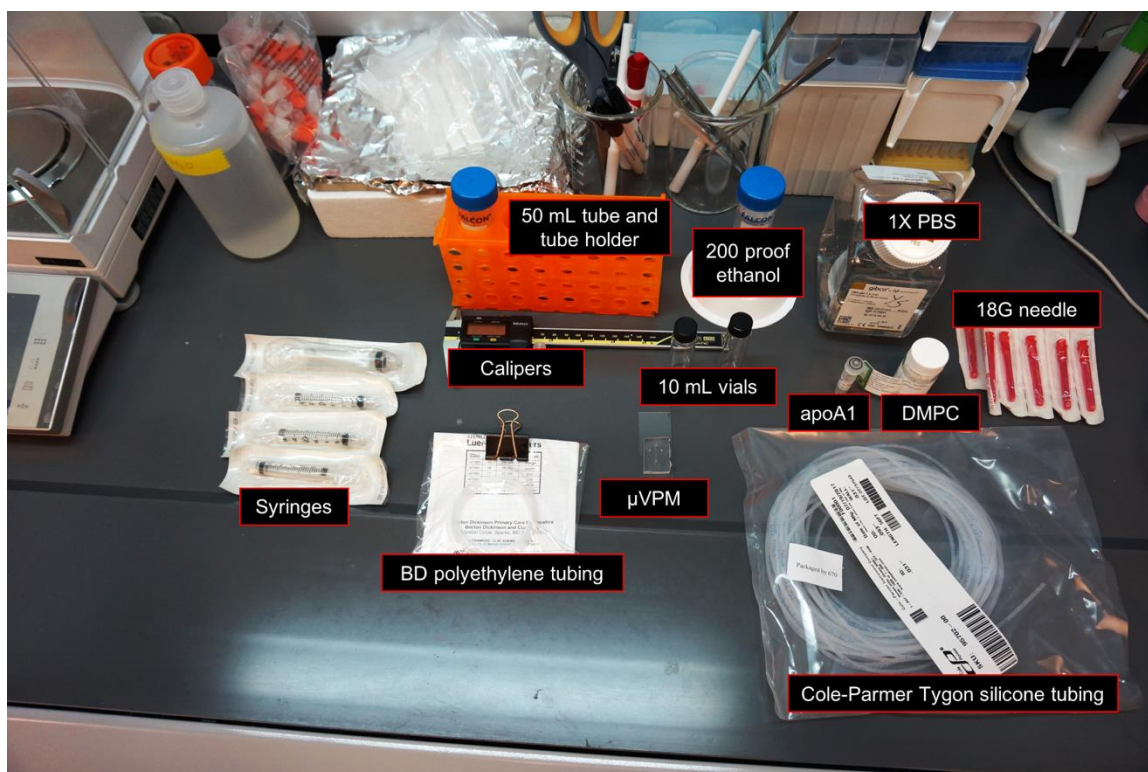


Figure B.1. Materials used in the synthesis of eHNPs.

Methods:

1. Set one syringe pump to use a 10 mL syringe running at 1 mL/min (force setting should be 100%).
2. Take out precursor components from the freezer and allow to thaw at room temperature.
3. Insert one BD needle into one end of the CP tubing.
4. Use the calipers to cut 10 cm sections of CP tubing measured from the tip of the needle inside the CP tubing.



Figure B.2. Measurement of tubing.

5. On the other end of the 10 cm section of CP tubing holding the BD needle, insert ~5 mm of PE tubing.

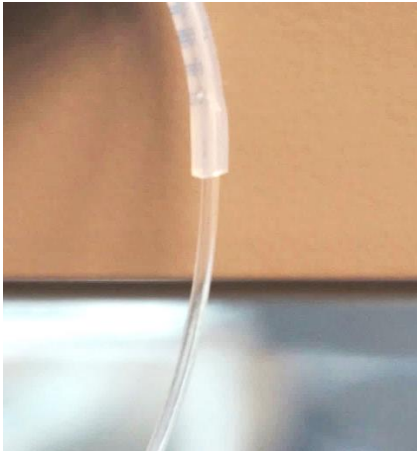


Figure B.3. PE tubing inserted into CP tubing.

6. Cut the PE tubing so that 1cm of the PE tubing is protruding from the CP tubing.
7. Repeat steps 3-6 to have a total of three 10 cm CP tubing segments.
8. Make another CP tubing segment with a BD needle and PE tubing segment, but cut the CP tubing significantly longer (about 30-40 cm).

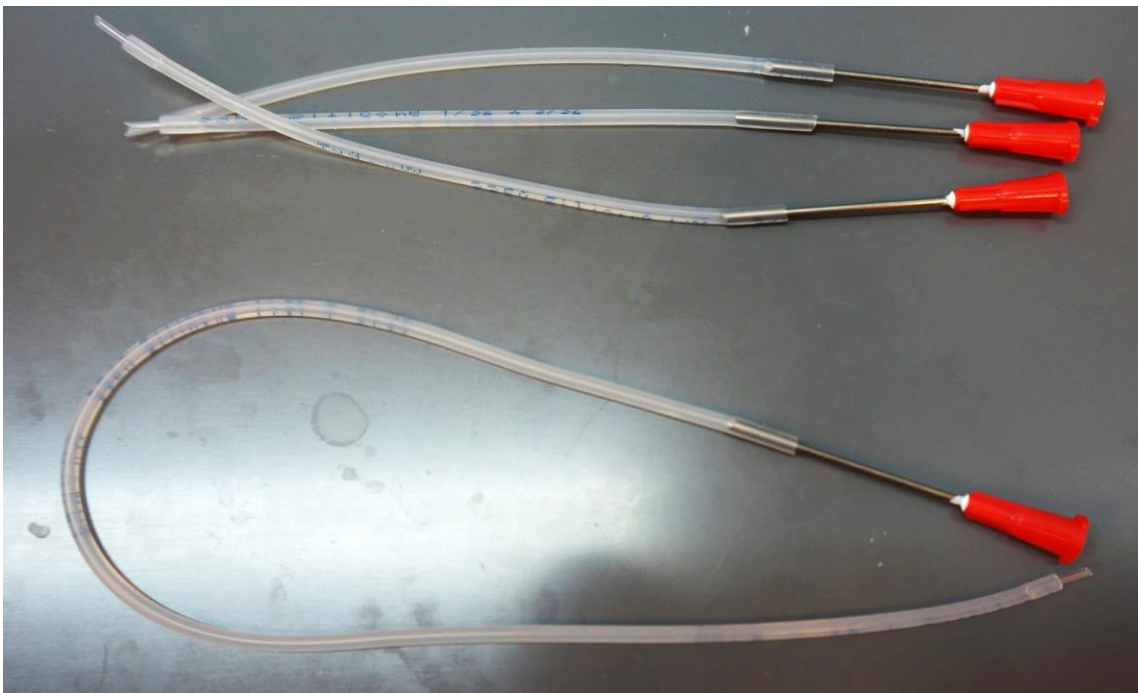


Figure B.4. Assembled tubing with needles and adapters.

9. Make a luer lock valve using a BD blunt fill needle, a 2 cm segment of CP tubing, and a binder clip.
10. Remove the plunger from a 10 mL syringe, and then plug the luer lock with the make shift valve. Fill the syringe with your primary nanoparticle solvent from the top (e.g. 1X PBS) and reassemble the syringe, making sure to remove any bubbles.
11. Connect the three 10 cm tubes with needles to the 3 inlets of the μ VPM chip (all are on a single side). Note that the PE tube should be inserted into the inlets
12. Connect the final, longer, tube with needle to the outlet.



Figure B.5. Assembled μ VPM with tubing.

13. Setup the 10 mL syringe in the syringe pump, and attach the syringe to the needle of the outlet tubing.
14. Place the needle ends of the inlet tubing segments into a plastic cup and run the syringe pump at 1 mL/min for 10 minutes.
15. Start preparing precursor solutions from thawed precursor components. For eHNP-A1, prepare a 0.2 mg/mL solution of apoA1 in 1X PBS and a 2.75 mg/mL solution of DMPC in 200 proof ethanol.
16. Evenly divide the aqueous precursor between two of the three syringes, and fill the remaining syringe with the lipid precursor. Make sure to remove any bubbles from the syringes.
17. Turn off the syringe pump and clamp all 4 tubes with binder clips.
18. Remove the 10 mL syringe from the pump.
19. Attach the two aqueous precursor syringes to the two outer inlet needles. Prevent any bubbles from forming by creating a liquid interface between the outlet of the syringe and the droplet inside the needle.
20. Attach the lipid precursor syringe to the center inlet needle using the same technique as described in the previous step to prevent the formation of bubbles.
21. Setup the aqueous precursor syringes to one syringe pump, and the lipid precursor syringe in the remaining syringe pump. Make sure to have the appropriate settings on each pump for the syringe types used (e.g. 3 mL Plastic Syringes).
22. Set the center syringe pump to infuse at 0.8 mL/min.
23. Set the outer syringe pump to infuse at 2.2 mL/min.
24. Cut the outlet tube so that about 5 mm of tubing is protruding from the μ VPM chip.

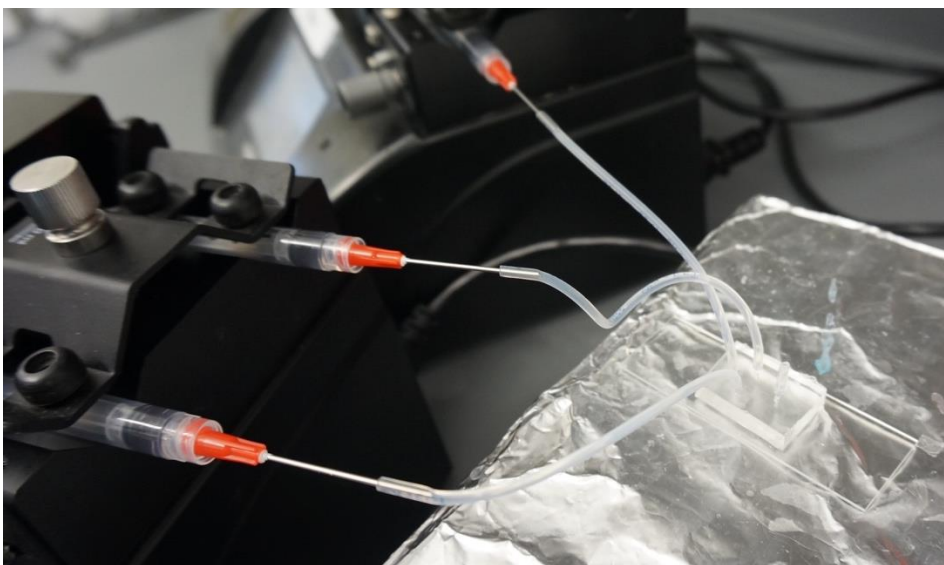


Figure B.6. μ VPM ready for synthesis.

25. Place the cut end of the outlet tube into a collection tube or bottle.



Figure B.7. Collection of nanoparticles from eHNPs.

26. Remove the clamps and run both syringe pumps.
27. Collect the resulting nanoparticle solution (avoid collecting the final drops during synthesis after the syringe pumps are stopped).
28. Transfer the nanoparticle solutions to the appropriate centrifugal filter (usually 10,000 or 30,000 MW filter). Add 10 mL of 1X PBS to the filter and centrifuge at 3900 RPM for 20 min. Avoid long wait (> 5 min) times between nanoparticle collection and centrifugation.
29. Centrifuge the nanoparticles for a total of 3 times, discarding the filtrate and adding more 1X PBS each time.

30. Collect the nanoparticles from the centrifugal filter using a 200 μL pipette. Gently rinse the filter membranes with the nanoparticle solution before transferring the solution to another tube/vial.
31. Characterize the nanoparticles using DLS to verify the particle size.

APPENDIX C. RIGHTS AND PERMISSIONS

Rights and permissions were obtained for the following works for reuse:

1. Fernandez-Friera, L., et al., *Prevalence, Vascular Distribution, and Multiterritorial Extent of Subclinical Atherosclerosis in a Middle-Aged Cohort: The PESA (Progression of Early Subclinical Atherosclerosis) Study*. *Circulation*, 2015. **131**(24): p. 2104-13.
2. Nam, D., et al., *Partial carotid ligation is a model of acutely induced disturbed flow, leading to rapid endothelial dysfunction and atherosclerosis*. *American Journal of Physiology-Heart and Circulatory Physiology*, 2009. **297**(4).
3. Son, D., et al., *The atypical mechanosensitive microRNA-712 derived from pre-ribosomal RNA induces endothelial inflammation and atherosclerosis*. *Nature Communications*, 2013. **4**.
4. Karnik, R., et al., *Microfluidic Platform for Controlled Synthesis of Polymeric Nanoparticles*. *Nano letters*, 2008.
5. Kim, Y., et al., *Mass Production and Size Control of Lipid-Polymer Hybrid Nanoparticles through Controlled Microvortices*. *Nano letters*, 2012. **12**(7): p. 3587-3591.
6. Toth, M.J., T. Kim, and Y. Kim, *Robust Manufacturing of Lipid-Polymer Nanoparticles Through Feedback Control of Parallelized Swirling Microvortices*. *Lab Chip*, 2017. **17**(16): p. 2805-2813.
7. Sei, Y.J., et al., *Detecting the functional complexities between high-density lipoprotein mimetics*. *Biomaterials*, 2018. **170**: p. 58-69.
8. Sei, Y.J., et al., *Detection of frequency-dependent endothelial response to oscillatory shear stress using a microfluidic transcellular monitor*. *Sci Rep*, 2017. **7**(1): p. 10019.

REFERENCES

1. Mozaffarian, D., et al., *Executive summary: heart disease and stroke statistics-2015 update: a report from the american heart association*. Circulation, 2015. **131**(4): p. 434-441.
2. Libby, P., *Inflammation and cardiovascular disease mechanisms*. The American journal of clinical nutrition, 2006. **83**(2).
3. Packard, R.R.S. and P. Libby, *Inflammation in Atherosclerosis: From Vascular Biology to Biomarker Discovery and Risk Prediction*. Clinical Chemistry, 2008. **54**(1): p. 24-38.
4. Wallez, Y. and P. Huber, *Endothelial adherens and tight junctions in vascular homeostasis, inflammation and angiogenesis*. Biochimica et Biophysica Acta (BBA) - Biomembranes, 2008. **1778**(3).
5. Fernandez-Friera, L., et al., *Prevalence, Vascular Distribution, and Multiterritorial Extent of Subclinical Atherosclerosis in a Middle-Aged Cohort: The PESA (Progression of Early Subclinical Atherosclerosis) Study*. Circulation, 2015. **131**(24): p. 2104-13.
6. Nam, D., et al., *Partial carotid ligation is a model of acutely induced disturbed flow, leading to rapid endothelial dysfunction and atherosclerosis*. American Journal of Physiology-Heart and Circulatory Physiology, 2009. **297**(4).
7. Nam, D., et al., *A model of disturbed flow-induced atherosclerosis in mouse carotid artery by partial ligation and a simple method of RNA isolation from carotid endothelium*. J Vis Exp, 2010(40).
8. Son, D., et al., *The atypical mechanosensitive microRNA-712 derived from pre-ribosomal RNA induces endothelial inflammation and atherosclerosis*. Nature Communications, 2013. **4**.
9. Hofmeister, L.H., et al., *Phage-Display-Guided Nanocarrier Targeting to Atheroprone Vasculature*. ACS nano, 2015. **9**(4): p. 4435-4446.
10. Samady, H., et al., *Coronary Artery Wall Shear Stress Is Associated With Progression and Transformation of Atherosclerotic Plaque and Arterial Remodeling in Patients With Coronary Artery Disease*. Circulation, 2011. **124**(7): p. 779-788.

11. Valencia, P.M., et al., *Microfluidic Technologies for Accelerating the Clinical Translation of Nanoparticles*. Nature Nanotechnology, 2012. **7**(10): p. 623-629.
12. Bruckert, E. and D. Rosenbaum, *Lowering LDL-cholesterol through diet: potential role in the statin era*. Current Opinion in Lipidology, 2011. **22**(1): p. 43.
13. Descamps, O.S., et al., *Where does the interplay between cholesterol absorption and synthesis in the context of statin and/or ezetimibe treatment stand today?* Atherosclerosis, 2011. **217**(2): p. 308-321.
14. Weber, C. and H. Noels, *Atherosclerosis: current pathogenesis and therapeutic options*. Atherosclerosis: current pathogenesis and therapeutic options, 2011.
15. Lobatto, M.E., et al., *Perspectives and Opportunities for Nanomedicine in the Management of Atherosclerosis*. Nature Reviews Drug Discovery, 2011. **10**(11): p. 835-852.
16. Khera, A.V., et al., *Cholesterol Efflux Capacity, High-Density Lipoprotein Function, and Atherosclerosis*. The New England Journal of Medicine, 2011. **364**(2): p. 127-135.
17. Kontush, A., S. Chantepie, and M.J. Chapman, *Small, Dense HDL Particles Exert Potent Protection of Atherogenic LDL Against Oxidative Stress*. Arterioscler Thromb Vasc Biol, 2003. **23**(10): p. 1881-8.
18. Walker, K.H., et al., *Cholesterol, Triglycerides, and Associated Lipoproteins*. Cholesterol, Triglycerides, and Associated Lipoproteins, 1990.
19. Kontush, A., et al., *Structure of HDL: particle subclasses and molecular components*. Handb Exp Pharmacol, 2015. **224**: p. 3-51.
20. Rosenson, R.S., et al., *HDL measures, particle heterogeneity, proposed nomenclature, and relation to atherosclerotic cardiovascular events*. Clin Chem, 2011. **57**(3): p. 392-410.
21. Besler, C. and T.F. Lüscher, *Molecular mechanisms of vascular effects of high - density lipoprotein: alterations in cardiovascular disease*. EMBO Molecular Medicine, 2012.

22. Tall, A.R. and L. Yvan-Charvet, *Cholesterol, inflammation and innate immunity*. Cholesterol, inflammation and innate immunity, 2015.
23. von Eckardstein, A. and D. Kardassis, *High Density Lipoproteins*. Handbook of Experimental Pharmacology. 2015: Springer.
24. Wang, M. and M.R. Briggs, *HDL: the metabolism, function, and therapeutic importance*. HDL: the metabolism, function, and therapeutic importance, 2004.
25. Mahmood, S.S., et al., *The Framingham Heart Study and the epidemiology of cardiovascular disease: a historical perspective*. Lancet, 2014. **383**(9921): p. 999-1008.
26. Kannel, W.B., et al., *Risk Factors in Coronary Heart Disease. An Evaluation of Several Serum Lipids as Predictors of Coronary Heart Disease; the Framingham Study*. Ann Intern Med, 1964. **61**: p. 888-99.
27. Tariq, S.M., et al., *HDL hypothesis: where do we stand now?* Curr Atheroscler Rep, 2014. **16**(4): p. 398.
28. Lacko, A.G., N.A. Sabnis, and B. Nagarajan, *HDL As a Drug and Nucleic Acid Delivery Vehicle*. HDL as a drug and nucleic acid delivery vehicle, 2015.
29. Subramanian, C., et al., *Synthetic high-density lipoprotein nanoparticles: A novel therapeutic strategy for adrenocortical carcinomas*. Surgery, 2015.
30. McMahon, K. and C. Thaxton, *High-density lipoproteins for the systemic delivery of short interfering RNA*. Expert Opinion on Drug Delivery, 2013: p. 117.
31. McMahon, K.M., et al., *Biomimetic High Density Lipoprotein Nanoparticles for Nucleic Acid Delivery*. Nano letters, 2011. **11**(3): p. 1208-1214.
32. Barter, P.J., et al., *Antiinflammatory Properties of HDL*. Circulation Research, 2004. **95**(8): p. 764-772.
33. Kratzer, A., H. Giral, and U. Landmesser, *High-Density Lipoproteins As Modulators of Endothelial Cell Functions: Alterations In Patients with Coronary Artery Disease*. Cardiovascular Research, 2014. **103**(3): p. 350-361.

34. Kontush, A., M. Lhomme, and M.J. Chapman, *Unraveling the complexities of the HDL lipidome*. J Lipid Res, 2013. **54**(11): p. 2950-63.
35. Eren, E., N. Yilmaz, and O. Aydin, *Functionally Defective High-Density Lipoprotein and Paraoxonase: A Couple for Endothelial Dysfunction in Atherosclerosis*. Cholesterol, 2013. **2013**: p. 792090.
36. Vandenbroucke, E., et al., *Regulation of endothelial junctional permeability*. Annals of the New York Academy of Sciences, 2008. **1123**: p. 134-145.
37. Shah, A.S., et al., *Proteomic diversity of high density lipoproteins: our emerging understanding of its importance in lipid transport and beyond*. J Lipid Res, 2013. **54**(10): p. 2575-85.
38. Navab, M., G.M. Anantharamaiah, and S.T. Reddy, *Apolipoprotein AI Mimetic Peptides*. Arteriosclerosis, Thrombosis, and Vascular Biology, 2005.
39. Navab, M., et al., *Peptide Mimetics of Apolipoproteins Improve HDL Function*. J Clin Lipidol, 2007. **1**(2): p. 142-7.
40. Kingwell, B.A., et al., *HDL-Targeted Therapies: Progress, Failures and Future*. Nature Reviews Drug Discovery, 2014. **13**(6): p. 445-464.
41. Andrews, J., et al., *Effect of serial infusions of reconstituted high-density lipoprotein (CER-001) on coronary atherosclerosis: rationale and design of the CARAT study*. Cardiovasc Diagn Ther, 2017. **7**(1): p. 45-51.
42. Lincoff, A.M., et al., *Evacetrapib and Cardiovascular Outcomes in High-Risk Vascular Disease*. N Engl J Med, 2017. **376**(20): p. 1933-1942.
43. Rader, D.J. and A. Daugherty, *Translating molecular discoveries into new therapies for atherosclerosis*. Nature, 2008. **451**(7181): p. 904-13.
44. Gu, F., et al., *Precise engineering of targeted nanoparticles by using self-assembled biointegrated block copolymers*. Proceedings of the National Academy of Sciences, 2008.
45. Soppimath, K.S., et al., *Biodegradable polymeric nanoparticles as drug delivery devices*. Journal of Controlled Release, 2001.

46. Torchilin, V.P., *Recent advances with liposomes as pharmaceutical carriers*. Nature Reviews Drug Discovery, 2005. **4**(2): p. 145-160.
47. Kim, B.Y., J.T. Rutka, and W.C. Chan, *Nanomedicine*. The New England journal of medicine, 2010. **363**(25): p. 2434-2443.
48. Cormode, D.P., et al., *Nanocrystal core high-density lipoproteins: a multimodality contrast agent platform*. Nano letters, 2008. **8**(11): p. 3715-3723.
49. Thaxton, C.S., et al., *Templated spherical high density lipoprotein nanoparticles*. J Am Chem Soc, 2009. **131**(4): p. 1384-5.
50. Yang, M., et al., *Efficient Cytosolic Delivery of siRNA Using HDL-Mimicking Nanoparticles*. Small, 2011. **7**(5): p. 568-73.
51. Navab, M., et al., *Oral D-4f Causes Formation of Pre-Beta High-Density Lipoprotein and Improves High-Density Lipoprotein-Mediated Cholesterol Efflux and Reverse Cholesterol Transport from Macrophages in Apolipoprotein E-Null Mice*. Circulation, 2004. **109**(25): p. 3215-20.
52. Zhang, Z., et al., *Biomimetic nanocarrier for direct cytosolic drug delivery*. Angew Chem Int Ed Engl, 2009. **48**(48): p. 9171-5.
53. Huang, M., et al., *GM1-Modified Lipoprotein-like Nanoparticle: Multifunctional Nanoplatform for the Combination Therapy of Alzheimer's Disease*. ACS Nano, 2015. **9**(11): p. 10801-16.
54. Kim, Y., et al., *Single Step Reconstitution of Multifunctional High-Density Lipoprotein-Derived Nanomaterials Using Microfluidics*. ACS nano, 2013. **7**(11): p. 9975-9983.
55. McConathy, W.J., et al., *Evaluation of Synthetic/Reconstituted High-Density Lipoproteins As Delivery Vehicles for Paclitaxel*. Anti-cancer drugs, 2008. **19**(2): p. 183-188.
56. Sanchez-Gaytan, B.L., et al., *HDL-Mimetic PLGA Nanoparticle To Target Atherosclerosis Plaque Macrophages*. Bioconjugate chemistry, 2015.
57. Blanco, E., H. Shen, and M. Ferrari, *Principles of nanoparticle design for overcoming biological barriers to drug delivery*. Nat Biotechnol, 2015. **33**(9): p. 941-51.

58. Ingber, D.E., *Reverse Engineering Human Pathophysiology with Organs-on-Chips*. Cell, 2016. **164**(6): p. 1105-1109.
59. Kim, Y., et al., *Dynamic control of 3D chemical profiles with a single 2D microfluidic platform*. Lab on a chip, 2011. **11**(13): p. 2182-2188.
60. Karnik, R., et al., *Microfluidic Platform for Controlled Synthesis of Polymeric Nanoparticles*. Nano letters, 2008.
61. Capretto, L., et al., *Micromixing Within Microfluidic Devices*. Topics in Current Chemistry, 2011.
62. Ottino, J.M. and S. Wiggins, *Applied physics. Designing optimal micromixers*. Science, 2004. **305**(5683): p. 485-6.
63. Kim, Y., et al., *Mass Production and Size Control of Lipid-Polymer Hybrid Nanoparticles through Controlled Microvortices*. Nano letters, 2012. **12**(7): p. 3587-3591.
64. Toth, M.J., T. Kim, and Y. Kim, *Robust Manufacturing of Lipid-Polymer Nanoparticles Through Feedback Control of Parallelized Swirling Microvortices*. Lab Chip, 2017. **17**(16): p. 2805-2813.
65. Ahn, J., et al., *Tumor Microenvironment on a Chip: The Progress and Future Perspective*. Bioengineering (Basel), 2017. **4**(3).
66. Sei, Y.J., et al., *Detecting the functional complexities between high-density lipoprotein mimetics*. Biomaterials, 2018. **170**: p. 58-69.
67. Huh, D., et al., *Reconstituting organ-level lung functions on a chip*. Science (New York, N.Y.), 2010. **328**(5986): p. 1662-1668.
68. Kim, H.J., et al., *Human gut-on-a-chip inhabited by microbial flora that experiences intestinal peristalsis-like motions and flow*. Lab on a chip, 2012. **12**(12): p. 2165-2174.
69. Booth, R. and H. Kim, *Characterization of a microfluidic in vitro model of the blood-brain barrier (μ BBB)*. Lab on a Chip, 2012. **12**(10): p. 1784-1792.

70. Herland, A., et al., *Distinct Contributions of Astrocytes and Pericytes to Neuroinflammation Identified in a 3D Human Blood-Brain Barrier on a Chip*. PLOS ONE, 2016. **11**(3).
71. Kim, H. and D.E. Ingber, *Gut-on-a-Chip microenvironment induces human intestinal cells to undergo villus differentiation*. Integrative Biology, 2013. **5**(9): p. 1130-1140.
72. Torisawa, Y.-s., et al., *Bone marrow-on-a-chip replicates hematopoietic niche physiology in vitro*. Nature Methods, 2014. **11**(6): p. 663-669.
73. Kim, Y., et al., *Probing nanoparticle translocation across the permeable endothelium in experimental atherosclerosis*. Proceedings of the National Academy of Sciences of the United States of America, 2014. **111**(3): p. 1078-1083.
74. Ferrell, N., et al., *A microfluidic bioreactor with integrated transepithelial electrical resistance (TEER) measurement electrodes for evaluation of renal epithelial cells*. Biotechnology and Bioengineering, 2010. **107**(4): p. 707-716.
75. Odijk, M., et al., *Measuring direct current trans-epithelial electrical resistance in organ-on-a-chip microsystems*. Lab on a Chip, 2014. **15**(3): p. 745-752.
76. Vogel, P.A., S.T. Halpin, and R.S. Martin, *Microfluidic transendothelial electrical resistance measurement device that enables blood flow and postgrowth experiments*. Microfluidic transendothelial electrical resistance measurement device that enables blood flow and postgrowth experiments, 2011.
77. Veniant, M., J.P. Clozel, and W. Fischli, *A comparison of the effects of renin inhibition and angiotensin converting enzyme inhibition upon bradykinin potentiation*. J Hypertens, 1992. **10**(2): p. 155-60.
78. Pampaloni, F., E.G. Reynaud, and E.H. Stelzer, *The third dimension bridges the gap between cell culture and live tissue*. Nature Reviews Molecular Cell Biology, 2007. **8**: p. 839-845.
79. Huh, D., G.A. Hamilton, and D.E. Ingber, *From 3D cell culture to organs-on-chips*. Trends Cell Biol, 2011. **21**(12): p. 745-54.
80. El-Ali, J., P.K. Sorger, and K.F. Jensen, *Cells on chips*. Nature, 2006. **442**(7101): p. 403-411.

81. Moraes, C., et al., *Organs-on-a-chip: a focus on compartmentalized microdevices*. Ann Biomed Eng, 2012. **40**(6): p. 1211-27.
82. Huh, D., et al., *Reconstituting organ-level lung functions on a chip*. Science, 2010. **328**(5986): p. 1662-8.
83. Kim, H.J., et al., *Human gut-on-a-chip inhabited by microbial flora that experiences intestinal peristalsis-like motions and flow*. Lab Chip, 2012. **12**(12): p. 2165-74.
84. Zhou, J. and L.E. Niklason, *Microfluidic artificial "vessels" for dynamic mechanical stimulation of mesenchymal stem cells*. Integr Biol (Camb), 2012. **4**(12): p. 1487-97.
85. Shih, M.C., et al., *A microfluidic device mimicking acinar concentration gradients across the liver acinus*. Biomed Microdevices, 2013.
86. Suwanpayak, N., et al., *Blood cleaner on-chip design for artificial human kidney manipulation*. Int J Nanomedicine, 2011. **6**: p. 957-64.
87. Kuttenger, J., E. Polska, and B.M. Schaefer, *A novel three-dimensional bone chip organ culture*. Clin Oral Investig, 2012.
88. Shein, M., et al., *Engineered neuronal circuits shaped and interfaced with carbon nanotube microelectrode arrays*. Biomed Microdevices, 2009. **11**(2): p. 495-501.
89. Grosberg, A., et al., *Muscle on a chip: in vitro contractility assays for smooth and striated muscle*. Journal of pharmacological and toxicological methods, 2012. **65**(3): p. 126-135.
90. Ghaemmaghami, A.M., et al., *Biomimetic tissues on a chip for drug discovery*. Drug Discov Today, 2012. **17**(3-4): p. 173-81.
91. Liu, D., et al., *Current developments and applications of microfluidic technology toward clinical translation of nanomedicines*. Adv Drug Deliv Rev, 2018. **128**: p. 54-83.
92. Friend, J. and L. Yeo, *Fabrication of microfluidic devices using polydimethylsiloxane*. Biomicrofluidics, 2010. **4**(2).

93. Rohrl, C. and H. Stangl, *HDL Endocytosis and Resecretion*. Biochim Biophys Acta, 2013. **1831**(11): p. 1626-33.
94. Lou, B., et al., *High-Density Lipoprotein as a Potential Carrier for Delivery of a Lipophilic Antitumoral Drug into Hepatoma Cells*. World journal of gastroenterology : WJG, 2005. **11**(7): p. 954-959.
95. Matz, C.E. and A. Jonas, *Micellar Complexes of Human Apolipoprotein A-I with Phosphatidylcholines and Cholesterol Prepared from Cholate-Lipid Dispersions*. J Biol Chem, 1982. **257**(8): p. 4535-40.
96. Shih, A.Y., S.G. Sligar, and K. Schulten, *Maturation of High-Density Lipoproteins*. J R Soc Interface, 2009. **6**(39): p. 863-71.
97. Gu, F., et al., *Structures of Discoidal High Density Lipoproteins: A Combined Computational-Experimental Approach*. J Biol Chem, 2010. **285**(7): p. 4652-65.
98. Thomas, M.J., S. Bhat, and M.G. Sorci-Thomas, *Three-Dimensional Models of HDL ApoA-I: Implications for its Assembly and Function*. J Lipid Res, 2008. **49**(9): p. 1875-83.
99. Marrache, S. and S. Dhar, *Biodegradable Synthetic High-Density Lipoprotein Nanoparticles for Atherosclerosis*. Proceedings of the National Academy of Sciences of the United States of America, 2013. **110**(23): p. 9445-9450.
100. Leman, L.J., B.E. Maryanoff, and M.R. Ghadiri, *Molecules That Mimic Apolipoprotein A-I: Potential Agents for Treating Atherosclerosis*. J Med Chem, 2014. **57**(6): p. 2169-96.
101. Qin, S., et al., *Reverse D4F, an Apolipoprotein-AI Mimetic Peptide, Inhibits Atherosclerosis in Apoe-Null Mice*. Journal of cardiovascular pharmacology and therapeutics, 2012. **17**(3): p. 334-343.
102. Zhang, Z., et al., *HDL-mimicking peptide-lipid nanoparticles with improved tumor targeting*. Small (Weinheim an der Bergstrasse, Germany), 2010. **6**(3): p. 430-437.
103. Cui, L., et al., *A PEGylation-Free Biomimetic Porphyrin Nanoplatform for Personalized Cancer Theranostics*. ACS Nano, 2015. **9**(4): p. 4484-95.
104. Sei, Y., et al., *Engineering Living Systems on Chips: From Cells to Human on Chips*. Microfluidics and Nanofluidics, 2014.

105. Morgan, J.P., et al., *Formation of Microvascular Networks In Vitro*. Nature protocols, 2013. **8**(9): p. 1820-1836.
106. Kim, S., et al., *Engineering of functional, perfusable 3D microvascular networks on a chip*. Lab Chip, 2013. **13**(8): p. 1489-500.
107. Ahn, J., et al., *Probing the effect of bioinspired nanomaterials on angiogenic sprouting using a microengineered vascular system*. IEEE Transactions on Nanotechnology, 2017. **PP**(99): p. 1-1.
108. Besler, C., T.F. Luscher, and U. Landmesser, *Molecular Mechanisms of Vascular Effects of High-Density Lipoprotein: Alterations in Cardiovascular Disease*. EMBO Mol Med, 2012. **4**(4): p. 251-68.
109. Zhang, L., et al., *Optimized Negative-Staining Electron Microscopy for Lipoprotein Studies*. Optimized negative-staining electron microscopy for lipoprotein studies, 2013.
110. Gordon, S.M., et al., *A comparison of the mouse and human lipoproteome: suitability of the mouse model for studies of human lipoproteins*. J Proteome Res, 2015. **14**(6): p. 2686-95.
111. Scarselli, E., et al., *The human scavenger receptor class B type I is a novel candidate receptor for the hepatitis C virus*. EMBO J, 2002. **21**(19): p. 5017-25.
112. Rohrer, L., et al., *High-Density Lipoprotein Transport Through Aortic Endothelial Cells Involves Scavenger Receptor Bi and Atp-Binding Cassette Transporter G1*. Circ Res, 2009. **104**(10): p. 1142-50.
113. Xia, P., et al., *High Density Lipoproteins (HDL) Interrupt the Sphingosine Kinase Signaling Pathway A POSSIBLE MECHANISM FOR PROTECTION AGAINST ATHEROSCLEROSIS BY HDL*. Journal of Biological Chemistry, 1999. **274**(46): p. 33143-33147.
114. Clay, M.A., et al., *Time sequence of the inhibition of endothelial adhesion molecule expression by reconstituted high density lipoproteins*. Atherosclerosis, 2001. **157**(1): p. 23-29.
115. Fotis, L., et al., *Intercellular adhesion molecule (ICAM)-1 and vascular cell adhesion molecule (VCAM)-1 at the early stages of atherosclerosis in a rat model. in vivo*, 2012. **26**(2): p. 243-250.

116. van Haelst, P.L., et al., *Acute Myeloid Leukaemia As a Cause of Acute Ischaemic Heart Disease*. *Neth Heart J*, 2006. **14**(2): p. 62-65.
117. Denard, B., C. Lee, and J. Ye, *Doxorubicin Blocks Proliferation of Cancer Cells through Proteolytic Activation of CREB3L1*. *Elife*, 2012. **1**: p. e00090.
118. Sardao, V.A., et al., *Morphological Alterations Induced by Doxorubicin on H9c2 Myoblasts: Nuclear, Mitochondrial, and Cytoskeletal Targets*. *Cell Biol Toxicol*, 2009. **25**(3): p. 227-43.
119. Nishida, N., et al., *Angiogenesis in Cancer*. *Vasc Health Risk Manag*, 2006. **2**(3): p. 213-9.
120. Oehler, V.G., et al., *The Derivation of Diagnostic Markers of Chronic Myeloid Leukemia Progression from Microarray Data*. *Blood*, 2009. **114**(15): p. 3292-8.
121. Van Der Spoel, D., et al., *Gromacs: Fast, Flexible, and Free*. *J Comput Chem*, 2005. **26**(16): p. 1701-18.
122. Marrink, S.J., et al., *The Martini Force Field: Coarse Grained Model for Biomolecular Simulations*. *J Phys Chem B*, 2007. **111**(27): p. 7812-24.
123. Periole, X., et al., *Combining an Elastic Network With a Coarse-Grained Molecular Force Field: Structure, Dynamics, and Intermolecular Recognition*. *J Chem Theory Comput*, 2009. **5**(9): p. 2531-43.
124. Wassenaar, T.A., et al., *Computational Lipidomics with Insane: A Versatile Tool for Generating Custom Membranes for Molecular Simulations*. *J Chem Theory Comput*, 2015. **11**(5): p. 2144-55.
125. Midtgaard, S.R., et al., *Self-Assembling Peptides Form Nanodiscs that Stabilize Membrane Proteins*. *Soft Matter*, 2014. **10**(5): p. 738-52.
126. Mishra, V.K., et al., *Effect of Leucine to Phenylalanine Substitution on the Nonpolar Face of a Class A Amphipathic Helical Peptide on its Interaction with Lipid: High Resolution Solution Nmr Studies of 4f-Dimyristoylphosphatidylcholine Discoidal Complex*. *J Biol Chem*, 2008. **283**(49): p. 34393-402.
127. Kim, Y., et al., *Three-dimensional chemical profile manipulation using two-dimensional autonomous microfluidic control*. *J Am Chem Soc*, 2010. **132**(4): p. 1339-47.

128. Genovese, D., et al., *Prevention of self-quenching in fluorescent silica nanoparticles by efficient energy transfer*. Angew Chem Int Ed Engl, 2013. **52**(23): p. 5965-8.
129. Mohan, P. and N. Rapoport, *Doxorubicin as a molecular nanotheranostic agent: effect of doxorubicin encapsulation in micelles or nanoemulsions on the ultrasound-mediated intracellular delivery and nuclear trafficking*. Mol Pharm, 2010. **7**(6): p. 1959-73.
130. Snider, C., et al., *MPEX: A Tool for Exploring Membrane Proteins*. Protein Sci, 2009. **18**(12): p. 2624-8.
131. Kim, S., M. Chung, and N.L. Jeon, *Three-dimensional biomimetic model to reconstitute sprouting lymphangiogenesis in vitro*. Biomaterials, 2016. **78**: p. 115-28.
132. Wang, W., et al., *Cationic Polymethacrylate-Modified Liposomes Significantly Enhanced Doxorubicin Delivery and Antitumor Activity*. Sci Rep, 2017. **7**: p. 43036.
133. Ye, W.L., et al., *Cellular uptake and antitumor activity of DOX-hyd-PEG-FA nanoparticles*. PLoS One, 2014. **9**(5): p. e97358.
134. Kuai, R., et al., *High-Density Lipoproteins: Nature's Multifunctional Nanoparticles*. ACS Nano, 2016. **10**(3): p. 3015-41.
135. Hwang, J.Y., et al., *Multimodality imaging in vivo for preclinical assessment of tumor-targeted doxorubicin nanoparticles*. PLoS One, 2012. **7**(4): p. e34463.
136. Sei, Y.J., et al., *Detection of frequency-dependent endothelial response to oscillatory shear stress using a microfluidic transcellular monitor*. Sci Rep, 2017. **7**(1): p. 10019.
137. Libby, P., P.M. Ridker, and A. Maseri, *Inflammation and atherosclerosis*. Circulation, 2002. **105**(9): p. 1135-43.
138. Chappell, D.C., et al., *Oscillatory shear stress stimulates adhesion molecule expression in cultured human endothelium*. Circ Res, 1998. **82**(5): p. 532-9.
139. Johnson, B.D., K.J. Mather, and J.P. Wallace, *Mechanotransduction of shear in the endothelium: Basic studies and clinical implications*. Vascular Medicine, 2011. **16**(5): p. 365-377.

140. Seebach, J., et al., *Endothelial barrier function under laminar fluid shear stress*. Lab Invest, 2000. **80**(12): p. 1819-31.
141. Ku, D.N., et al., *Pulsatile flow and atherosclerosis in the human carotid bifurcation. Positive correlation between plaque location and low oscillating shear stress*. Arteriosclerosis, 1985. **5**(3): p. 293-302.
142. Chatzizisis, Y.S., et al., *Role of endothelial shear stress in the natural history of coronary atherosclerosis and vascular remodeling: molecular, cellular, and vascular behavior*. J Am Coll Cardiol, 2007. **49**(25): p. 2379-93.
143. Cunningham, K.S. and A.I. Gotlieb, *The role of shear stress in the pathogenesis of atherosclerosis*. Lab Invest, 2005. **85**(1): p. 9-23.
144. Hwang, J., et al., *Oscillatory shear stress stimulates endothelial production of O₂-from p47phox-dependent NAD(P)H oxidases, leading to monocyte adhesion*. J Biol Chem, 2003. **278**(47): p. 47291-8.
145. Ni, C.W., et al., *Development of immortalized mouse aortic endothelial cell lines*. Vasc Cell, 2014. **6**(1): p. 7.
146. Getz, G.S. and C.A. Reardon, *Animal models of atherosclerosis*. Arterioscler Thromb Vasc Biol, 2012. **32**(5): p. 1104-15.
147. Chiu, J.-J. and S. Chien, *Effects of Disturbed Flow on Vascular Endothelium: Pathophysiological Basis and Clinical Perspectives*. Physiological Reviews, 2011. **91**(1): p. 327-387.
148. Sorescu, G.P., et al., *Bone morphogenic protein 4 produced in endothelial cells by oscillatory shear stress stimulates an inflammatory response*. J Biol Chem, 2003. **278**(33): p. 31128-35.
149. Velasco, V., et al., *An orbital shear platform for real-time, in vitro endothelium characterization*. Biotechnol Bioeng, 2016. **113**(6): p. 1336-44.
150. Young, E.W. and C.A. Simmons, *Macro- and microscale fluid flow systems for endothelial cell biology*. Lab Chip, 2010. **10**(2): p. 143-60.
151. VanderLaan, P.A., C.A. Reardon, and G.S. Getz, *Site specificity of atherosclerosis: site-selective responses to atherosclerotic modulators*. Arterioscler Thromb Vasc Biol, 2004. **24**(1): p. 12-22.

152. Himburg, H.A., S.E. Dowd, and M.H. Friedman, *Frequency-dependent response of the vascular endothelium to pulsatile shear stress*. Am J Physiol Heart Circ Physiol, 2007. **293**(1): p. H645-53.
153. Feaver, R.E., B.D. Gelfand, and B.R. Blackman, *Human haemodynamic frequency harmonics regulate the inflammatory phenotype of vascular endothelial cells*. Nat Commun, 2013. **4**: p. 1525.
154. Bhatia, S.N. and D.E. Ingber, *Microfluidic organs-on-chips*. Nature Biotechnology, 2014. **32**(8): p. 760-772.
155. Hosoya, T., et al., *Differential responses of the Nrf2-Keap1 system to laminar and oscillatory shear stresses in endothelial cells*. J Biol Chem, 2005. **280**(29): p. 27244-50.
156. Ji, J.Y., H.Y. Jing, and S.L. Diamond, *Hemodynamic regulation of inflammation at the endothelial-neutrophil interface*. Annals of Biomedical Engineering, 2008. **36**(4): p. 586-595.
157. Jouven, X., et al., *Heart-rate profile during exercise as a predictor of sudden death*. New England Journal of Medicine, 2005. **352**(19): p. 1951-1958.
158. Fox, K., et al., *Resting heart rate in cardiovascular disease*. J Am Coll Cardiol, 2007. **50**(9): p. 823-30.
159. Chung, B., et al., *Nanomedicines for Endothelial Disorders*. Nano Today, 2015. **10**(6): p. 759-776.
160. Hengzi, W., et al., *Optimizing layout of obstacles for enhanced mixing in microchannels*. Smart Materials and Structures, 2002. **11**(5): p. 662-667.
161. Park, B.Y., R. Zaouk, and M.J. Madou, *Fabrication of Microelectrodes Using the Lift-Off Technique*, in *Microfluidic Techniques: Reviews and Protocols*, S.D. Minteer, Editor. 2006, Humana Press: Totowa, NJ. p. 23-26.
162. Aran, K., et al., *Irreversible, direct bonding of nanoporous polymer membranes to PDMS or glass microdevices*. Lab Chip, 2010. **10**(5): p. 548-52.
163. Shinwari, M.W., et al., *Microfabricated reference electrodes and their biosensing applications*. Sensors (Basel), 2010. **10**(3): p. 1679-715.

164. Vickers, K.C., et al., *Micrnas Are Transported in Plasma and Delivered to Recipient Cells by High-Density Lipoproteins*. *Nature cell biology*, 2011. **13**(4): p. 423-433.
165. Chen, B., et al., *Apolipoprotein AI Tertiary Structures Determine Stability and Phospholipid-Binding Activity of Discoidal High-Density Lipoprotein Particles of Different Sizes*. *Protein Sci*, 2009. **18**(5): p. 921-35.
166. Frank, P.G. and Y.L. Marcel, *Apolipoprotein A-I: Structure-Function Relationships*. *J Lipid Res*, 2000. **41**(6): p. 853-72.
167. Fung, K.Y., et al., *SR-BI Mediated Transcytosis of HDL in Brain Microvascular Endothelial Cells Is Independent of Caveolin, Clathrin, and PDZK1*. *Front Physiol*, 2017. **8**: p. 841.
168. Pagler, T.A., et al., *SR-BI-Mediated High Density Lipoprotein (HDL) Endocytosis Leads to HDL Resecretion Facilitating Cholesterol Efflux*. *J Biol Chem*, 2006. **281**(16): p. 11193-204.
169. Nieland, T.J., et al., *Identification of the molecular target of small molecule inhibitors of HDL receptor SR-BI activity*. *Biochemistry*, 2008. **47**(1): p. 460-72.
170. Nieland, T.J., et al., *Cross-inhibition of SR-BI- and ABCA1-mediated cholesterol transport by the small molecules BLT-4 and glyburide*. *J Lipid Res*, 2004. **45**(7): p. 1256-65.
171. Bertrand, N., et al., *Mechanistic understanding of in vivo protein corona formation on polymeric nanoparticles and impact on pharmacokinetics*. *Nat Commun*, 2017. **8**(1): p. 777.
172. Kuai, R., et al., *Designer vaccine nanodiscs for personalized cancer immunotherapy*. *Nat Mater*, 2017. **16**(4): p. 489-496.